Organic Phosphonate Coatings on $LiNi_{0.5}Mn_{0.3}Co_{0.2}O_2$ High Voltage Lithium Ion Battery Cathodes

By

Wansoo Chang

A dissertation submitted in partial fulfillment of

the requirements for the degree of

Doctor of Philosophy

(Chemistry)

at the

UNIVERSITY OF WISCONSIN-MADISON

2017

Date of final oral examination: 12/16/2016

The dissertation is approved by the following members of the Final Oral Committee:

Mahesh K. Mahanthappa, Associate Professor
Robert J. Hamers, Professor, Chemistry
Mark D. Ediger, Professor, Chemistry
Song Jin, Professor, Chemistry
Ive Hermans, Associate Professor, Chemistry

ABSTRACT

Rechargeable lithium–ion batteries (LIBs) have attained widespread use in small consumer electronic devices, as a consequence of their high energy densities that originate from the small atomic mass and the low standard reduction potential of metallic lithium. However, their modest storage capacities and limited deliverable power restrict their high power applications in long-range electric vehicles and large scale batteries for electrical energy storage and utilization for electrical power grid applications. High voltage $LiNi_xMn_yCo_{1-x-y}O_2$ (NMC) cathode materials offer an attractive route for improving the power deliverable by LIBs, yet NMCs exhibit substantial charge-discharge capacity fade and poor discharge rate performances that currently limit their utilization.

In this thesis, we describe the development and application of various organic phosphonate coatings to high voltage NMC cathode materials in order to improve their electrochemical performance characteristics. First, we developed a thiophene-based coating that may be grafted to NMC cathodes surfaces, which electropolymerizes during LIB charging to generate a thin, electrically conductive organic cathode coating that improves NMC cycling efficiency and fast charge/discharge capacity rate performance. We also studied the impact of electrically insulating, linear alkylphosphonate surface coatings on the electrochemical performances of NMC cathodes. These studies revealed that thicker and more crystalline surface coatings protect the electrolyte from unwanted degradation reactions at the cathode surface, at the cost of impeding Li^+ permeation to NMC surface for cathode intercalation in a manner that severely curtails their discharge rate performance. Finally, we developed a kinetically controlled, template-assisted strategy for generating spatially heterogeneous mixed alkylphosphonate

monolayers on NMC cathode surfaces. By studying the electrochemical behaviors of variously coated NMCs, we determined that surface Ni-rich surface domains are the primary species that cause electrolyte decomposition, while the Mn -and Co- surface domains exhibit the lowest kinetic barrier to Li-ion intercalation during LIB discharging. Thus, this study thus provides new molecular-level insights for developing new coatings that enhnace the performance characteristics of high voltage NMC cathode materials.

PREFACE

Chapter 1 in this thesis presents an overview of ongoing research into lithium ion battery materials and current strategies for coating high–voltage cathode surfaces in order to improve their long-term cycling performance. Chapter 2 concerns the synthesis of an electropolymerizable alkylphosphonate surface ligand that is grafted to the surface of high voltage nickel-manganese-cobalt oxide (NMC) cathodes, and the electrochemical behaviors of these coated cathodes are characterized under typical lithium ion battery charge-discharge cycling conditions. Dr. Tae Woo Kim in the Department of Chemistry at the University of Wisconsin-Madison obtained scanning electron microscopy images and energy dispersive X-ray spectroscopy analyses for this research project. Chapter 3 details our investigations of the ideal characteristics of electrically insulating alkylphosphonate surface coatings for high voltage NMC cathodes. Laura E. Slaymaker and Professor Robert. J. Hamers in the Department of Chemistry at the University of Wisconsin-Madison performed diffuse reflectance infrared spectroscopy as part of this research. Chapter 4 describes our understanding of the role of transition metals on the $LiNi_{0.5}Mn_{0.3}Co_{0.2}O_2$ cathode surfaces using spatially–controlled mixed alkylphosphonate monolayer coatings generated by a kinetically controlled, template-assisted coating strategy. David H. K. Jackson and Professor Thomas F. Kuech in the Department of Chemical & Biological Engineering at the University of Wisconsin-Madison participated in helpful and insightful discussions. Chapters 2, 3, and 4 are currently being prepared for submission to peer-reviewed journals for publication.

ACKNOWLEDGMENTS

I cannot express enough gratitude for the many collaborators, mentors, friends, and family who supported and helped me along the way. Without them, I would have not been able to stand where I am standing now.

First, I want to thank my advisor Professor Mahesh Mahanthappa, who was the primary reason I decided to come to University of Wisconsin-Madison to pursue my Ph.D. When I stepped into his office in the summer of 2011, I was moved by Mahesh's insight and passion for science and immediately realized that I made the right choice to come to Madison. I have never regretted my decision. He was a great mentor and because of his excellent guidance, I was able to make it here. I regret that I do not know enough English to thank Mahesh enough. 교수님 밑에 있을 수 있어 정말 행운이었습니다. 정말 진심으로 감사드립니다.

Also, I want to thank all Mahanthappa group members. Especially, I thank Dominic Perroni and Frank Speetjens for being good friends and great counselors. I will never forget Dominic's numerous ramen challenges and Frank's "second question." I thank Dr. James Jennings for being a great friend and for always being willing to help me and teach me both science and English. I thank Adam Schmitt for being a good friend and for sharing his knowledge of polymer. I thank Grayson Jackson for his friendship and for sharing many useful thoughts in electrochemical analysis and sharing news from Minnesota. I thank Carlos Baez for giving such a positive energy to me. I thank Dr. Sung A Kim for her friendship and listening to all of my complaints in Korean. I thank Ryan Weber and Greg Sorenson. Although Ryan and

Greg's time in the group overlapped with mine only briefly, their impact on the group and me was profound.

I thank all Dow project collaboration members: Shuyu Fang, David Jackson, Laura Slaymaker, Shenzhen Xu, Dr. Laskar Masihhur, Dr. Juan Tuberquia, Dr. Mark Dreibelbis, Professor Robert Hamers, Professor Thomas Kuech and Professor Dane Morgan. It was a collaborative, informative team. I feel proud that I was a member of this collaboration team and that I was able to produce quality research with them.

I thank Professor Hyuk Yu for being my academic grandfather. He was the one who made me come to Wisconsin to pursue a Ph.D in chemistry. When I struggled to decide which graduate program to join, he called me to come to Madison. He was always helpful, thoughtful, and smart. His "two simple questions" will never be forgotten.

Also I thank my family for their love and support. They always encourage me and teach me to be a person who I am. Without them, it would not have been possible to make it to Madison. I would like to say this to my father "I am honored that I was able to follow your path".

I thank my wife Ara. She has been my best friend ever since I entered undergraduate school. She was always there and she always supported me and loved me. We were apart for a quite a long time as I decided to study abroad, but she waited for me and supported me from the opposite side of earth. I feel very lucky to have her as my wife and I look forward to continuing our journey together.

Finally, I would like to thank the committee members, Professors Robert J. Hamers, Mark D. Ediger, Song Jin, and Ive Hermans. I greatly appreciate their feedback and guidance.

FINANCIAL SUPPORT

We gratefully acknowledge The Dow Chemical Company for principal financial support for the work described in this thesis. This research made extensive use of University of Wisconsin–Madison Soft Matter Laboratory and Materials Science Center core characterization facilities, which are supported by NSF through the University of Wisconsin Materials Research Science and Engineering Center (DMR-1121288). Portions of this research also made use of the UW-Madison Department of Chemistry core instrumentation facilities supported by Paul J. and Margaret M. Bender, as well as the National Science Foundation (CHE-9629688, CHE-0342998, CHE-9974839, CHE-1048642, CHE-9208463), and the National Institute of Health (1-S10-RR08389-01).

TABLE OF CONTENTS

LIST OF FIGURES

LIST OF SCHEMES

LIST OF TABLES

CHAPTER 1

AN OVERVIEW OF LITHIUM ION BATTERY AND CATHODE SURFACE MODIFICATION TECHNIQUES

1.1 Lithium Ion Battery (LIB)

A battery is a device that converts chemical energy into electrical energy through a redox reaction. The lithium ion battery (LIB) is one of the most ubiquitous rechargeable (secondary) batteries, operating according to the "rocking-chair" principle where lithium ions move between cathode and anode upon charging and discharging.[1] LIB has high energy density compared to other batteries owing to lithium metals special properties (e.g. small mass and low standard reduction potential).[2] Due to its high energy density, LIB has become one of the most popular power sources for portable electronics such as smartphones, laptop computers and digital cameras. LIB is also broadening its field in areas that require high power and energy such as electric vehicles, hybrid electric vehicles, plug-in hybrid vehicles and large-scale grid energy storage.

LIB's rechargeability arises from the reversible intercalation and de-intercalation of lithium ions from/into the cathode and the anode upon charging and discharging. During the discharging of a LIB, electrons move from the anode to the cathode through an external circuit while lithium ions de-intercalate from the anode and migrate through an electrolyte to intercalate into the cathode structure (Figure 1.1).[1] When charging a LIB, electrons move through the external circuit from cathode to anode, which is accompanied by the migration of lithium ions from cathode to anode through the electrolyte.

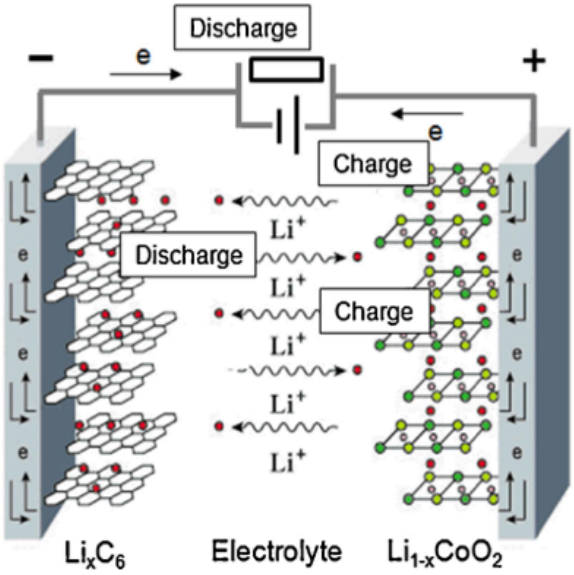

Figure 1.1 Schematic showing lithium ion battery operating mechanism. Lithium ions reversibly intercalate/de–intercalate to electrodes upon charging and discharging. During LIB operation, lithium ions traverse through an electrolyte with the concurrent shuttling of electrons through an external circuit. Figure adopted from Reference 1.

LIBs are typically composed of electrodes (cathode and anode in composite mixture) and an electrolyte with a Li salt (Figure 1.2), the details of which will be discussed in the following sections.

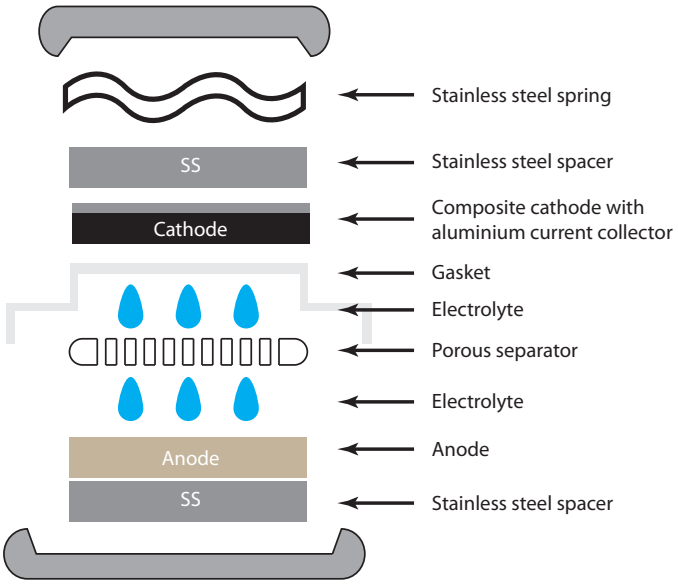

Figure 1.2 Components of a lithium ion battery in coin cell geometry. The cell components and geometry may depend on the type of the LIB.

1.2 Components of LIB

1.2.1 Anode

Currently, three classes of materials are mainly used as the anode in the LIB: Lithium metal, a carbon-based material, and inorganic materials.[3-4] Lithium metal has an extremely high specific capacity (3,860 mAh/g), low standard reduction potential (-3.04 V vs SHE) and low density (0.534 g/cm^3), which makes the lithium metal an ideal candidate for the anode in a LIB.[2, 5] However, lithium metal has two main disadvantages that restrict utilization in actual LIB: 1) *Safety*. During multiple cycles of charge and discharge, lithium can plate at the surface of the lithium metal anode. This plating leads to generation of lithium dendrites that can grow from the anode to the cathode to short circuit the LIB.[5-6] Short-circuiting generates a large amount of heat, which can induce ignition of an organic electrolyte. 2) *Low Coulombic efficiency during*

repeated cycles of the LIB. Unlike other anode materials, lithium metal is deposited and stripped during LIB cycling. Therefore whole lithium metal electrode suffers from the huge volume change[5, 7-8] This huge volume change induces breakdown of the surface layer (known as the solid electrolyte interphase, SEI), which is formed by a reduction of the electrolyte during discharging of the LIB. Formation of the SEI at the anode surface is a inevitable process, which happens within the first two cycles of charging and discharging. However, when the SEI breaks down and is detached from the lithium metal anode surface, newly exposed lithium metal surface leads to generation of additional SEI upon LIB cycling. As lithium ions are consumed during the SEI formation, formation of additional SEI lowers the capacity of the LIB and results in a low coulomb efficiency (80-90% for carbonate based electrolytes and 90-95% for ether based electrolytes).

Carbon-based materials are one of the most widely accepted anode materials for current rechargeable LIBs due to low cost, high Li diffusivity, high electrical conductivity, and relatively low volume change during LIB cycling.[4, 9] Carbon-based anodes such as graphite already have comparable standard reduction potential as the lithium metal itself, therefore when carbon based materials are used, the voltage of a LIB can be retained close to the LIB utilizing lithium metal as the anode. Lithium ions can intercalate and de-intercalate between the graphite layers during charging and discharging of the LIB (Figure 1.3). However, even at the maximum lithium loading, graphite anode has a low theoretical specific capacity (372 mAh/g).

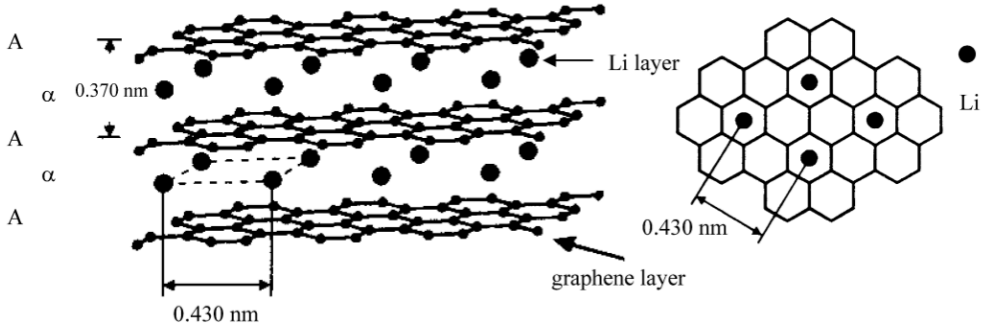

$$6C + xLi^+ + xe^- \underset{\text{discharge}}{\overset{\text{charge}}{\rightleftharpoons}} Li_xC_6,$$

Figure 1.3 Schematic representation for a graphite anode. Lithium ions intercalate and de-intercalate between graphite layers upon charging and discharging. Figure adopted from Reference 4.

In order to increase the total capacity of the LIB, inorganic materials such as Sn, Si, and Ge have been extensively studied as the anode for LIB (Figure 1.4).[3, 10-11] These materials form alloys with lithium and therefore can be utilized as the anode in LIB. Among them silicon has attracted particular attention, as it has the higher theoretical specific capacity (4200 mAh/g) than the lithium metal itself. However, these inorganic anodes experience huge volume changes during battery cycling (as high as 400 %). This huge volume change induces breakdown of the anode (Figure 1.5),[11] loss of contact between anode material and conductive medium as well as the current collector during LIB cycling, and breakdown of the surface SEI layer, which limits their application.

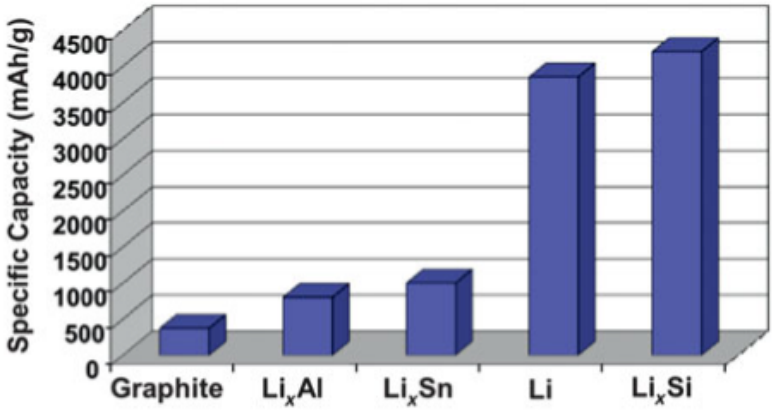

Figure 1.4 Plot showing specific discharge capacity of various anode materials. Silicon-based anodes are particularly attractive due to their high specific capacity. Figure adopted from Reference 3.

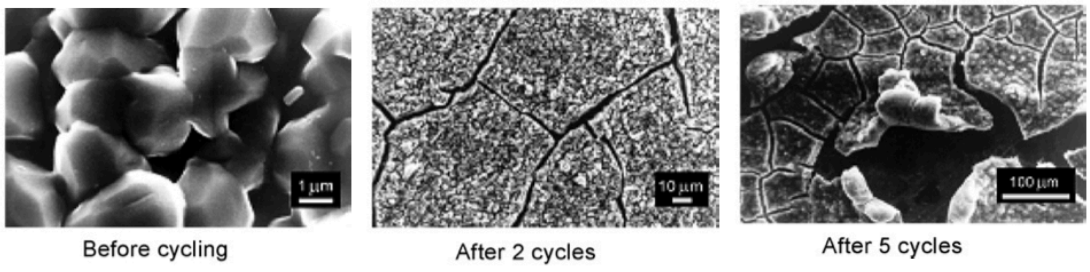

Figure 1.5 SEM images showing Sn-based anode upon LIB cycling. The huge volume change of an inorganic anode leads to the breakdown of the anode. Figure adopted from Reference 11.

1.2.2 Electrolyte

Currently, two classes of electrolytes are mainly used in LIB: Organic liquid electrolyte and organic polymer electrolyte.[12-14] The electrolyte within a LIB should have high ionic conductivity and should be electrochemically stable within the battery operation potential

window (Figure 1.6). If an electrolyte is not electrochemically stable within the battery operation potential window, the electrolyte will oxidatively or reductively degraded during LIB cycling to generate SEI on the electrode surface.

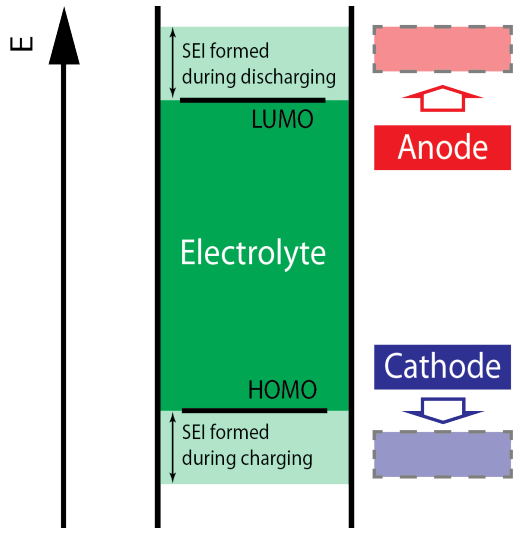

Figure 1.6 Schematic depicting relative energies of the anode and cathode versus the LUMO-HOMO window of the electrolyte. When the energies of the anode and cathode become higher and lower than the LUMO and the HOMO of the electrolyte upon battery cycling, electrolyte will degrade at the electrode surface to generate SEI.

Organic liquid electrolytes are the most widely used electrolytes in LIBs due to their wide operation voltage. Most commonly used organic liquid electrolytes for LIB are blends of two or more carbonates with $LiPF_6$ salt. Ethylene carbonate (EC) is typically mixed with one or more of the following carbonates to depress the melting temperature of the EC (34 to 37 ºC): propylene carbonate, diethyl carbonate, dimethyl carbonate, and ethyl methyl carbonate. EC is an effective electrolyte with high ionic conductivity, high salt dissociation ability, and forms a proper SEI that protects the electrolyte degradation after initial formation of the SEI on the carbon-based

anode surface during LIB cycling.[13, 15-17] Unfortunately, safety is the largest concern when utilizing organic liquid electrolytes in LIBs: carbonate electrolytes are highly flammable (flash point below 30 C°),[13, 18] and $LiPF_6$ salt can undergo autocatalytic decomposition into LiF and PF_5 where PF_5 reacts with any water present inside the battery to generate HF (Figure 1.7),[15, 19] which can potentially degrade electrodes during LIB cycling.

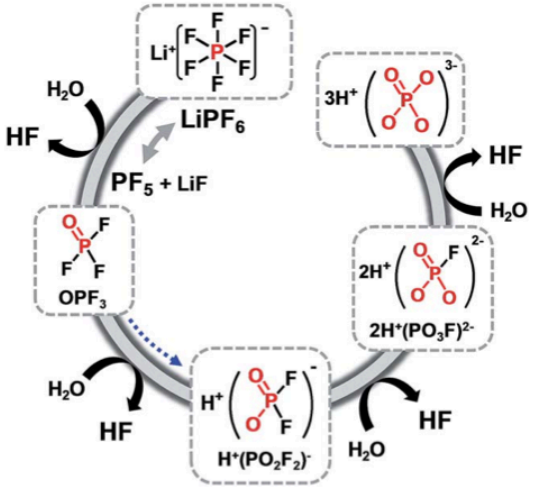

Figure 1.7 Hydrolysis of $LiPF_6$ salt to generate HF during LIB cycling. Figure adopted from Reference 15.

Polymeric materials capable of conducting lithium ions can also be used as electrolytes in LIBs. They can act as the separator and electrolyte simultaneously, as polymer electrolytes typically take the form of solids or viscous gels, which can physically separate cathode and anode while transferring lithium ions. Compared to liquid organic electrolyte, organic polymer electrolytes have benefits in safety.[20-23] Polymer electrolytes with high modulus have been reported to inhibit short-circuiting of LIBs by preventing lithium dendrite growth from the anode to the cathode during LIB cycling. Additionally, they are stable (non-volatile and less

flammable) at elevated temperature, which enables LIBs with polymer electrolyte to operate in high temperature applications.

Typically, block copolymer electrolytes such as PS-b-PEO are composed of a domain that enables transfer of lithium ions (polyethylene oxide) and a domain that endows mechanical integrity (polystyrene) to the polymer electrolyte. Recently, single ion conducting polymer gained much attention. Single ion conducting polymer for LIB is the polymer, in which balancing anions are covalently tethered to the polymer chain, making lithium ions the only movable ions in the electrolyte.[24-26] As charge-compensating anions are fixed, LIB utilizing single ion conducting polymer can maximize the LIB performance. However, most polymer electrolytes have two to three orders of magnitude lower lithium ion conductivity (σ_{Li+}) at room temperature ($\sigma_{Li+} < 10^{-5}$ S/cm) than liquid organic electrolyte that restricts their application.

1.2.3 Cathode

Currently, two types of materials are mainly used as the cathode in the LIB: Lithium metal oxide with a layered structure and a spinel structure (Figure 1.8).[4, 12, 27-28] Layered cathodes have the general formula $LiMO_2$ (M = Ni, Co etc.), and form a distorted rock-salt (α-$NaFeO_2$-type) crystal structure. In this structure, lithium ions intercalate and de-intercalate between MO_6 layers during LIB cycling. Lithium cobalt oxide ($LiCoO_2$, LCO) is probably the most well known and most widely accepted cathode material in commercialized LIB, due to good cycle life and reliability. During charging and discharging of the LIB, cobalt experiences oxidation and reduction between Co^{3+} and Co^{4+}, which induce lithium ions to intercalate into and de-intercalate from the LCO structure. LCO has a cell voltage at around 4 V vs Li/Li^+ with the theoretical specific capacity of 273 mAh/g, however, the practical specific capacity of LCO is only 140

mAh/g. This is due to the oxygen gas evolution that occurs when more than 50 % of lithium ions de-intercalate from the LCO structure upon charging, which leads to degradation of the LCO.

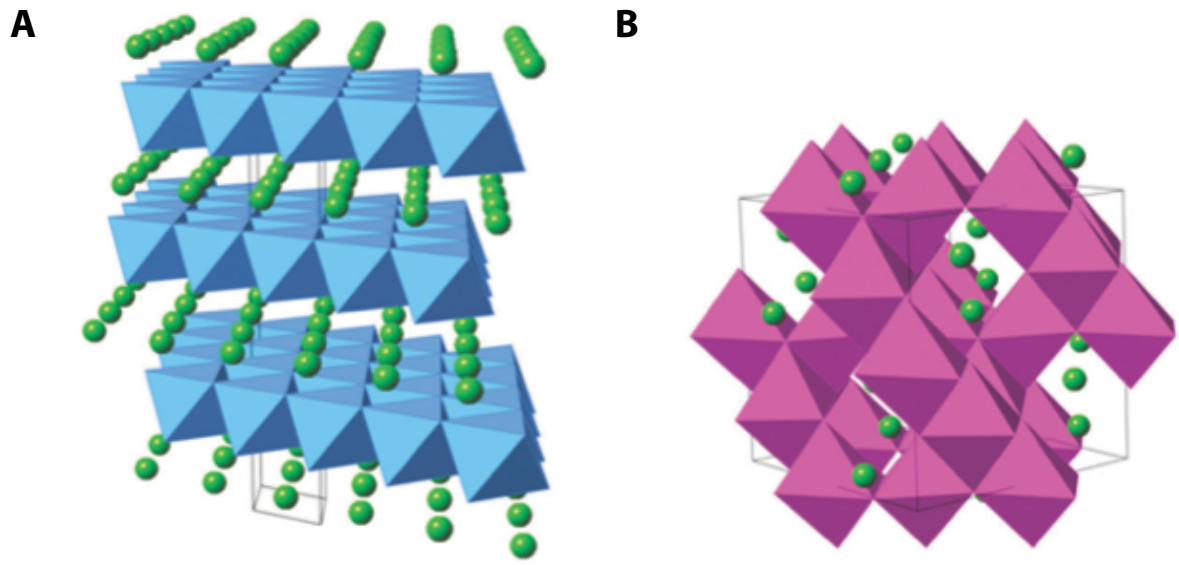

Figure 1.8 (A) Schematic representation of a layered cathode structure. (B) Schematic representation of a spinel cathode structure. Octahedrons represent MO_6 (M = transition metal) and light green spheres represent lithium ions in the cathode structure. The figures were adopted from reference 28.

The spinel cathode for LIB has the general formula LiM_2O_4. In a spinel cathode, lithium ions sit at the tetrahedral sites in the crystal structure and during charging and discharging, lithium ions reversibly move between tetrahedral sites. Among various spinel cathodes, lithium manganese oxide ($LiMn_2O_4$) attracts most attention due to low cost, good thermal stability, good safety and high power capability. However, lithium manganese oxide is a problematic cathode material owing to the occurrence of sudden capacity drops. This sudden capacity drop arises due

to Mn^{3+} ion dissolution and decomposition of an organic electrolyte induced by Mn^{4+} after charging of the LIB.

1.2.4 Composite Electrode

In LIB, active electrode materials must be oxidized or reduced in order to drive intercalation/de-intercalation of lithium ions upon charging and discharging. Cathode for example, transition metals in lithium metal oxide cathode materials must be oxidized or reduced in order to store and release lithium ions during operation of LIB. However, as typical cathode materials are in a powder form, a conductive medium that serves to facilitate electron transfer between the current collector and the active cathode materials must be incorporated into a cathode system. However, conductive medium (carbon-based materials) and cathode materials do not form a stable cathode system, therefore a binder, which glues every component together is needed. These components (lithium metal oxide cathode, conductive medium and binder) comprise the cathode for a LIB and this cathode system is called as the "composite cathode" (Figure 1.9).

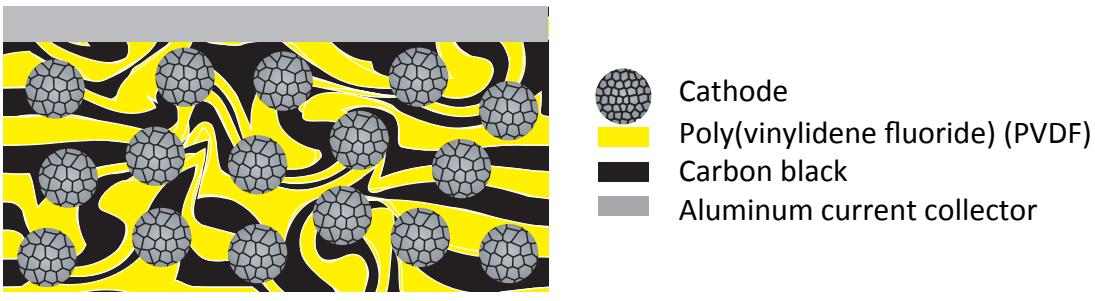

Figure 1.9 Figure illustrating a composite cathode and its components.

To maximize the LIB performance, the composition of each component must be delicately controlled.[29] In LIBs, the capacity is dictated by the total lithium ions that can be stored inside electrodes. Therefore, having more cathode materials in the composite cathode can yield a high capacity LIB. Nevertheless, increasing the amount of cathode materials in the composite cathode is not always ideal, as cathode materials cannot be effectively oxidized and reduced upon charging and discharging, due to the decrease in the amount of conducting medium. On the other hand, having more conductive medium can effectively induce oxidation and reduction of lithium metal oxide cathode materials, but lead to less active cathode materials in the composite mixture, which resulted in a low capacity.

Like a cathode, an anode is also composed of various components to induce oxidation and reduction of the anode materials during discharging and charging of the LIB. Similar to a composite cathode, an anode in LIB is a composite anode composed of a conductive medium, an active anode material and a binder.

1.3 Lithium Ion Battery for High Power Application

Power is the rate of doing work, and defined as the product of the voltage (J/C) and the current (C/s). In an electric vehicle, for example, power is the ability to accelerate a car. As voltage affects the power of LIB, many efforts have been made to increase the voltage of the LIB. The voltage of a LIB is determined by the electrochemical potential difference (standard reduction potential difference) between the cathode and the anode. However, the electrochemical potential of the anode cannot get lower than the lithium metal itself, and carbon based anodes already have similar reduction potential values as the lithium metal, therefore high voltage cathodes have gained great attention in order to increase the voltage of the LIB.

One of the most common and efficient approaches to generate high voltage cathodes is modifying already existing cathode materials. In particular, incorporating different transition metals such as nickel and manganese into LCO has been proven to increase the voltage effectively. By replacing some cobalt in LCO structure with nickel and manganese, $LiNi_xMn_yCo_{1-x-y}O_2$ (NMC) electrode was successfully developed.[3, 12-14, 30-32] NMC cathodes in which Mn and Ni replace some of the Co sites in the $LiCoO_2$, have a much higher capacity value (~250 mAh/g) and higher cell voltage (4.3 V or higher), making LIB more suitable for high power applications. However, such high voltage cathode materials have problems in long term cycling due to various issues, including: transition metal dissolution, oxidation of conductive particles, electrolyte degradation, and surface layer formation that reduces LIB cycling efficiency (Figure 1.10).[1, 14, 31, 33-37]

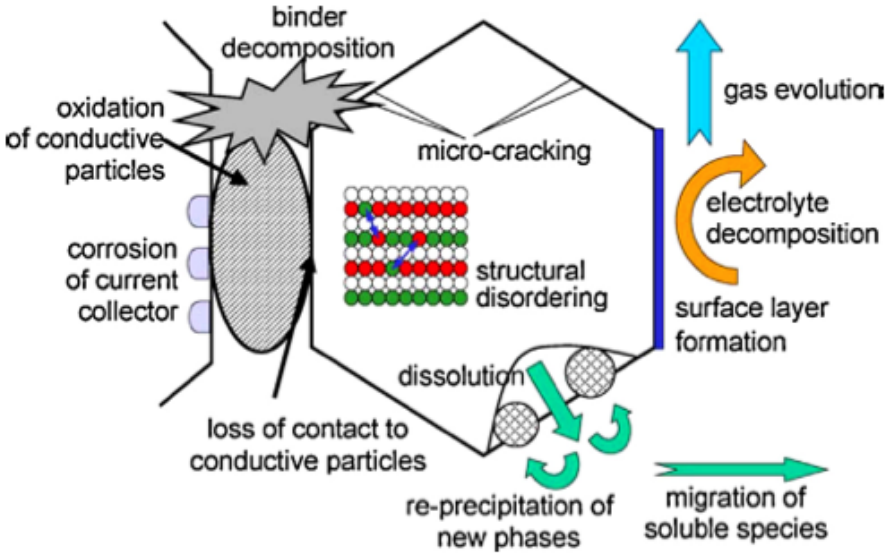

Figure 1.10 Various problems that lowers cycling efficiency of the high voltage cathode. Figure was adopted from Reference 1.

As transition metals in the cathode determine the voltage of the LIB, transition metal dissolution can lead to a voltage drop of the LIB.[11-12, 38-39] Additionally, transition metal dissolution can induce irreversible phase transformations of the cathode crystal structure. As storage of lithium ions in the cathode is affected by the cathode crystal structure, phase transformation can significantly change the cycle efficiency of the LIB.

Oxidation of LIB components is another critical issue in high voltage cathode materials. Carbonate-based organic electrolytes were reported to be stable to oxidation up to 4.3 V vs Li/Li^+.[15, 40-43] However, as the typical operation voltage in high voltage cathodes easily exceeds 4.3 V vs Li/Li^+, and carbonate-based organic electrolytes can oxidize at the cathode surface during charging of the LIB. Upon charging the LIB, electrons move from cathode to anode through an external circuit, which induces the Fermi level of the cathode to drop. When the cathode's Fermi level drops below the HOMO of the electrolyte, the electrolyte oxidizes on the cathode surface to generate the SEI (often referred to as the cathode electrolyte Interphase) (Figure 1.11).[13-14, 33-34] Formation of SEI leads to the long-term performance drop of the LIB. SEI increases the internal resistance of the LIB, as SEI is the breakdown products of electrolyte components. Additionally, it is reported that lithium ions are consumed during SEI formation, hence lowering the total capacity of the LIB.

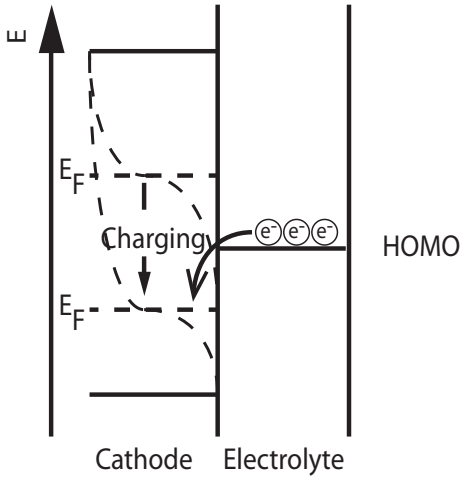

Figure 1.11 Energy diagram showing the drop of the Fermi level of the cathode upon charging the LIB. Upon charging the LIB, Fermi level of the cathode drops below the HOMO of the electrolyte, which can induce the oxidation of the electrolyte.

SEIs are fragile and can easily break and be detached from the cathode surface upon charging and discharging. Unlike inorganic anodes such as Si, high voltage cathode materials do not experience huge volume change upon LIB cycling. However, it has been reported that the high voltage cathode can still experience about 7-10 % of volume change during LIB cycling.[44-47] The size of the LIB cathode is in μm scale whereas a SEI formed via oxidation of the electrolyte has a thickness in the nm scale. Therefore, even with the little volume change of the cathode during LIB cycling, SEI can still fracture and be detached from the cathode surface. When an SEI is detached from the cathode surface, newly exposed cathode surface leads to generation of additional SEI that lowers the cycle efficiency of the battery (Figure 1.12).

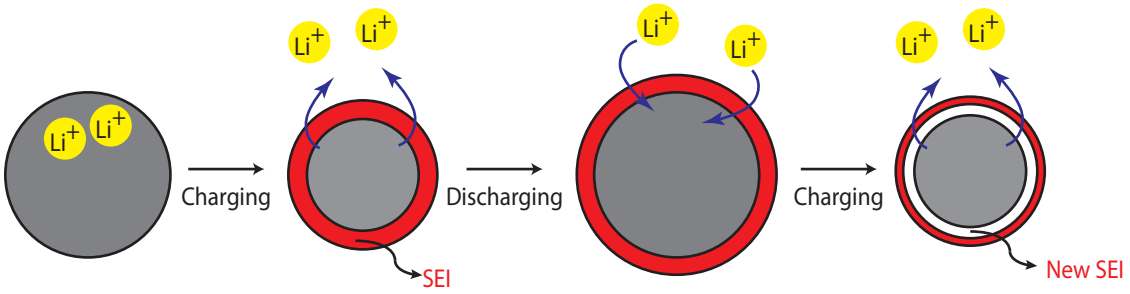

Figure 1.12 Schematic showing the formation of the SEI at the cathode surface during LIB cycling. Gray circle represents the LIB cathode. Upon charging, lithium ions de–intercalte from the cathode leads to decrease in volume and becomes reactive enough to oxidatively degrade the electyrolyte to generate the SEI at the cathode surface. During discharging, lithium ion intercalate to the cathode that leads to increase the volume of the cathode. During charging and discharging, cathode experiences volume change (c.a. 7 – 10%), which is large enough to induce the breakdown of the SEI at the cathode surface. When SEI breaks down and detached off from the cathode surface, newly exposed cathode surface can generate additional SEI upon battery cycling.

1.4 Improving High Voltage Cathode Performance

1.4.1 Coating High Voltage Cathode

Most unwanted side reactions that lower the performance of the high voltage cathode occur at the cathode surface and various materials (inorganic, carbon) have been coated on the high voltage cathode surface using various methods (ALD, Sol-gel, calcination, etc.) to minimize side effects.

1.4.1.1 Inorganic Coating

Various electron–insulating inorganic coatings have been employed to coat the high voltage cathode surface to enhance the LIB performance by reducing side reactions (Figure 1.13).[48-53]

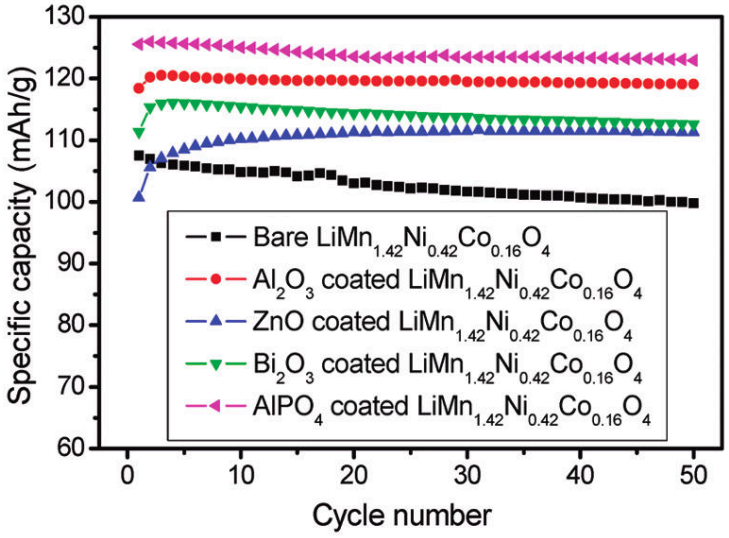

Figure 1.13 The effect of various insulating inorganic coatings on the cycle performance of a LIB cathode. The plot shows that LIB cathodes coated with insulating inorganic coatings retain higher specific discharge capacity values than bare (uncoated) LIB cathode. This clearly demonstrates that insulating inorganic coatings can improve the battery performance. Figure adopted from Reference 30.

As electrolyte degrades at the cathode surface via electrochemical oxidation during charging of the LIB, application of insulating inorganic coatings effectively reduces the oxidation-driven electrolyte degradation during LIB cycling. In addition, these coatings have been demonstrated to prevent transition metal dissolution and to protect the cathode from the HF attack, which can be generated from $LiPF_6$ salt in the presence of a small amount of water inside

the electrolyte. These inorganic insulating materials have been coated on the high voltage cathode surface using techniques by atomic layer deposition (ALD) and sol-gel method (Figure 1.14).

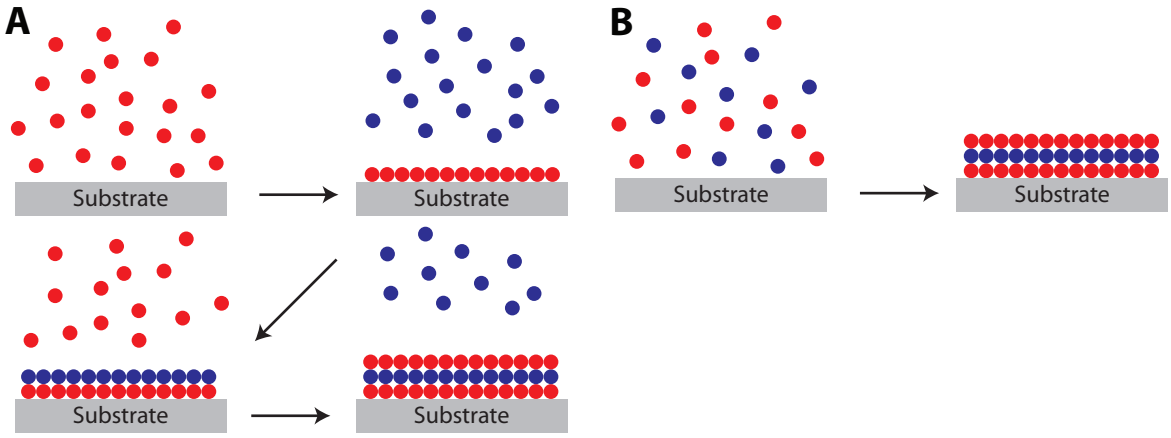

Figure 1.14 Schematic representation of a) ALD and b) Sol-gel method.

ALD is a technique relying on the sequential gas phase reaction to produce thin inorganic film/coating on a substrate. In ALD, at least two types of reactants are used. First, the surface is treated with one reactant until the surface is fully saturated with the reactant. Then, excess reactants are removed before treating with a different reagent. After removal of the excess reactant, the surface reacted with the first reagent is exposed to a different reagent. Then excess reactants are taken out before retreating the surface with the first reactant (Figure 1.14-a). For example, trimethylaluminum and water are two reactants used to generate Al_2O_3 thin coating. ALD has a benefit of controlling the coating thickness on the atomic length scale. However, finding optimal growth conditions (often called self-defining conditions) can be difficult as growth conditions depend on the types of reactants and reaction temperature. Also, ALD is not the most cost efficient methods to generate a coating on a large scale.[54]

Sol-gel method is another technique to generate inorganic coatings on the surface via cross-linking polymerization of inorganic monomers (Figure 1.14-b). The sol-gel method can generate coatings on a large scale, however, as the sol-gel method relies on crosslinking polymerization of inorganic monomers, which lacks in control, it is challenging to control the coating thickness and coating uniformity for coatings thinner than 100 nm.[55]

1.4.1.2 Carbon Coating

Carbon coatings on the cathode surface have shown to enhance the electron conductivity between the current collector and cathode.[56-57] Due to the enhanced electron transfer, LIB uses carbon-coated cathode could be charged or discharged in a faster rate compared to non-carbon coated cathode (Figure 1.15). Additionally, since an electron-conducting medium must be incorporated in the composite LIB cathode, an electron conductive carbon coating on the cathode surface can reduce the amount of the conductive medium incorporated in the composite cathode. This results in an increase of the total capacity of the LIB. Various methods, including: dry mixing,[58] sol-gel,[59] spray pyrolysis,[60] ball milling,[61] co-precipitation,[62] and chemical vapor deposition (CVD)[63] have been developed to coat the cathode surface with conducting carbon materials.

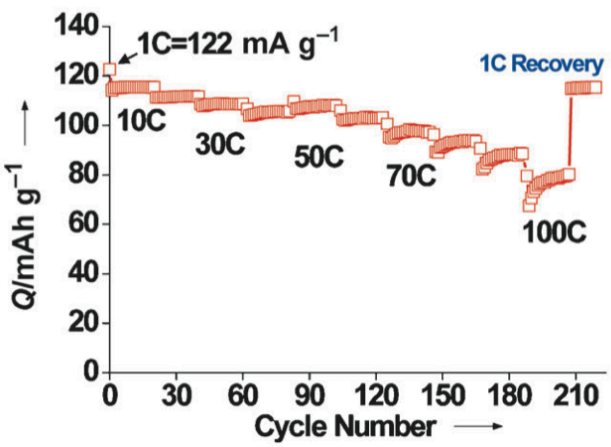

Figure 1.15 Effect of carbon coatings on the LIB cathode. LIB cathodes coated with carbon-based materials show high specific discharge capacity retention at high discharge rates. About 75 % of discharge capacity was retained even at 100 C discharge rate (1 C is the rate to fully charge or discharge the LIB in 1 hour. At 100 C, the LIB is discharged in 36 seconds). Figure adopted from Reference 57.

Although carbon coatings have improved battery performance (especially a rate performance), there are some issues that must be overcome. There are two potential routes to apply carbon coatings on the cathode surface: pre and post coating. Pre coating is a path in which the cathode surface is coated during synthesis of the lithium metal oxide cathode, whereas post coating is a route to generate carbon coating on the cathode surface to an already synthesized cathode.[56] Pre coating has benefits of controlling qualities (e.g. thickness, coverage) of the coating. However, when carbon coating the cathode materials during synthesis of the cathode, carbon coating precursors are likely to burn out as typical lithium transition metal oxide cathodes are synthesized in air or pure oxygen at elevated temperature (> 800 C°). In the case of calcinating in an inert atmosphere, precursors can still thermally decompose to generate strongly

reductive H_2 and CO, which can reduce transition metal in the lithium transition metal cathode. Therefore, the most common approach to coat the cathode with carbon-based materials relies on post coating (mechanical mixing). However, post coating allows limited control over the thickness and uniformity of the coating.[56]

1.4.2 Electrolyte Additive

As stated above, the most common approach to alleviate side reactions occurring at the high voltage cathode surfaces is coating. Different approach to mitigate side effects other than coating is using the organic molecule as electrolyte additives.[64-65] Usually, additives in electrolyte do not exceed more than 5 % by weight or volume. Even a little amount of additives, they have shown to effectively improve LIB performance.

Additives are added to the LIB for various purposes, including: to facilitate formation of SEI, to stabilize an already formed SEI, to enhance thermal stability of the LIB, to protect transition metal from dissolution; to protect the electrode from HF or water, to improve physical properties of the electrolyte (e.g., ionic conductivity, viscosity, electrolyte wettability), overcharge protection, to enhance thermal stability by lowering the flammability of an organic electrolytes, to terminate LIB operation in an abuse condition.

Within the cathode, additives had been mainly exploited for HF scavenging,[66-67] preventing transition metal dissolution,[68-69] formation of a polymeric coating via electropolymerization and overcharge protection.[70-75] For HF scavenging, amine based organic base and carbodiimide compounds have been studied. Transition metal dissolution was prevented by the formation of insoluble products with dissolved metal ions and additive molecules. These insoluble products worked as a protective film to coat the cathode surface to prevent further

dissolution of transition metal ions. Molecules such as thiophene and pyrrole and its derivatives were studied as additives to generate polymeric coatings on cathode surfaces upon charging of the LIB. These molecules are known to electropolymerize in oxidizing condition, therefore when these molecules were used as the additives, these molecules went on electropolymerization at the cathode surface during charging of the LIB to generate polymeric coatings at the cathode surface. These polymeric coatings have shown to mitigate side reactions at the cathode surface. Moreover, these electropolymerized coatings are electron conductive, which aids electron conductivity between the current collector and cathode. Molecules that can oxidize at slightly higher than an end-of-charge potential and reduce back to the neutral state within the LIB cycling condition were used as overcharge protecting additives. When a cathode experiences overcharging, various side reactions such as oxygen evolution and oxidation driven electrolyte degradation can occur. Therefore, depending on the voltage window of the LIB, various molecules have been exploited as additives to protect the cathode from overcharging.

However, as most additives were studied to improve one specific property of the LIB, additives may cause negative impacts on other properties.[76] For example, additive that enhances cathode performance could be negative to the anode performance. Moreover, studies on additives rely on the trial and error type approach, finding appropriate general guideline for additives is inefficient. As shown in Figure 1.16, LIB performance can vary depending on the amount of additive in the electrolyte, which implies that any possible compositions must all be tested in order to ensure the performance of the additives. In addition, additive molecules may behave differently depending on the electrolyte composition.

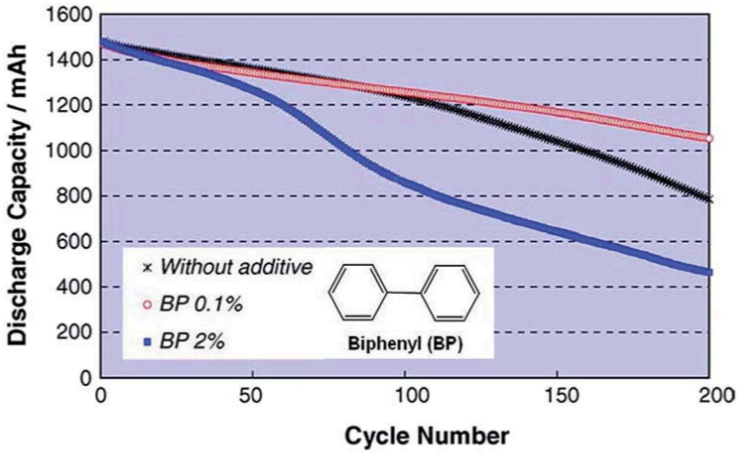

Figure 1.16 Effect of a biphenyl (BP) additive on LIB cycling performance. The biphenyl additive formed an artificial SEI on LCO cathode surface (68 Å thick layer for 0.1 % BP and 217 Å thick layer for 2 % BP), which resulted in an improved cycle performance. This result implies that amount of electrolyte additive must be delicately controlled in order to improve the LIB performances. Figure adopted from Reference 15.

1.5 Organic Coating

As discussed above, there are several methods to improve performances of the high voltage cathode. However, each method has clear advantages and disadvantages. Inorganic coating produced by ALD improved LIB performance. But it is not a suitable method to produce coating in large scale. For sol-gel, it was hard to control the uniformity and the thickness of the coating. Carbon coating enhanced rate performance, yet, it is also hard to control the coating thickness or the uniformity. Unlike these non-organic coating techniques, electrolyte additives have improved LIB performance in many different aspects. However, as additives were mostly

studied for one purpose, additive to enhance one component in LIB can negatively affect other LIB components. Additionally, as there is no guideline for additives, most studies on additives rely on the trial and error type approach that is inefficient and time consuming.

Unlike these approaches, incorporating organic molecules to introduce desired functionalities for specific purposes can open up new possibilities. For example, it is possible to generate electron conducting coating and electron insulating coating starting from the same starting material. Additionally, as organic coating can be done in the solution state (e.g. spray coating, roll to roll coating, spin coating, etc.) it can be cost efficient to generate a uniform coating in large scale.

1.5.1 Self-Assembled Monolayer (SAM) Coating

Organic molecules bearing acid functionalities such as phosphonic acid ($-PO_3H_2$) and carboxylic acid (-COOH) are known to spontaneously react with the hydroxyl group (-OH) at the metal oxide surface to generate a self-assembled monolayer (SAM) (Figure 1.17).[77-83] In particular, phosphonic acid (PA) is known to form a mechanically robust phosphonate bond, which is known to be stable towards hydrolysis. PA is also known to preferentially form phosphonate monolayer rather than multilayers. Moreover, any multilayers formed during grafting of PAs can easily be removed by washing the multilayers. As lithium metal oxides are widely used as the cathode for LIB, organic molecules having PA groups can be potentially used to generate organic coatings on the cathode surface by forming phosphonate SAMs.

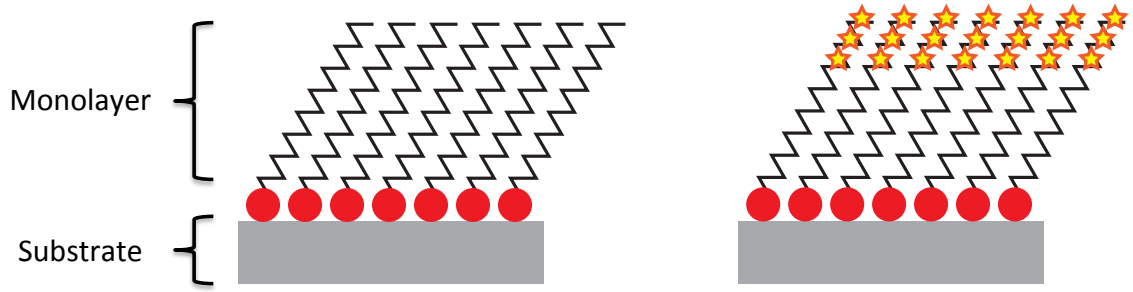

Figure 1.17 Schematic representation of a SAM on a metal oxide substrate. Red circles refer to the acid functionality in the organic molecule, and yellow stars represent the various functionalities that can be incorporated into the molecular structure.

1.5.2 Synthesis of Phosphonic Acid

There are few synthetic routes available to incorporate phosphonic acid into organic molecules. Among them, Michaelis-Arbuzov reaction (Scheme 1.1) between an alkyl phosphite and an alkyl halide, followed by deprotection of the phosphonate (Scheme 1.2) is a well-known and the most widely adopted synthetic method to introduce PA functionality into a molecular structure.[84] Triethylphosphite and alkyl bromide are the most widely utilized alkyl phosphite and alkyl halides adopted for Arbuzov reaction. In Arbuzov reaction using triethylphosphite and alkyl bromide, key step to increase the yield of the synthesis is venting the reaction vessel to remove ethylbromide during reaction. Ethylbromide formed during the Arbuzov reaction as a byproduct and it is also another halide source, which can react with alkylphosphite to produce ethyl diethylphosphonate that lowers synthetic yield (Scheme 1.3). Since boiling point of ethyl bromide is around 38 ˚C, venting the reaction vessel drives the forward reaction based on the Le Chatelier's principle.

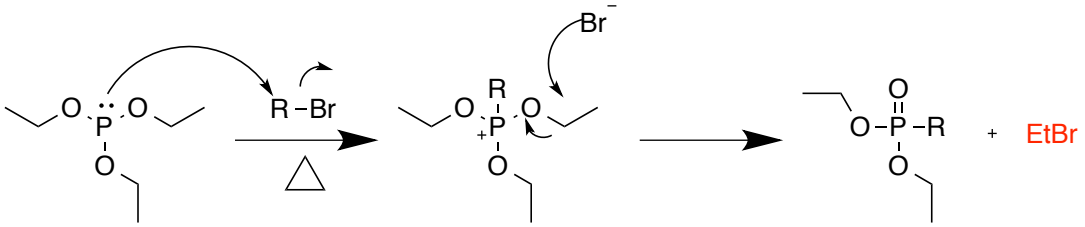

Scheme 1.1 Reaction mechanism of the Michaelis-Arbuzov reaction using triethylphosphite and an alkyl bromide. During Arbuzov reaction, ethyl bromide is generated as the reaction byproduct.

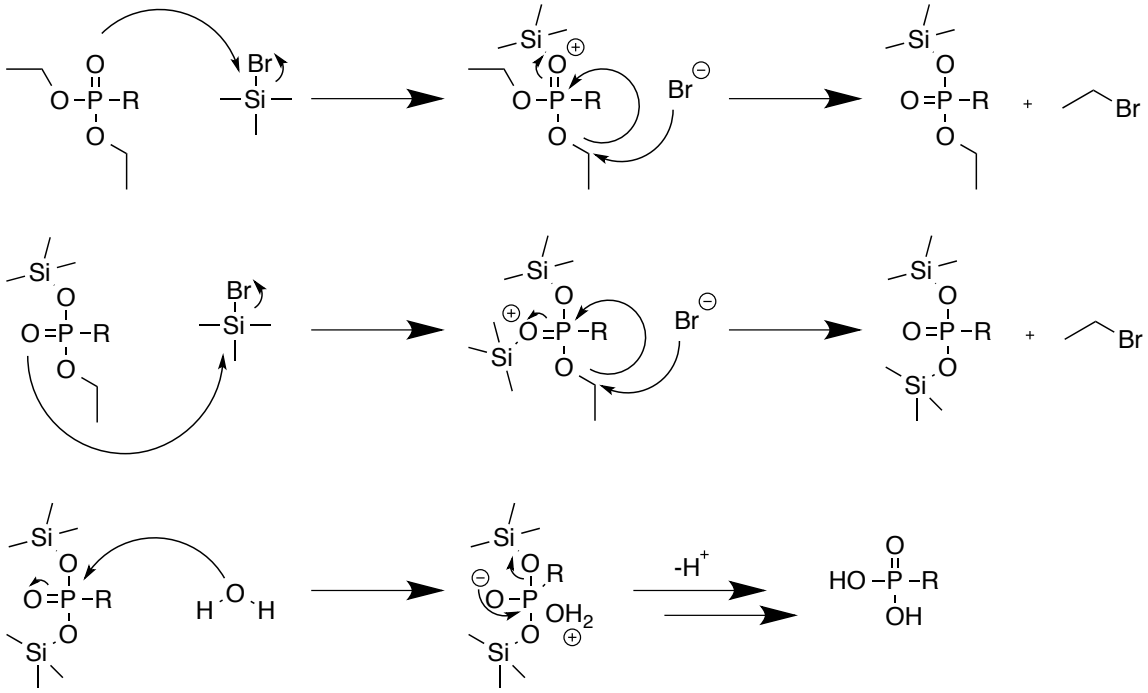

Scheme 1.2 Deprotection mechanism of phosphonate ester using bromotrimethylsilane and water to generate phosphonic acid.

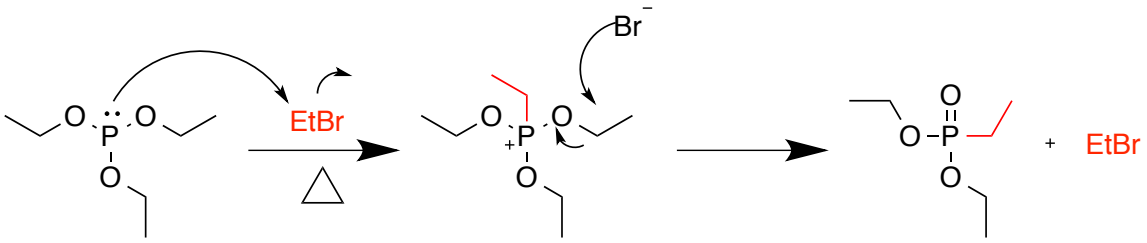

Scheme 1.3 Mechanism of forming ethyl diethylphosphonate, a common side reaction of the Michaelis-Arbuzov reaction using triethylphosphite.

The remaining chapters in this thesis cover works relate to the SAMs formed via various organic phosphonic acids on the NMC cathode to understand the effects of the various organic phosphonate coatings.

1.6 References

1. Hausbrand, R.; Cherkashinin, G.; Ehrenberg, H.; Gröting, M.; Albe, K.; Hess, C.; Jaegermann, W., Fundamental degradation mechanisms of layered oxide Li-ion battery cathode materials: Methodology, insights and novel approaches. *Mater. Sci. Eng., B* **2015,** *192*, 3-25.

2. Qian, J.; Henderson, W. A.; Xu, W.; Bhattacharya, P.; Engelhard, M.; Borodin, O.; Zhang, J. G., High rate and stable cycling of lithium metal anode. *Nat. Commun.* **2015,** *6*, 6362.

3. Amine, K.; Kanno, R.; Tzeng, Y., Rechargeable lithium batteries and beyond: Progress, challenges, and future directions. *MRS Bull.* **2014,** *39* (05), 395-401.

4. Fu, L. J.; Liu, H.; Li, C.; Wu, Y. P.; Rahm, E.; Holze, R.; Wu, H. Q., Surface modifications of electrode materials for lithium ion batteries. *Solid State Sci.* **2006,** *8* (2), 113-128.

5. Liang, Z.; Lin, D.; Zhao, J.; Lu, Z.; Liu, Y.; Liu, C.; Lu, Y.; Wang, H.; Yan, K.; Tao, X.; Cui, Y., Composite lithium metal anode by melt infusion of lithium into a 3D conducting scaffold with lithiophilic coating. *Proc. Natl. Acad. Sci. U.S.A.* **2016,** *113* (11), 2862-7.

6. Kim, H.; Jeong, G.; Kim, Y. U.; Kim, J. H.; Park, C. M.; Sohn, H. J., Metallic anodes for next generation secondary batteries. *Chem. Soc. Rev.* **2013,** *42* (23), 9011-9034.

7. Cheng, X. B.; Peng, H. J.; Huang, J. Q.; Wei, F.; Zhang, Q., Dendrite-Free Nanostructured Anode: Entrapment of Lithium in a 3D Fibrous Matrix for Ultra-Stable Lithium-Sulfur Batteries. *Small* **2014,** *10* (21), 4257-4263.

8. Kang, H. K.; Woo, S. G.; Kim, J. H.; Lee, S. R.; Kim, Y. J., Conductive porous carbon film as a lithium metal storage medium. *Electrochim. Acta* **2015,** *176*, 172-178.

9. Nitta, N.; Wu, F.; Lee, J. T.; Yushin, G., Li-ion battery materials: present and future. *Mater. Today* **2015,** *18* (5), 252-264.

10. Scrosati, B.; Garche, J., Lithium batteries: Status, prospects and future. *J. Power Sources* **2010,** *195* (9), 2419-2430.

11. Winter, M.; Besenhard, J. O.; Spahr, M. E.; Novak, P., Insertion electrode materials for rechargeable lithium batteries. *Adv. Mater.* **1998,** *10* (10), 725-763.

12. Kraytsberg, A.; Ein-Eli, Y., Higher, Stronger, Better… A Review of 5 Volt Cathode Materials for Advanced Lithium-Ion Batteries. *Adv. Energy Mater.* **2012,** *2* (8), 922-939.

13. Goodenough, J. B.; Kim, Y., Challenges for Rechargeable Li Batteries†. *Chem. Mater.* **2010,** *22* (3), 587-603.

14. John, B. G., Evolution of Strategies for Modern Rechargeable Batteries. *Acc. Chem. Res.* **2013,** *46*, 1053.

15. Choi, N.-S.; Han, J.-G.; Ha, S.-Y.; Park, I.; Back, C.-K., Recent advances in the electrolytes for interfacial stability of high-voltage cathodes in lithium-ion batteries. *RSC Adv.* **2015,** *5* (4), 2732-2748.

16. Fong, R.; Vonsacken, U.; Dahn, J. R., Studies of Lithium Intercalation into Carbons Using Nonaqueous Electrochemical-Cells. *J. Electrochem. Soc.* **1990,** *137* (7), 2009-2013.

17. Yazami, R., Surface chemistry and lithium storage capability of the graphite-lithium electrode. *Electrochim. Acta* **1999,** *45* (1-2), 87-97.

18. Vogdanis, L.; Martens, B.; Uchtmann, H.; Hensel, F.; Heitz, W., SYNTHETIC AND THERMODYNAMIC INVESTIGATIONS IN THE POLYMERIZATION OF ETHYLENE CARBONATE. *Makromol. Chem.* **1990,** *191* (3), 465-472.

19. Plakhotnyk, A. V.; Ernst, L.; Schmutzler, R., Hydrolysis in the system LiPF6-propylene carbonate-dimethyl carbonate-H2O. *J. Fluorine Chem.* **2005,** *126* (1), 27-31.

20. Monroe, C.; Newman, J., The impact of elastic deformation on deposition kinetics at lithium/polymer interfaces. *J. Electrochem. Soc.* **2005,** *152* (2), A396-A404.

21. Khurana, R.; Schaefer, J. L.; Archer, L. A.; Coates, G. W., Suppression of Lithium Dendrite Growth Using Cross-Linked Polyethylene/Poly(ethylene oxide) Electrolytes: A New Approach for Practical Lithium-Metal Polymer Batteries. *J. Am. Chem. Soc.* **2014,** *136* (20), 7395-7402.

22. Stone, G. M.; Mullin, S. A.; Teran, A. A.; Hallinan, D. T., Jr.; Minor, A. M.; Hexemer, A.; Balsara, N. P., Resolution of the Modulus versus Adhesion Dilemma in Solid Polymer Electrolytes for Rechargeable Lithium Metal Batteries. *J. Electrochem. Soc.* **2012,** *159* (3), A222-A227.

23. Schulze, M. W.; McIntosh, L. D.; Hillmyer, M. A.; Lodge, T. P., High-Modulus, High-Conductivity Nanostructured Polymer Electrolyte Membranes via Polymerization-Induced Phase Separation. *Nano Lett.* **2014,** *14* (1), 122-126.

24. Kobayashi, N.; Uchiyama, M.; Tsuchida, E., POLY LITHIUM METHACRYLATE-CO-OLIGO(OXYETHYLENE)METHACRYLATE AS A SOLID ELECTROLYTE WITH HIGH IONIC-CONDUCTIVITY. *Solid State Ionics* **1985,** *17* (4), 307-311.

25. Tsuchida, E.; Kobayashi, N.; Ohno, H., SINGLE-ION CONDUCTION IN POLY (OLIGO(OXYETHYLENE)METHACRYLATE)-CO-(ALKALI-METAL METHACRYLATES). *Macromolecules* **1988,** *21* (1), 96-100.

26. Ryu, S. W.; Mayes, A. M., Synthesis and properties of heptadecane-functionalized poly(propylene oxide) based single-ion polymer electrolytes. *Polymer* **2008,** *49* (9), 2268-2273.

27. Ohzuku, T.; Brodd, R. J., An overview of positive-electrode materials for advanced lithium-ion batteries. *J. Power Sources* **2007,** *174* (2), 449-456.

28. Islam, M. S.; Fisher, C. A., Lithium and sodium battery cathode materials: computational insights into voltage, diffusion and nanostructural properties. *Chem. Soc. Rev.* **2014,** *43* (1), 185-204.

29. Li, Y.; Meyer, S.; Lim, J.; Lee, S. C.; Gent, W. E.; Marchesini, S.; Krishnan, H.; Tyliszczak, T.; Shapiro, D.; Kilcoyne, A. L.; Chueh, W. C., Effects of Particle Size, Electronic Connectivity, and Incoherent Nanoscale Domains on the Sequence of Lithiation in LiFePO(4) Porous Electrodes. *Adv. Mater.* **2015,** *27* (42), 6591-7.

30. Manthiram, A., Materials Challenges and Opportunities of Lithium Ion Batteries. *J. Phys. Chem. Lett.* **2011,** *2* (3), 176-184.

31. Wu, Z.; Ji, S.; Zheng, J.; Hu, Z.; Xiao, S.; Wei, Y.; Zhuo, Z.; Lin, Y.; Yang, W.; Xu, K.; Amine, K.; Pan, F., Prelithiation Activates Li(Ni0.5Mn0.3Co0.2)O2 for High Capacity and Excellent Cycling Stability. *Nano Lett.* **2015,** *15* (8), 5590-6.

32. Armand, M.; Endres, F.; MacFarlane, D. R.; Ohno, H.; Scrosati, B., Ionic-liquid materials for the electrochemical challenges of the future. *Nat. Mater.* **2009,** *8* (8), 621-9.

33. Yoshida, T.; Takahashi, M.; Morikawa, S.; Ihara, C.; Katsukawa, H.; Shiratsuchi, T.; Yamaki, J.-i., Degradation Mechanism and Life Prediction of Lithium-Ion Batteries. *J. Electrochem. Soc.* **2006,** *153* (3), A576.

34. Xu, K.; von Cresce, A., Interfacing electrolytes with electrodes in Li ion batteries. *J. Mater. Chem.* **2011,** *21* (27), 9849.

35. Aravindan, V.; Gnanaraj, J.; Madhavi, S.; Liu, H. K., Lithium-ion conducting electrolyte salts for lithium batteries. *Chem. - Eur. J.* **2011,** *17* (51), 14326-46.

36. Xu, K., Nonaqueous liquid electrolytes for lithium-based rechargeable batteries. *Chem. Rev.* **2004,** *104* (10), 4303-417.

37. Bloom, I.; Trahey, L.; Abouimrane, A.; Belharouak, I.; Zhang, X.; Wu, Q.; Lu, W.; Abraham, D. P.; Bettge, M.; Elam, J. W.; Meng, X.; Burrell, A. K.; Ban, C.; Tenent, R.; Nanda, J.; Dudney, N., Effect of interface modifications on voltage fade in 0.5Li2MnO3·0.5LiNi0.375Mn0.375Co0.25O2 cathode materials. *J. Power Sources* **2014,** *249*, 509-514.

38. Bruce, P. G.; Armstrong, A. R.; Gitzendanner, R. L., New intercalation compounds for lithium batteries: layered LiMnO2. *J. Mater. Chem.* **1999,** *9* (1), 193-198.

39. Armstrong, A. R.; Robertson, A. D.; Bruce, P. G., Structural transformation on cycling layered Li(Mn1-yCoy)O-2 cathode materials. *Electrochim. Acta* **1999,** *45* (1-2), 285-294.

40. Yang, L.; Ravdel, B.; Lucht, B. L., Electrolyte Reactions with the Surface of High Voltage LiNi0.5Mn1.5O4 Cathodes for Lithium-Ion Batteries. *Electrochem. Solid-State Lett.* **2010,** *13* (8), A95-A97.

41. Zhang, Z. C.; Hu, L. B.; Wu, H. M.; Weng, W.; Koh, M.; Redfern, P. C.; Curtiss, L. A.; Amine, K., Fluorinated electrolytes for 5 V lithium-ion battery chemistry. *Energy Environ. Sci.* **2013,** *6* (6), 1806-1810.

42. Yabuuchi, N.; Yoshii, K.; Myung, S. T.; Nakai, I.; Komaba, S., Detailed Studies of a High-Capacity Electrode Material for Rechargeable Batteries, Li2MnO3-LiCo1/3Ni1/3Mn1/3O2. *J. Am. Chem. Soc.* **2011,** *133* (12), 4404-4419.

43. Hy, S.; Felix, F.; Rick, J.; Su, W. N.; Hwang, B. J., Direct In situ Observation of Li2O Evolution on Li-Rich High-Capacity Cathode Material, Li NixLi(1-2x)/3Mn(2-x)/3 O-2 (0 <= x <= 0.5). *J. Am. Chem. Soc.* **2014,** *136* (3), 999-1007.

44. Woodford, W. H.; Carter, W. C.; Chiang, Y.-M., Design criteria for electrochemical shock resistant battery electrodes. *Energy Environ. Sci.* **2012,** *5* (7), 8014.

45. Zhu, M.; Park, J.; Sastry, A. M., Fracture Analysis of the Cathode in Li-Ion Batteries: A Simulation Study. *J. Electrochem. Soc.* **2012,** *159* (4), A492.

46. Croguennec, L.; Palacin, M. R., Recent achievements on inorganic electrode materials for lithium-ion batteries. *J. Am. Chem. Soc.* **2015,** *137* (9), 3140-56.

47. Li, J.; Zhang, Q.; Xiao, X.; Cheng, Y. T.; Liang, C.; Dudney, N. J., Unravelling the Impact of Reaction Paths on Mechanical Degradation of Intercalation Cathodes for Lithium-Ion Batteries. *J. Am. Chem. Soc.* **2015,** *137* (43), 13732-5.

48. Su, Y.; Cui, S.; Zhuo, Z.; Yang, W.; Wang, X.; Pan, F., Enhancing the High-Voltage Cycling Performance of LiNi0.5Mn0.3Co0.2O2 by Retarding Its Interfacial Reaction with an

Electrolyte by Atomic-Layer-Deposited Al2O3. *ACS. Appl. Mater. Interfaces* **2015,** *7* (45), 25105-12.

49. Li, X.; Liu, J.; Meng, X.; Tang, Y.; Banis, M. N.; Yang, J.; Hu, Y.; Li, R.; Cai, M.; Sun, X., Significant impact on cathode performance of lithium-ion batteries by precisely controlled metal oxide nanocoatings via atomic layer deposition. *J. Power Sources* **2014,** *247*, 57-69.

50. Kim, J. W.; Kim, D. H.; Oh, D. Y.; Lee, H.; Kim, J. H.; Lee, J. H.; Jung, Y. S., Surface chemistry of LiNi0.5Mn1.5O4 particles coated by Al2O3 using atomic layer deposition for lithium-ion batteries. *J. Power Sources* **2015,** *274*, 1254-1262.

51. Sun, Y. K.; Lee, M. J.; Yoon, C. S.; Hassoun, J.; Amine, K.; Scrosati, B., The role of AlF3 coatings in improving electrochemical cycling of Li-enriched nickel-manganese oxide electrodes for Li-ion batteries. *Adv. Mater.* **2012,** *24* (9), 1192-6.

52. Huang, Y.; Chen, J.; Ni, J.; Zhou, H.; Zhang, X., A modified ZrO2-coating process to improve electrochemical performance of Li(Ni1/3Co1/3Mn1/3)O2. *J. Power Sources* **2009,** *188* (2), 538-545.

53. Quinlan, R. A.; Lu, Y.-C.; Kwabi, D.; Shao-Horn, Y.; Mansour, A. N., XPS Investigation of the Electrolyte Induced Stabilization of LiCoO2and “AlPO4”-Coated LiCoO2Composite Electrodes. *J. Electrochem. Soc.* **2015,** *163* (2), A300-A308.

54. Leskela, M.; Ritala, M., Atomic layer deposition chemistry: recent developments and future challenges. *Angew. Chem. Int. Ed. Engl.* **2003,** *42* (45), 5548-54.

55. Zhong, Z. Y.; Yin, Y. D.; Gates, B.; Xia, Y. N., Preparation of mesoscale hollow spheres of TiO2 and SnO2 by templating against crystalline arrays of polystyrene beads. *Adv. Mater.* **2000,** *12* (3), 206-+.

56. Li, H.; Zhou, H., Enhancing the performances of Li-ion batteries by carbon-coating: present and future. *Chem. Commun.* **2012,** *48* (9), 1201-17.

57. Lee, S.; Cho, Y.; Song, H.-K.; Lee, K. T.; Cho, J., Carbon-Coated Single-Crystal LiMn2O4 Nanoparticle Clusters as Cathode Material for High-Energy and High-Power Lithium-Ion Batteries. *Angew. Chem. Int. Ed.* **2012,** *51* (35), 8748-8752.

58. Zhi, X.; Liang, G.; Wang, L.; Ou, X.; Gao, L.; Jie, X., Optimization of carbon coatings on LiFePO4: Carbonization temperature and carbon content. *J. Alloys Compd.* **2010,** *503* (2), 370-374.

59. Wilcox, J. D.; Doeff, M. M.; Marcinek, M.; Kostecki, R., Factors influencing the quality of carbon coatings on LiFePO4. *J. Electrochem. Soc.* **2007,** *154* (5), A389-A395.

60. Ng, S. H.; Wang, J.; Wexler, D.; Chew, S. Y.; Liu, H. K., Amorphous carbon-coated silicon nanocomposites: A low-temperature synthesis via spray pyrolysis and their application as high-capacity anodes for lithium-ion batteries. *J. Phys. Chem. C* **2007,** *111* (29), 11131-11138.

61. Cho, Y.-D.; Fey, G. T.-K.; Kao, H.-M., The effect of carbon coating thickness on the capacity of LiFePO4/C composite cathodes. *J. Power Sources* **2009,** *189* (1), 256-262.

62. Oh, S. W.; Myung, S.-T.; Oh, S.-M.; Oh, K. H.; Amine, K.; Scrosati, B.; Sun, Y.-K., Double Carbon Coating of LiFePO4 as High Rate Electrode for Rechargeable Lithium Batteries. *Adv. Mater.* **2010,** *22* (43), 4842-+.

63. Amine, K.; Liu, J.; Belharouak, I., High-temperature storage and cycling of C-LiFePO4/graphite Li-ion cells. *Electrochem. Commun.* **2005,** *7* (7), 669-673.

64. Zhang, S. S., A review on electrolyte additives for lithium-ion batteries. *J. Power Sources* **2006,** *162* (2), 1379-1394.

65. Abe, K.; Ushigoe, Y.; Yoshitake, H.; Yoshio, M., Functional electrolytes: Novel type additives for cathode materials, providing high cycleability performance. *J. Power Sources* **2006,** *153* (2), 328-335.

66. Takechi, K. A., JP), Koiwai, Akihiko (Aichi, JP), Shiga, Tohru (Aichi, JP) Nonaqueous electrolytic solution for battery and nonaqueous electrolytic solution battery. US6077628 A, 2000.

67. Takechi, K. A., JP), Shiga, Tohru (Aichi, JP) Nonaqueous electrolytic solution for battery and nonaqueous electrolytic solution battery using the same. US6235431 B1, 2001.

68. Amine, K.; Liu, J.; Kang, S.; Belharouak, I.; Hyung, Y.; Vissers, D.; Henriksen, G., Improved lithium manganese oxide spinel/graphite Li-ion cells for high-power applications. *J. Power Sources* **2004,** *129* (1), 14-19.

69. Chen, Z. H.; Lu, W. Q.; Liu, J.; Amine, K., LiPF6/LiBOB blend salt electrolyte for high-power lithium-ion batteries. *Electrochim. Acta* **2006,** *51* (16), 3322-3326.

70. Mao, H.; Wainwright, D. S., Polymerizable additives for making non-aqueous rechargeable lithium batteries safe after overcharge. Google Patents: 2000.

71. Abouimrane, A.; Odom, S. A.; Tavassol, H.; Schulmerich, M. V.; Wu, H.; Bhargava, R.; Gewirth, A. A.; Moore, J. S.; Amine, K., 3-Hexylthiophene as a Stabilizing Additive for High Voltage Cathodes in Lithium-Ion Batteries. *J. Electrochem. Soc.* **2012,** *160* (2), A268-A271.

72. Choi, J. A.; Eo, S. M.; MacFarlane, D. R.; Forsyth, M.; Cha, E.; Kim, D. W., Effect of organic additives on the cycling performances of lithium metal polymer cells. *J. Power Sources* **2008,** *178* (2), 832-836.

73. Dahn, J. R.; Jiang, J. W.; Moshurchak, L. M.; Fleischauer, M. D.; Buhrmester, C.; Krause, L. J., High-rate overcharge protection of LiFePO4-based Li-ion cells using the redox

shuttle additive 2,5-ditertbutyl-1,4-dimethoxybenzene. *J. Electrochem. Soc.* **2005,** *152* (6), A1283-A1289.

74. Moshurchak, L. M.; Buhrmester, C.; Dahn, J. R., Spectroelectrochemical studies of redox shuttle overcharge additive for LiFePO4-based Li-ion batteries. *J. Electrochem. Soc.* **2005,** *152* (6), A1279-A1282.

75. Adachi, M.; Tanaka, K.; Sekai, K., Aromatic compounds as redox shuttle additives for 4 V class secondary lithium batteries. *J. Electrochem. Soc.* **1999,** *146* (4), 1256-1261.

76. Haregewoin, A. M.; Wotango, A. S.; Hwang, B.-J., Electrolyte additives for lithium ion battery electrodes: progress and perspectives. *Energy Environ. Sci.* **2016,** *9* (6), 1955-1988.

77. Vercelli, B.; Zotti, G.; Schiavon, G.; Zecchin, S.; Berlin, A., Adsorption of hexylferrocene phosphonic acid on indium-tin oxide electrodes. Evidence of strong interchain interactions in ferrocene self-assembled monolayers. *Langmuir* **2003,** *19* (22), 9351-9356.

78. Van Alsten, J. G., Self-assembled monolayers on engineering metals: Structure, derivatization, and utility. *Langmuir* **1999,** *15* (22), 7605-7614.

79. Thissen, P.; Valtiner, M.; Grundmeier, G., Stability of phosphonic acid self-assembled monolayers on amorphous and single-crystalline aluminum oxide surfaces in aqueous solution. *Langmuir* **2010,** *26* (1), 156-64.

80. Pawsey, S.; Yach, K.; Reven, L., Self-assembly of carboxyalkylphosphonic acids on metal oxide powders. *Langmuir* **2002,** *18* (13), 5205-5212.

81. Mutin, P. H.; Guerrero, G.; Vioux, A., Hybrid materials from organophosphorus coupling molecules. *J. Mater. Chem.* **2005,** *15* (35-36), 3761.

82. Gao, W.; Dickinson, L.; Grozinger, C.; Morin, F. G.; Reven, L., Self-assembled monolayers of alkylphosphonic acids on metal oxides. *Langmuir* **1996,** *12* (26), 6429-6435.

83. Jadhav, S. A., Self-assembled monolayers (SAMs) of carboxylic acids: an overview. *Cent. Eur. J. Chem.* **2011,** *9* (3), 369-378.

84. Bhattacharya, A. K.; Thyagarajan, G., The Michaelis-Arbuzov Rearrangement. *Chem. Rev.* **1981,** *81* (4), 415-430.

CHAPTER 2

IMPROVING $LiNi_{0.5}Mn_{0.3}Co_{0.2}O_2$ CATHODE PERFORMANCE WITH SURFACE-BOUND SEMICONDUCTING POLYMER COATINGS

2.1 Introduction

Numerous consumer electronics and gas–electric hybrid vehicles rely on lightweight, high energy density batteries.[1] The most widely used and studied class of secondary (rechargeable) batteries is based on lithium metal or other lithiated anodes juxtaposed against intercalation–type cathodes, which are spatially separated by an ion transporting liquid electrolyte. These electrochemical cells exhibit high energy densities that arise from the low standard reduction potential of metallic lithium and its small atomic mass. However, the low storage capacities of these cells coupled with their inadequate deliverable power limit the utilization of lithium–ion batteries in electric vehicles and in electrical grid storage devices crucial for the efficient utilization of intermittent electricity derived from solar and wind energies. Thus, two major thrusts in Li–ion battery research focus on the development and safe implementation of: (1) "high voltage" cathodes that undergo reversible lithium intercalation at oxidizing potentials ≥ 3.8 V (versus Li/Li^+),[2-4] and (2) high capacity anodes with low standard reduction potentials, such as lithium metal, or lithiated silicon or germanium.[2, 5] Advances in both research thrusts may potentially broaden the applications of Li–ion batteries, since increasing both the electrochemical potential difference between the cathode and anode and the maximum current capacity will augment their deliverable power.

Typical cathode materials in Li–ion batteries are 2D–layered inorganic oxides, into which lithium ions intercalate and de–intercalate upon discharging and charging of the electrochemical cell, respectively.[6] The most commonly used metal oxide cathode material in consumer electronics is $LiCoO_2$, which furnishes a cell voltage of ~3.6 V and a theoretical capacity of 140 mA•h/g.[3, 5, 7] Replacement of a portion of the cobalt sites in $LiCoO_2$ with Ni and Mn yields $LiNi_xMn_yCo_{1-x-y}O_2$ (NMC), which exhibits higher, composition–dependent intercalation voltages ranging 3.8–4.3 V with a higher theoretical capacity of ~250 mA•h/g.[3-5, 7-8] The higher intercalation voltage arises from changes in the potentials at which the Ni, Mn, and Co sites undergo reversible oxidation/reduction.

While the capacity and cathode intercalation voltage set the theoretical maximum power deliverable by a battery under optimal conditions, real lithium–ion battery electrodes are porous composites comprising the active material (e.g., NMC or lithiated silicon) embedded in a high dielectric poly(vinylidene difluoride) (PVDF) matrix binder that contains electrically conductive carbon black (CB). In order to facilitate efficient electron transfer between the active electrode material and the electrode current collector, the CB must form a percolating, electrically conductive network. Increasing the CB concentration in a composite cathode thus enhances the charge and discharge rate performance of a cathode, enabling rapid cell charge and discharge ideal for electric vehicle applications. However, increasing the CB content reduces both the volumetric and gravimetric energy density of the battery.[9] Thus, reducing the amount of CB incorporated into the cathode would increase the overall energy density of the cell. In the case of anodes, the groups of Liu[10-12] and Balsara[13] have independently demonstrated the utility of multifunctional polymeric binders based on semiconducting polymer backbones that adhere to

the active anode material surfaces to yield electrically and ionically conductive composite electrodes. However, similar strategies have not yet been extensively explored in the context of high voltage cathode materials.

Another barrier confronting the implementation of NMC cathode materials is their significant irreversible capacity fade upon repeated charge–discharge cycling.[14-16] This irreversible capacity loss stems from a combination of cathode particle surface reconstruction due to Mn ion dissolution into the organic electrolyte, coupled with the intrinsic reactivity of the $LiPF_6$/organic carbonate electrolytes with the cathode surface. The latter irreversible reactions consume lithium ions and lead to the deposition of high impedance, solid–electrolyte interphase (SEI) layers at the cathode surface, which decrease battery cycling efficiency.[3-4, 7, 16-18] To mitigate these processes, numerous research groups have focused on coating NMC and other high voltage cathodes with electrically insulating, inorganic oxide materials that are Li–ion permeable.[19-21]

To address the challenges of developing composite cathodes that incorporate greater amounts of active material with reduced charge–discharge capacity fade, numerous groups have developed functional cathode coatings.[22-24] Recent work demonstrated that thin, conductive carbon coatings enhance the cycling and rate performance of Li–ion batteries.[25] The variable surface coverage and thickness of these coatings results in wide variation in the resulting cell performances,[26] and the carbonaceous nature of the coating limits the thermal processablities of these electrode materials.[25] Alternatively, various groups have pursued the *in situ* formation of conducting polymer coatings at the oxidizing cathode surface by electropolymerization of p–conjugated battery electrolyte additives during battery cycling.[27-30] While numerous examples of

the oxidative electropolymerization of thiophene–derived electrolyte additives have appeared, the lack of surface adhesion between the cathode and polymeric surface layer limits potential performance gains.

Herein, we report a new strategy for generating surface anchored, electropolymerizable coatings for NMC cathode particles, which reduce capacity fade upon repeated battery cycling with enhanced charge–discharge rate performances. Our approach is predicated on the design and synthesis of an oxidatively electropolymerizable monomer bearing a surface binding functionality. Charging the active NMC cathode material coated with a thin layer of this surface ligand induces its oxidative polymerization to form a p–doped semiconducting polymer layer that mitigates irreversible capacity losses due to surface reactions with the electrolyte, while also enhancing the rate and cycling performance of Li–ion half cells.

2.2 Experimental Section

Materials. All reagents were purchased from the Sigma–Aldrich Chemical Co. (Milwaukee, WI) and used as received unless noted. Anhydrous THF and CH_2Cl_2 were obtained by sparging analytical grade solvents for 30 min with $N_2(g)$, followed by cycling through a column of activated alumina in Vacuum Atmospheres Co. solvent purification systems. *N*–bromosuccinimide was recrystallized from H_2O, and triphenylphosphine was recrystallized from hexane prior to use. $LiNi_{0.5}Mn_{0.3}Co_{0.2}O_2$ (NMC) electrode powder and 1 M $LiPF_6$ in 50:50 *v*/*v* ethyl carbonate/diethyl carbonate electrolyte were supplied by The Dow Chemical Company (Midland, MI). CR2032 coin cell components (case, cap and gasket) were purchased from Pred Materials International. Celgard 2500 battery separators were cut into 1.9 cm diameter discs and

dried at 40 °C under full vacuum for 12 h prior to use. TIMCAL Super C 65 carbon black and SOLVAY Solef 5130 poly(vinylidene difluoride) (PVDF) were used as received. Platinum wire (0.5 mm in diameter, 25 cm long) and lithium foil (0.75mm thick) for cyclic voltammetry studies were purchased from Alfa Aesar (Ward Hill, MA). ITO glass slides (25 mm x 25 mm x 1.1 mm, surface resistivity 8 – 12 Ω/slide) was purchased from the Sigma–Aldrich Chemical Co. (Milwaukee, WI). Lithium foil (0.2 mm thick) for half–cell assembly was purchased from Rockwood Lithium (Kings Mountain, NC).

^{1}H NMR and ^{13}C NMR spectra were recorded in DMSO–d_6 or $CDCl_3$ at 25 °C on both Bruker AC+ 300a and Bruker Avance 500 spectrometers. All spectra were referenced to the residual solvent peaks in the samples. Elemental analyses (C, H and S) were performed by Atlantic Microlab, Inc. (Norcross, GA).

Synthesis of 2, 5–Dibromo–3–(2–hydroxy)ethylthiophene (1).[31] 3–thiophenethanol (2.60 g, 20.3 mmol) was added to a stirred solution of *N*–bromosuccinimide (9.05 g, 50.8 mmol) in anhydrous THF (65 mL) at ambient temperature. After 14 h, the reaction mixture was poured into CH_2Cl_2 (100 mL) and extracted with de–ionized water (3 x 100 mL). The organic layer was dried over $MgSO_4(s)$ and concentrated under reduced pressure by rotary evaporation to yield a yellow oil. This crude product was purified by column chromatography using a 1:4 *v*/*v* hexanes/ethyl acetate mixture. Yield: 2.56 g (57 %). ^{1}H NMR (300 MHz, $CDCl_3$) δ (ppm): 6.88 (*s*, 1H), 3.82 (*t*, *J* = 6.5 Hz, 2H), 2.81 (*t*, *J* = 6.5 Hz, 2H).

Synthesis of 3'–(2–Hydroxyethyl)–2, 2':5', 2''–terthiophene (2).[32] A degassed mixture of 1 M K_2CO_3 (*aq*) (17 mL) and 1,2 dimethoxyethane (34 mL) was added to a Schlenk flask charged with **1** (2.56 g, 8.95 mmol). Solid 2–thienylboronic acid (2.52 g, 19.7 mmol) and $(Ph_3P)_4Pd$ (1.03 g, 0.891 mmol) were then added to this reaction mixture under a flush of $N_2(g)$.

The sealed reaction mixture was stirred at 80 °C for 11 h. Upon cooling the reaction flask, the reaction mixture was poured into CH_2Cl_2 (100 mL) and extracted with de–ionized water (3 x 100 mL). The resulting organic layer was dried over $MgSO_4(s)$ and subsequently concentrated under reduced pressure to yield a yellow oil. The crude product was purified by column chromatography in pure CH_2Cl_2. Yield: 2.26 g (86 %). ^{1}H NMR (300 MHz, $CDCl_3$) δ (ppm): 7.34–7.01 (*m*, 7H), 3.92 (*q*, *J* = 6.5 Hz, 3H), 3.03 (*t*, *J* = 6.6 Hz, 2H), 1.47 (*t*, *J* = 5.8 Hz, 1H).

Synthesis of 3'–(2–Bromoethyl)–2, 2':5', 2''–terthiophene (3).[33] Solid CBr_4 (7.70 g, 23.2 mmol) and solid $(C_6H_5)_3P$ (6.04 g, 23.0 mmol) were added a solution of **2** (2.26 g, 7.73 mmol) in anhydrous THF (40 mL) at ambient temperature under nitrogen. After a 16 h reaction time, the reaction mixture was poured into CH_2Cl_2 (100 mL). After extraction with de–ionized water (3 x 100 mL) and subsequent drying of the organic layer over $MgSO_4(s)$, the crude product was isolated by rotary evaporation of the volatile solvent to yield a yellow oil. This crude product was purified by column chromatography in 9:1 *v*/*v* hexanes/CH_2Cl_2. Yield: 0.88 g (32 %). ^{1}H NMR (300 MHz, $CDCl_3$) δ (ppm): 7.35 –7.00 (*m*, 7H), 3.58 (*t*, *J* = 7.7 Hz, 2H), 3.31 (*t*, *J* = 7.8 Hz, 2H).

Synthesis of Diethyl 2–(3'–terthiophene)ethylphosphonate (4). Triethylphosphite (1.23 g, 7.40 mmol) and **3** (0.880 g, 2.47 mmol) were combined in a 100 mL Schlenk flask. This reaction mixture was stirred under a dynamic flow of nitrogen, while heating in a thermostatted oil bath at 150 °C for 16 h. The reaction mixture was vented through an oil bubbler into a saturated $K_2CO_3(aq)$ solution to trap the gaseous bromoethane reaction byproduct. The excess $(EtO)_3P$ was removed *in vacuo* to yield a yellow oil. This crude product was purified by column chromatography in 95:5 *v*/*v* ethyl acetate/methanol. Yield: 0.82 g (43 %). ^{1}H NMR (500 MHz, $CDCl_3$) δ (ppm): 7.33 (*dd*, *J* = 5.2, 1.2 Hz, 1H), 7.22 (*dd*, *J* = 5.2, 1.2 Hz, 1H), 7.16 (*dt*, *J* = 3.6,

1.3 Hz, 2H), 7.08 (*dd*, *J* = 5.1, 3.6 Hz, 1H), 7.04 – 7.01 (*m*, 2H), 4.25 – 3.98 (*m*, 4H), 3.15 – 2.93 (*m*, 2H), 2.19 – 1.96 (*m*, 2H), 1.32 (*t*, *J* = 7.0 Hz, 6H). ^{13}C NMR (125.7 MHz, $CDCl_3$) δ (ppm): 138.24, 138.09, 136.99, 135.90, 135.27, 128.05, 127.82, 126.35, 126.10, 125.89, 124.77, 123.94, 61.83, 61.78, 26.74 (*d*, *J* = 139.1 Hz), 22.46, 22.43, 16.65, 16.60.

Synthesis of Ethyl 3'–terthiophenephosphonic acid (TTePA). Bromotrimethylsilane (0.638 g, 4.17 mmol) was added dropwise by syringe to a solution of **4** (0.806 g, 1.95 mmol) in anhydrous CH_2Cl_2 (10 mL). After stirring this reaction mixture for 10 h at ambient temperature, volatiles were removed under reduced pressure. The reaction mixture was then treated with CH_3OH (10 mL) and stirred for an additional 2 h at 22 °C. CH_3OH was removed under reduced pressure and the crude product was purified by recrystallization from 40 mL of CH_3CN to yield a yellow solid. Yield: 0.575 g (84%). ^{1}H NMR (500 MHz, DMSO–d_6) δ (ppm): 7.64 (dd, *J* = 5.1, 1.2 Hz, 1H), 7.53 (dd, *J* = 5.1, 1.1 Hz, 1H), 7.33 (dd, *J* = 3.6, 1.2 Hz, 1H), 7.30 (s, 1H), 7.24 (dd, *J* = 3.7, 1.2 Hz, 1H), 7.16 (dd, *J* = 5.1, 3.6 Hz, 1H), 7.10 (dd, *J* = 5.1, 3.6 Hz, 1H), 2.95 – 2.86 (m, 2H), 2.50 (p, *J* = 1.8 Hz, 7H), 1.94 – 1.83 (m, 2H). ^{13}C NMR (125.7 MHz, $CDCl_3$): 139.44, 135.95, 134.49, 134.45, 128.73, 128.41, 128.22, 126.68, 126.23, 125.74, 124.24, 28.37 (d, *J* = 134.8 Hz), 22.78. *Anal*. Calc $C_{14}H_{13}O_3S_3P$: C, 47.18; H, 3.68; S, 26.99; Found: C, 46.92; H, 3.53; S, 26.69.

TTePA Surface Grafting Procedure. Model planar indium tin oxide (ITO) glass substrates (2.25 cm^2 total area each) were initially cleaned by simultaneous irradiation with 189.4 nm and 253.7 nm light in a Uvotech ProCleanerTM 110 UV–ozone cleaner for 15 min remove any organic surface contaminants and to maximize the surface hydroxyl group content. The ITO substrate was then immersed into a solution of **TTePA** (21.0 mg, 0.0589 mmol) in anhydrous ethanol (10 mL) for 5 min at ambient temperature. This solution concentration was selected to

reflect a 3–fold excess of **TTePA** required to form a compact monolayer of the surface ligand, assuming a binding area of 0.24 nm^2/phosphonic acid.[34] The ITO substrate was removed from the solution and dried under high vacuum at 140 °C for 48 h to drive the formation of metal–phosphonate surface linkages by dehydration. (Note: Thermogravimetric analyses under a $N_2(g)$ flow revealed that heating **TTePA** to $T > 170$ °C results in its thermal decomposition.) To remove any potential surface multilayers that may have formed during this ligand grafting process, the ITO substrate was sonicated for 1 h in a 95:5 *v/v* ethanol/Et_3N solution (10 mL). The sample was then washed with additional anhydrous ethanol (3 x 10 mL), followed by vacuum drying.

An analogous protocol was used to coat $LiNi_{0.5}Mn0_{.3}Co_{0.2}O_2$ (NMC, 2.0 g) powder. The surface area of the NMC is 0.5 m^2/g, according to BET analyses conducted at The Dow Chemical Company (Midland, MI). After UV–ozone surface cleaning of the cathode powder, a NMC slurry was coated with a solution of **TTePA** (34.0 mg, 0.0954 mmol) in anhydrous ethanol (10 mL) for 5 min at ambient temperature. NMC powder was isolated by centrifugation and decanting the resulting supernatant liquid.

Scanning Electron Microscopy (SEM) and Energy Dispersive X–ray Spectroscopy (EDS). SEM micrographs were captured using a LEO 1530–2 field–emission SEM using an accelerating voltage of 5.0 kV with backscattered electron detection (SE2 mode), which provides 2 nm resolution. EDS data were obtained using a ThermoFisher Ultra Dry EDS unit, using a beam energy of 20.0 kV.

X–ray Photoelectron Spectroscopy (XPS). XPS spectra of alkyl phosphonate–coated NMC powders were measured using a Thermo Fisher K–Alpha™ X–ray Photoelectron Spectrometer. Measurements utilized a monochromatic microfocus Al *K*a X–ray source (1486.6

eV) with a 400 μm spot size, an analyzer resolution of 0.1 eV, a pass energy of 20.0 eV, and a take–off angle of 90°. Each peak was referenced to the C (1s) at 284.5 eV. Peak positions and peak area ratios for S (2p) and P (2p) were calculated by baseline correction using the Smart function in the Thermo–Scientific Avantage software, fitting the observed peaks to a combined 30% Gaussian and 70% Lorentzian function, and normalization of the signals using the atomic sensitivity factors: 1.881 for S (2p), 1.353 for P (2p), and 18.235 for Co (2p) .

Cyclic Voltammetry (CV). Cyclic voltammetry (CV) was performed using an Autolab potentiostat 302N over the potential range of 3.0–4.3 V versus Li/Li^+ with a scan rate of 5 mV/s in an electrolyte comprising 1M $LiPF_6$ in 50:50 *v/v* ethyl carbonate:diethyl carbonate (2 mL). The electrochemical cell used in these studies was home–built to mimic a lithium–ion battery CR3032 coin cell geometry, in which lithium metal, Pt wire, and the **TTePA**–grafted ITO were the reference, counter, and working electrodes, respectively. Pt wire was electrochemically cleaned prior to CV experiments according to an established protocol.[35]

Cathode Disc Fabrication. Super C 65 carbon black (0.00978 g), a 8.2 wt % solution of PVDF in *N*–methyl pyrrolidone (0.9278 g), and NMP (0.4 mL) were combined in a Thinky Mixer ARE–310 at 2000 rpm for 4 min, followed by increasing the mixing speed to 2200 rpm for 30 sec. NMP (0.4 mL) was added to the resulting slurry, and the mixing protocol was repeated. NMC (2 g, either **TTePA**–grafted or uncoated) was then added to the slurry, and the mixing procedure was again repeated. The slurry was then cast onto 15 mm thick Al foil (MTI Corp., Richmond, CA) using an Elcometer 4340 Automatic Film Applicator. The resulting films were then dried under high vacuum at 40 °C for 16 h. 15 mm diameter electrode discs were punched from this solvent–cast electrode sheet, each of which was calendared under a force of 1.8 tons using a Carver 3851–0 melt press. Upon transferring the calendared electrodes to an

argon filled glovebox, the cathode discs were heated to 140 °C for 12 h under full vacuum to thoroughly dry them.

Half–Cell Assembly and Testing. CR2032–type lithium half–cells were assembled inside an argon–filled glovebox. At least 12 h prior to half–cell assembly, vacuum dried Celgard battery separators were immersed in the 1 M $LiPF_6$ in 50:50 *v*/*v* ethyl carbonate:diethyl carbonate electrolyte used in these cells. Each cathode disc was weighed prior to cell assembly, to enable accurate calculation of its theoretical specific capacity. The top cap of the CR2032 cell was loaded sequentially with a stainless steel spacer (16 mm diameter), a lithium foil electrode (16 mm diameter), 40 μl of electrolyte, a pre–soaked Celgard battery separator, a plastic gasket, 40 μl of electrolyte, and a cathode disc. Since the cathode discs curled slightly during the final vacuum drying in the glove box, they were flattened using plastic tweezers prior to placement in the cell. Finally, a stainless steel spacer was stacked on top of the cathode disc, followed by a stainless steel spring and the bottom cell cap. Cells were crimp sealed using a Hohsen automatic coin cell crimper (Osaka, Japan).

Half–cells were cycled between 3.0–4.3 V vs. Li/Li^+, using an Arbin Instruments BT2000 battery test station. Prior to any cycle testing, half–cells were initially conditioned by two cycles of charging and discharging at 0.1 C. Discharge capacity retention measurements employed a cell charge rate of 0.3 C and discharge rate of 1 C. Discharge rate performance tests utilized a 0.3 C charge rate and increasing discharge rates of 1, 2, 5, 8, and 10 C, followed by a final 1 C rate experiment to assess if the higher C rate tests irreversibly damaged the cells.

2.3 Results and Discussion

We envisioned the possibility of developing a NMC cathode surface coating that would minimize battery discharge capacity fade associated with parasitic electrolyte decomposition reactions, while also enabling reduction in the amount of carbon black required for electrical contact between the active NMC material and the current collector. Thus, we pursued the design and synthesis of a difunctional molecule bearing: (1) a chemical functionality that enabled the formation of strong, covalent bonds with the metal oxide surface, and (2) a conjugated headgroup that would undergo oxidative electropolymerization during battery charge–discharge cycles to form an electrically conductive polymer coating.

Against these cathode coating design constraints, we designed the terthiophene ethyl phosphonic acid (**TTePA)** surface ligand depicted in Scheme 1. Solution grafting of high purity organic molecules bearing carboxylic acid (COOH),[36] trichlorosilane ($–SiCl_3$),[37-38] and phosphonic acid ($–PO_3H_2$) functionalities onto metal oxide substrates enables the generation of covalently bound,[34, 39-42] molecular surface coatings of precisely tunable thicknesses.[31] Since phosphonic acids are easy to handle and well–known for their ability form covalently bound, self–assembled monolayers on metal oxides, we chose to incorporate a phosphonic acid functionality into **TTePA**. For the oxidatively electropolymerizable headgroup functionality, we considered various thiophene derivatives that would polymerize during battery cycling to yield a multivalent, semiconducting polythiophene surface coating. Previous studies established that monothiophenes oxidatively polymerize at potentials ≥ 4.3 V (versus Li/Li^+) in electrolytes based on 1 M $LiPF_6$ in organic carbonate solvents.[28-29] Unfortunately, these potentials are typically outside of the 3.0–4.3 V window in which the $LiNi_{0.5}Mn_{0.3}Co_{0.2}O_2$ (NMC) cathode

materials of interest are stable. However, oligothiophenes exhibit increased conjugation lengths and smaller band gaps, which render them oxidizable at lower potentials. In this vein, Xia *et al*. investigated terthiophene (a linear thiophene trimer) as a soluble electrolyte additive for improving $LiCoO_2$–based battery performance, due to its lower 3.8 V (v. Li/Li^+) onset potential for electropolymerization.[29] Therefore, we included a terthiophene functionality in the **TTePA** surface ligand.

Scheme 2.1. Synthesis of the multifunctional **TTePA** surface ligand.

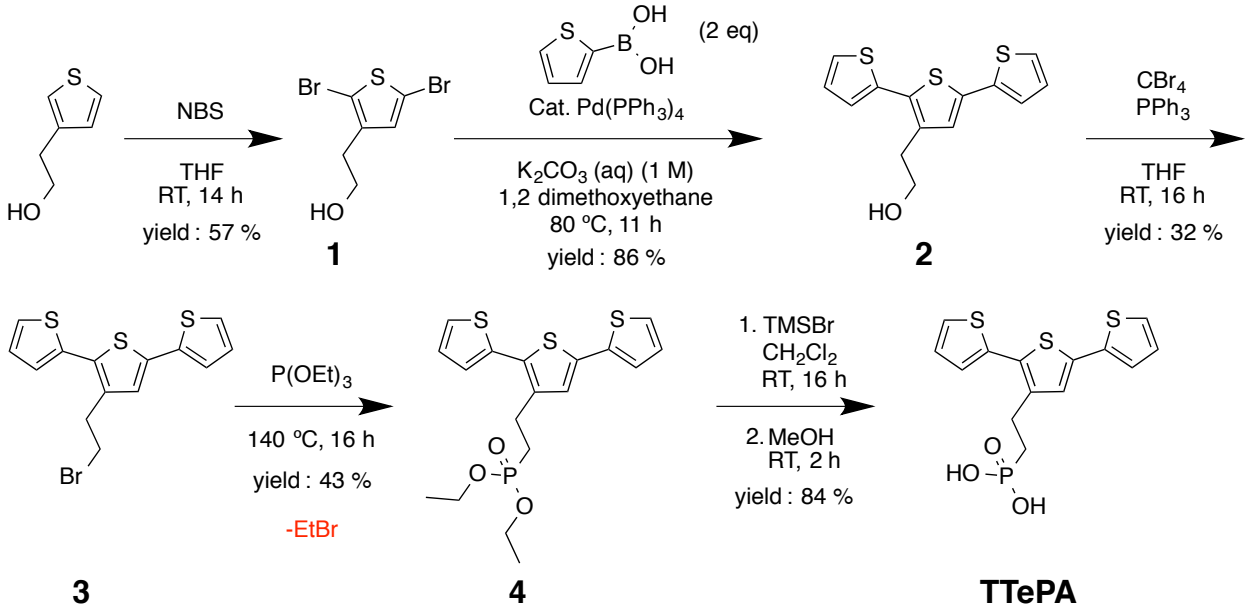

TTePA was synthesized in six steps from commercially available reagents in an overall 8 % yield, starting from commercially available 3–thiophene ethanol (Scheme 1). Dibromination of 3–thiophene ethanol with *N*–bromosuccinimide yielded 2,5–dibromothiophene ethanol (**1**),[31] which was carried into a $Pd(PPh3)_4$–catalyzed Suzuki coupling with two equivalents of 2–

thienylboronic acid to generate terthiophene **2** per the method of Wagner *et al*.[32] The pendant alcohol functionality in **2** was then transformed into alkyl bromide **3** using CBr_4/PPh_3 in THF, for use in a subsequent Michaelis–Arbuzov reaction with $P(OEt)_3$ at 140 °C to generate alkyl phosphonate diethyl ester **4**. We found that the yield in the Michaelis–Arbuzov transformation to generate **4** significantly improved by running the reaction under a dynamic nitrogen flow, in order to expel the volatile bromoethane reaction byproduct. If the bromoethane byproduct is not removed in this manner, it reacts with the excess $P(OEt)_3$ to lower the overall yield of **4** and to generate $EtP(OEt)_2$ as a persistent impurity. Treatment of **4** with excess $(CH_3)_3SiBr$ effected the deprotection of the ethyl ester to yield the desired **TTePA**, the chemical structure of which was confirmed by ^1H and ^{13}C NMR spectroscopy. The analytical purity of this product was established by elemental analysis.

In order to elucidate the electrochemical behavior of **TTePA** in a standard Li–ion battery electrolyte without any interference from other complex processes (*e.g.*, Li^+ intercalation), we initially grafted **TTePA** onto an electrically conductive, transparent indium tin oxide (ITO) glass blocking electrodes. Molecular layers of this surface ligand were generated by solution grafting **TTePA** from ethanolic solution, followed by heat treatment to effect covalent phosphonate bond formation with the ITO surface. After heat treatment, the substrates were sonicated with a mixture of 5 wt % Et_3N in ethanol to remove any potential multilayers that could have formed during solution surface ligand grafting.[43] X–ray photoelectron spectroscopy (XPS) analyses of these ligand–grafted substrates reveals the presence of signals associated with the P (2p) and S (2p) peaks (Figure 2.1). Normalization of these signals using the elemental sensitivity factors reveals that [P]:[S] = 1:3, as expected based on the chemical structure of **TTePA** (Figure 2.3).

Difficulties associated with assessing the exact number density of indium atoms at the surface coupled with the polycrystalline nature of the ITO substrate prevented quantitative analysis of the **TTePA** surface grafting density. Since previous reports[43] suggested that sonication of the grafted substrate in a 5 wt % Et_3N in ethanol removes any multilayers that may have formed, we assume the formation of a **TTePA** monolayer on the surface.

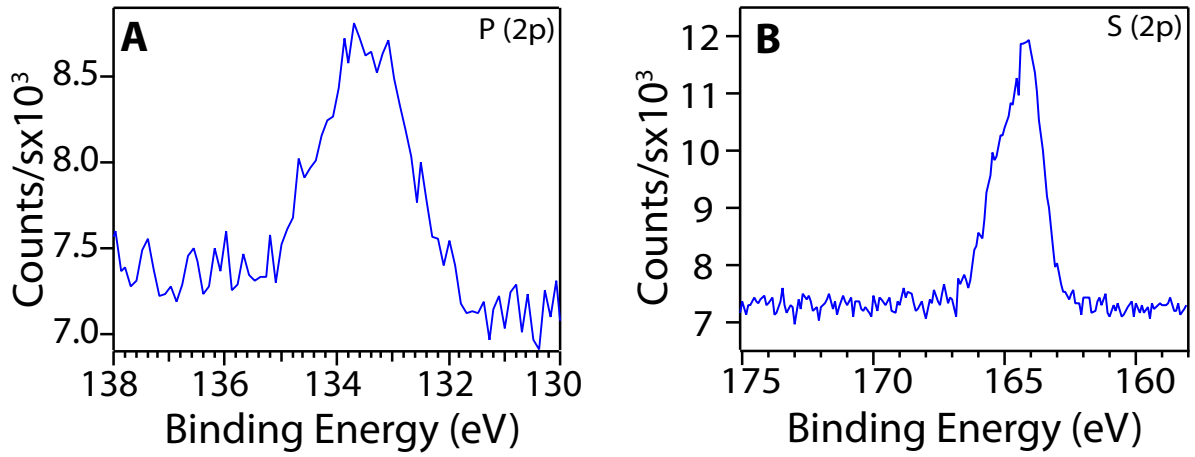

Figure 2.1. XPS spectra of ITO substrates bearing a surface grafted layer of **TTePA**, showing (A) the P (2p) and the (B) S (2p) peaks. Integration of the peak areas and normalization using the atomic sensitivity factors reveals the expected [P]:[S] = 1:3 atomic ratio.

Cyclic voltammetry (CV) studies of **TTePA**–grafted ITO substrates enabled determination of the oxidation potential of the surface–bound ligand, along with the electrochemical behavior of any resulting oligomeric surface layer. These three electrode measurements employed 1 M $LiPF_6$ in 50:50 *v/v* ethylene carbonate:diethyl carbonate as the electrolyte, with the ITO glass as the working electrode, Li metal as the reference electrode, and Pt wire as the counter electrode in an apparatus that mimicked the geometry of a CR2032 coin cell. In the first CV cycle sweeping from 3.4 to 4.3 V at a sweep rate of 5 mV/s, we observed an

oxidation wave with an onset potential of 3.7 V (Figure 2.2 a), which we ascribe to the oxidation of the surface bound **TTePA** monomer. Note that terthiophene oxidation apparently occurs at a potential that is ~0.1 V lower than that reported previously by Xia *et al*.[27] for terthiophene in 1 M $LiPF_6$ in a 30:70 *v/v* ethylene carbonate:diethyl carbonate electrolyte. We ascribe the lower observed onset potential in our system to differences in the exact electrolyte compositions. In the second CV sweep, we observe a new oxidation wave at 3.4 V, in addition to the wave at 3.7 V. We attribute the peak at 3.4 V to the formation of more readily oxidized oligothiophenes with longer conjugation lengths than the original terthiophene. The observed 0.3 V decrease in the oxidation onset potential is consistent with a previous report concerning the formation of polythiophene from terthiophene.[44] To emulate the conditions of an operating battery, we performed 50 consecutive CV scans. We observe that the parent terthiophene oxidation wave at 3.7 V completely disappears after 45 cycles (Figure 2.2 b), and that the only feature in the CV is a broad wave near 3.4 V associated with a polythiophene surface coating. Thus, the terthiophene monomer is completely consumed. Attempts to analyze the conjugation length of the polymeric surface layer using UV–Vis spectroscopy failed, due to significant overlap of the polythiophene absorption bands with those from the ITO substrate.

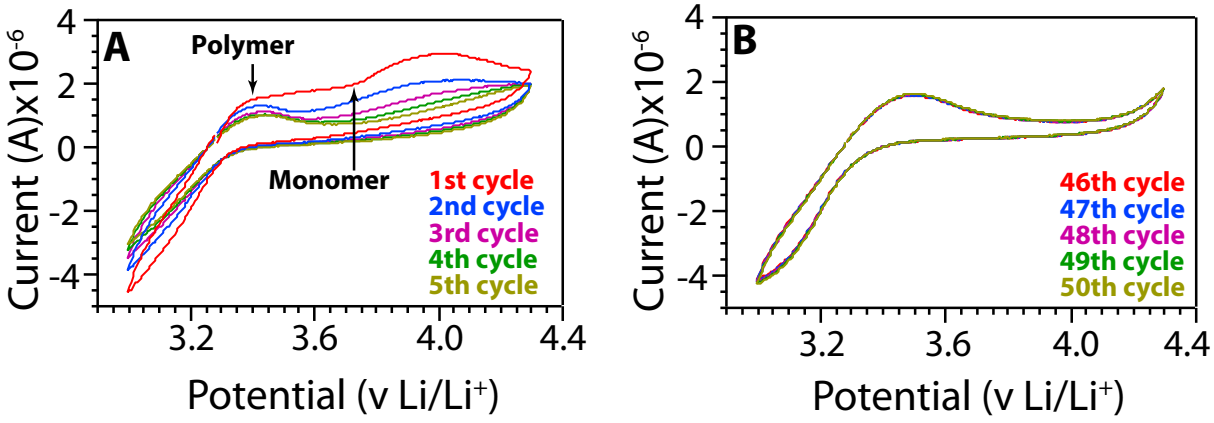

Figure 2.2 Cyclic voltammagrams for **TTePA**–coated planar ITO glass substrates depicting: (A) the first five CV cycles that exhibit peaks associated with the parent **TTePA** (~ 3.7 V versus Li/Li^+) and the polymeric **TTePA** oxidation (~3.4 V versus Li/Li^+), the latter of which appears only after the second cycle, and (B) the last five CV cycles, in which only the peak associated with polymeric **TTePA** remains. CV measurements employed 1 M $LiPF_6$ in 50:50 *v/v* ethylene carbonate/dimethyl carbonate electrolyte with a sweep rate of 5 mV/s over the range 3.0–4.3 V, with a Pt wire counter electrode and a Li reference electrode.

Armed with the knowledge that the terthiophene surface ligand undergoes oxidative polymerization at 3.7 V under conditions similar to an operating Li–ion battery, we proceeded to study the grafting of **TTePA** to the surfaces of $LiNi_{0.5}Mn0_{.3}Co_{0.2}O_2$ (NMC) high voltage cathode materials. An ethanolic solution grafting protocol analogous to that used for the ITO glass substrates enabled coating of the NMC with a covalently bound **TTePA** molecular surface layer. XPS analyses of the solution grafted NMC particles revealed the presence of both P (2p) and S (2p) peaks at 133.15 eV and 163.9 eV (Figure 2.3), which respectively correspond to a surface bound metal–phosphonate and the sulfur in a thiophene ring.[45-46] Quantitative integration of these peaks and normalization of their areas using the atomic sensitivity factors reveals that the atom percent ratio [P]:[S] = 1:3 as expected. Energy Dispersive X–ray Spectrscopy (EDS) analyses

further reveal that the uniform coating of the NMC particle surfaces with both P and S atoms, consistent with a homogeneous surface distribution of **TTePA** (Figure 2.4).

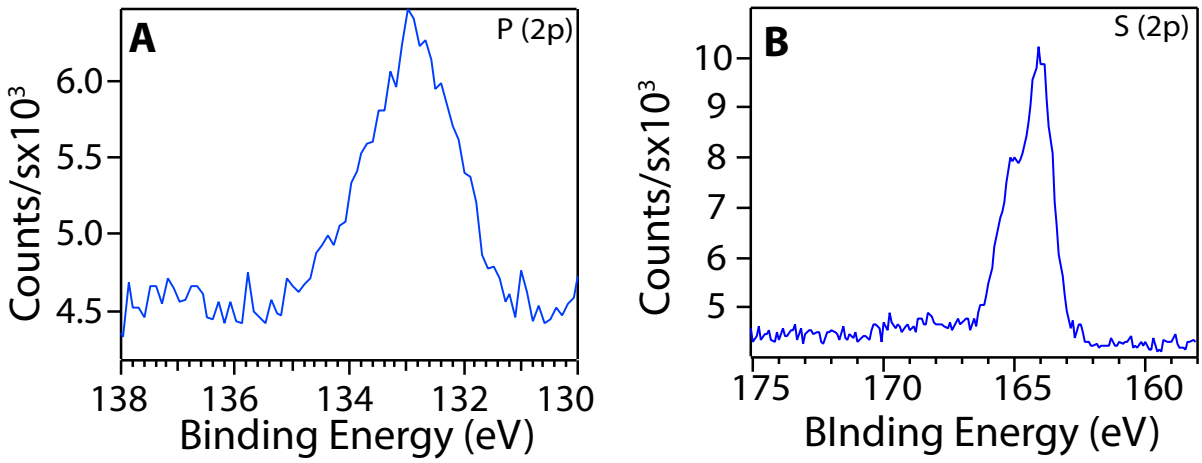

Figure 2.3. XPS spectra of **TTePA**–coated NMC, showing (A) the P (2p) peak at 133.15 eV, which corresponds to the expected energy of a metal–phosphonate, and (B) the S (2p) peak at 163.0 eV of the sulfur in a terthiophene ring system. The atom ratio [P]:[S] = 1:3 is that expected from the structure of the surface ligand.

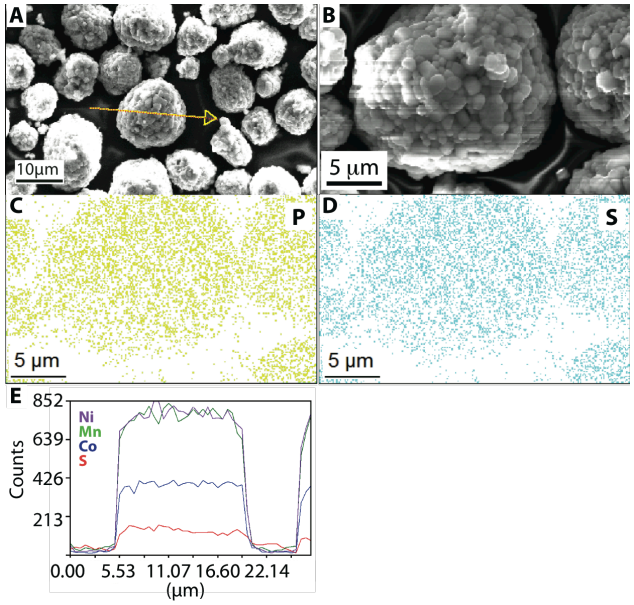

Figure 2.4. (A, B) SEM micrographs and (C) phosphorous and (D) sulfur EDS elemental

maps of **TTePA**–grafted NMC particles, and (E) an EDS line scan of TTePA grafted NMC, which indicate that the P and S are homogeneously distributed across the entire NMC surface.

The grafting density (n_F) of the surface bound **TTePA** on the NMC cathode particles was determined according to the following equation:[47]

$$n_F = \frac{l_P}{l_{Co}} \rho_{Co} \lambda_{Co} cos\ \theta = \frac{[P]}{[Co]} \rho_{Co} \lambda_{Co} cos\ \theta,$$

where l_P and l_{Co} are the sensitivity factor–normalized atom percent values for P (2p) and Co (2p) measured by XPS, r_{Co} = 5.9 atoms/nm^3 is the atomic number density of Co in NMC unit cell, l_{Co} = 1.287 nm is the inelastic mean free path of Co, and q = 90° is the XPS instrument take–off angle. XPS measurements of the coated NMC indicate that the (l_P/l_{Co}) = [P]:[Co] = 0.15, which leads to a calculated grafting density of 1.14 molecules/nm^2. We note that this value is significantly lower than the expected ~4 molecules/nm^2 for an ideal compact monolayer of a linear alkylphosphonate on a planar substrate.[48] We attribute this surface coverage discrepancy to the size of the terthiophene headgroup, which is calculated to have an area of 0.99 nm^2/molecule.[49] Upon accounting for this geometric difference between the occluded surface area of a linear alkyl phosphonate and that of **TTePA**, we calculate that a compact monolayer of **TTePA** should exhibit a grafting density of only 1.01 molecules/nm^2. The agreement between this last value and that deduced from XPS analyses strongly indicates the formation of a compact monolayer of **TTePA** at the NMC cathode particle surface.

Composite cathodes comprising **TTePA**–coated NMC cathode powders, carbon black, and a PVDF binder were fabricated for their electrochemical characterization in charge–discharge capacity cycling and discharge rate performance tests. Note that the NMC used in

composite cathode construction was fully lithiated. Consequently, we anticipated that the initial charging of the half–cells would lead to **TTePA** polymerization at 3.7 V prior to Li–ion de–intercalation at 3.8 V. The separation of the surface ligand electropolymerization and Li–ion de–intercalation potentials ensures the polymerization reaction does not interfere with the ion (de)intercalation process. Uncoated NMC cathodes were also produced using the same weight fractions of carbon black and PVDF binder.

Lithium half–cells were conditioned in triplicate by two initial cycles using a 0.1 C charge and 0.1 C discharge rate, prior to cycling 50 times using a 0.3 C charge and 1 C discharge rate to assess their relative performances. These charge–discharge cycling tests revealed that the **TTePA**–coated NMC composite cathodes exhibit improved discharge capacity retention as compared to the uncoated NMC (Figure 2.5). Based on our electrochemical characterization of the oxidative oligomerization of surface–bound **TTePA** on ITO glass, we attribute this improved half–cell cycling performance to the formation of a polythiophene coating on the NMC surface. We hypothesize that *in situ* polymerization of the **TTePA** surface layer on the cathode particle surface creates a thin shroud that minimizes parasitic electrolyte oxidation reactions that consume lithium, by physically blocking electrolyte/electrode surface contact. The multivalent surface coating may also help to maintain the integrity of the cathode particles during cycling, in spite of the ~10% volume change in the cathode particles during Li–ion (de)intercalation.[50-51]

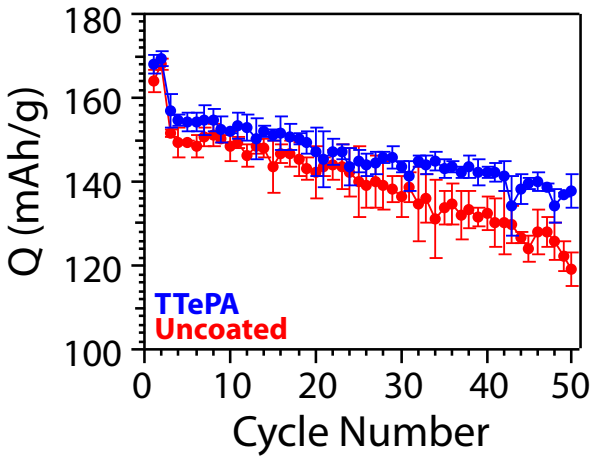

Figure 2.5. Charge–discharge cycle performance test results for uncoated NMC (•) and **TTePA**–coated NMC cathode materials (•), indicating that the electropolymerizable terthiophene surface coating results in enhanced discharge capacity retention. In triplicate, batteries were initially conditioned by charging and discharging at 0.1 C in the first two cycles, followed by 50 cycles of 0.3 C charging and 1 C discharging.

To confirm the presence of a polymerized **TTePA** coating after the half–cell cycling experiments, we performed *ex situ* XPS analysis of the cathode after 50 charge–discharge cycles. We opened one half–cell charged to a cell voltage of 3.6 V inside an argon–filled glovebox, and thoroughly washed the isolated cathode disc with dimethyl carbonate, and vacuum dried it prior to surface analysis. Note that this state of cathode charge will lead to oxidation of any surface bound polythiophenes (3.4 V oxidation potential), while leaving the parent terthiophene unperturbed due to its higher oxidation onset potential of 3.7 V (see Figure 2). XPS analysis of the cathode disc revealed that the presence of sulfur in the composite cathode, evidenced by the appearance of two distinct S (2p) peaks: one at 164 eV associated with the unreacted **TTePA** and a second peak at 170 eV (Figure 2.6). Given state of charge of the cathode, we assign the higher binding energy peak to oxidized polythiophene species. Quantitative analysis of the XPS

spectra reveals that the atom percent ratio [P]:[S] = 4:1, instead of the expected [P]:[S] = 1:3 expected for **TTePA**. The large difference in phosphorous content likely arises from the adsorption of $LiPF_6$ in the porous composite cathode. However, XPS firmly establishes the partial formation of a polymeric thiophene layer under the half–cell cycling conditions.

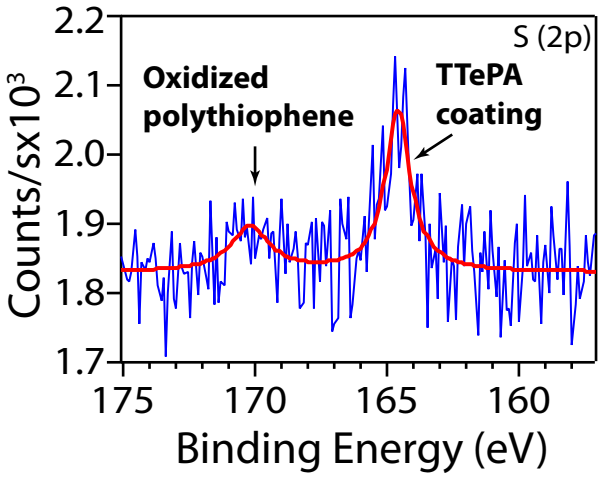

Figure 2.6. *Ex situ* XPS analysis of a cathode disc after half–cell cycle performance testing indicates the presence of two surface–bound S (2p) species with core electron binding energies of 164 eV and 170 eV, which correspond to the sulfurs in unreacted terthiophene headgroups and those in an oxidized (*p*–doped) surface–bound and electrically conductive polythiophene.

Attempts to discern the extent of oxidative polymerization of the surface–bound **TTePA** from the initial battery conditioning cycle charge–discharge curves failed, due to the very small charge transfer associated with this process. Based on the mass of NMC in the average cathode disc (~0.014 g), the relatively low NMC surface area (0.5 m^2/g), we calculate that the average CR2032 coin cell contains only $1.59 \bullet 10^{-8}$ mol **TTePA**. Complete xidative polymerization of the terthiophene functionality would thus would generate a nearly undetectable 1.5 mC of charge in the context of the expected specific cell capacity of ~177 mA•h/g or 8.92 C per cathode disc.

TTePA–coated NMC cathodes also exhibit improved rate performance as compared to the uncoated control cathode samples (Figure 2.7). After half–cell conditioning through two cycles of charging and discharging at 0.1 C, three half–cells were charged at 0.3 C and discharged at rates of 1, 2, 5, 8, and 10 C, followed a final 1 C discharge rate measurement. At discharge rates ≥ 2C, we observe statistically significant improvements in the **TTePA**–coated cathode specific discharge capacity. More explicitly, we observe a 20% improvement in discharge capacity at 5 C, and ≥ 250% improvement at 8 C and 10 C rates. In order to assess whether these extreme rate performance tests irreversibly damaged the cathode in some manner, we executed a final rate test at a discharge rate of 1 C. The fact that the specific capacity is of the **TTePA**–coated cathodes is comparable in the initial and final 1 C rate tests suggests that the improved performance stems from the polymeric surface coating. The superior rate performance of the NMC coated with a polythiophene molecular layer probably arises from the electrically conductive nature of the coating, since the conductive coating enhances the electrical contacts within the composite cathode. Previous reports suggest that conductive coatings on a cathode surface improve battery rate performance.[25, 52] Since polythiophene is electrically conductive upon oxidation or p–doping,[27, 53-54] the presence of oxidized polythiophene at the surface of the partially discharged cathode supports this proposed performance enhancement mechanism.

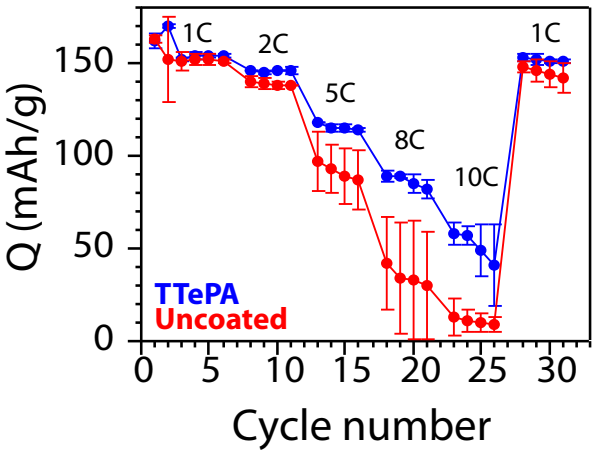

Figure 2.7. Rate performance tests of uncoated NMC (•) and TTePA–coated NMC (•) in lithium half–cells, demonstrating a significant discharge capacity improvement at high C rates for the coated NMC materials. In triplicate, half–cells were, initially conditioned by charging at 0.1 C and discharging at 0.1 C for the first two cycles, followed subsequent charging at 0.3 C and discharging at specified C rates in the presented order.

2.4 Conclusion

We have demonstrated the synthesis and solution grafting of the terthiophene alkylphosphonic acid **TTePA** surface ligand as a monolayer onto both model planar ITO glass substrates and high voltage NMC Li–ion battery cathode particles. Electrochemical characterization of **TTePA** molecular layers grafted onto model ITO glass substrates indicate that this coating undergoes oxidative electropolymerization at a potential of 3.7 V (v. Li/Li^+) to form a surface–bound polythiophene. Half–cell charge–discharge cycling performance tests of **TTePA**–coated NMC materials against Li metal in the voltage range 3.0–4.3 V indicate their superior capacity retention relative to uncoated NMC materials after 50 charge–discharge cycles. *Ex situ* XPS analyses reveal the formation of a polythiophene surface coating on the NMC cathodes, which protects the electrolyte from parasitic decomposition reactions at the cathode

particle surface and mitigates capacity fade. Rate performance tests further indicate that the **TTePA**–coated NMC exhibits enhanced rate performance at rates as high 5–10 C, relative to uncoated NMC cathode materials. This improved rate performance is ascribed to the electrically conductive nature of the polythiophene molecular layer on the NMC surfaces, which enhances the electrical connectivity between the current collector and the NMC cathode particles in the composite cathode

2.5 References

1. Tarascon, J. M.; Armand, M., Issues and challenges facing rechargeable lithium batteries. *Nature* **2001,** *414* (6861), 359-67.

2. Scrosati, B.; Garche, J., Lithium batteries: Status, prospects and future. *J. Power Sources* **2010,** *195* (9), 2419-2430.

3. Manthiram, A., Materials Challenges and Opportunities of Lithium Ion Batteries. *J. Phys. Chem. Lett.* **2011,** *2* (3), 176-184.

4. Kraytsberg, A.; Ein-Eli, Y., Higher, Stronger, Better...A Review of 5 Volt Cathode Materials for Advanced Lithium-Ion Batteries. *Adv. Energy Mater.* **2012,** *2* (8), 922-939.

5. Amine, K.; Kanno, R.; Tzeng, Y., Rechargeable lithium batteries and beyond: Progress, challenges, and future directions. *MRS Bull.* **2014,** *39* (05), 395-401.

6. Ohzuku, T.; Brodd, R. J., An overview of positive-electrode materials for advanced lithium-ion batteries. *J. Power Sources* **2007,** *174* (2), 449-456.

7. John, B. G., Evolution of Strategies for Modern Rechargeable Batteries. *Acc. Chem. Res.* **2013,** *46*, 1053.

8. Wu, Z.; Ji, S.; Zheng, J.; Hu, Z.; Xiao, S.; Wei, Y.; Zhuo, Z.; Lin, Y.; Yang, W.; Xu, K.; Amine, K.; Pan, F., Prelithiation Activates $Li(Ni_{0.5}Mn_{0.3}Co_{0.2})O_2$ for High Capacity and Excellent Cycling Stability. *Nano Lett.* **2015,** *15* (8), 5590-6.

9. Li, Y.; Meyer, S.; Lim, J.; Lee, S. C.; Gent, W. E.; Marchesini, S.; Krishnan, H.; Tyliszczak, T.; Shapiro, D.; Kilcoyne, A. L.; Chueh, W. C., Effects of Particle Size, Electronic Connectivity, and Incoherent Nanoscale Domains on the Sequence of Lithiation in $LiFePO_4$ Porous Electrodes. *Adv. Mater.* **2015,** *27* (42), 6591-7.

10. Wu, M.; Xiao, X.; Vukmirovic, N.; Xun, S.; Das, P. K.; Song, X.; Olalde-Velasco, P.; Wang, D.; Weber, A. Z.; Wang, L. W.; Battaglia, V. S.; Yang, W.; Liu, G., Toward an ideal polymer binder design for high-capacity battery anodes. *J. Amer. Chem. Soc.* **2013,** *135* (32), 12048-56.

11. Zhao, H.; Fu, Y.; Ling, M.; Jia, Z.; Song, X.; Chen, Z.; Lu, J.; Amine, K.; Liu, G., Conductive Polymer Binder-Enabled SiO-SnxCoyCz Anode for High-Energy Lithium-Ion Batteries. *ACS. Appl. Mater. Interfaces* **2016,** *8* (21), 13373-7.

12. Liu, G.; Xun, S. D.; Vukmirovic, N.; Song, X. Y.; Olalde-Velasco, P.; Zheng, H. H.; Battaglia, V. S.; Wang, L. W.; Yang, W. L., Polymers with Tailored Electronic Structure for High Capacity Lithium Battery Electrodes. *Adv. Mater.* **2011,** *23* (40), 4679-4683.

13. Patel, S. N.; Javier, A. E.; Balsara, N. P., Electrochemically oxidized electronic and ionic conducting nanostructured block copolymers for lithium battery electrodes. *ACS Nano* **2013,** *7* (7), 6056-68.

14. Choi, N.-S.; Han, J.-G.; Ha, S.-Y.; Park, I.; Back, C.-K., Recent advances in the electrolytes for interfacial stability of high-voltage cathodes in lithium-ion batteries. *RSC Advances* **2015,** *5* (4), 2732-2748.

15. Hausbrand, R.; Cherkashinin, G.; Ehrenberg, H.; Gröting, M.; Albe, K.; Hess, C.; Jaegermann, W., Fundamental degradation mechanisms of layered oxide Li-ion battery cathode materials: Methodology, insights and novel approaches. *Mater. Sci. Eng. B* **2015,** *192*, 3-25.

16. Yoshida, T.; Takahashi, M.; Morikawa, S.; Ihara, C.; Katsukawa, H.; Shiratsuchi, T.; Yamaki, J.-i., Degradation Mechanism and Life Prediction of Lithium-Ion Batteries. *J. Electrochem. Soc.* **2006,** *153* (3), A576.

17. Goodenough, J. B.; Kim, Y., Challenges for Rechargeable Li Batteries†. *Chem. Mater.* **2010,** *22* (3), 587-603.

18. Xu, K.; von Cresce, A., Interfacing electrolytes with electrodes in Li ion batteries. *J. Mater. Chem.* **2011,** *21* (27), 9849.

19. Jackson, D. H. K.; Laskar, M. R.; Fang, S. Y.; Xu, S. Z.; Ellis, R. G.; Li, X. Q.; Dreibelbis, M.; Babcock, S. E.; Mahanthappa, M. K.; Morgan, D.; Hamers, R. J.; Kuech, T. F., Optimizing AlF_3 atomic layer deposition using trimethylaluminum and TaF_5: Application to high voltage Li-ion battery cathodes. *J. Vac. Sci. Technol. A* **2016,** *34* (3).

20. Laskar, M. R.; Jackson, D. H. K.; Guan, Y. X.; Xu, S. Z.; Fang, S. Y.; Dreibelbis, M.; Mahanthappa, M. K.; Morgan, D.; Hamers, R. J.; Kuech, T. F., Atomic Layer Deposition of Al_2O_3-Ga_2O3 Alloy Coatings for $LiNi_{0.5}Mn_{0.3}Co_{0.2}O_2$ Cathode to Improve Rate Performance in Li-ion Battery. *ACS. Appl. Mater. Interfaces* **2016,** *8* (16), 10572-10580.

21. Meng, X. B.; Yang, X. Q.; Sun, X. L., Emerging Applications of Atomic Layer Deposition for Lithium-Ion Battery Studies. *Adv. Mater.* **2012,** *24* (27), 3589-3615.

22. Fu, L. J.; Liu, H.; Li, C.; Wu, Y. P.; Rahm, E.; Holze, R.; Wu, H. Q., Surface modifications of electrode materials for lithium ion batteries. *Solid State Sci.* **2006,** *8* (2), 113-128.

23. Bloom, I.; Trahey, L.; Abouimrane, A.; Belharouak, I.; Zhang, X.; Wu, Q.; Lu, W.; Abraham, D. P.; Bettge, M.; Elam, J. W.; Meng, X.; Burrell, A. K.; Ban, C.; Tenent, R.; Nanda, J.; Dudney, N., Effect of interface modifications on voltage fade in $0.5Li_2MnO_3{\cdot}0.5LiNi_{0.375}Mn_{0.375}Co_{0.2}5O_2$ cathode materials. *J. Power Sources* **2014,** *249*, 509-514.

24. Li, X.; Liu, J.; Meng, X.; Tang, Y.; Banis, M. N.; Yang, J.; Hu, Y.; Li, R.; Cai, M.; Sun, X., Significant impact on cathode performance of lithium-ion batteries by precisely controlled metal oxide nanocoatings via atomic layer deposition. *J. Power Sources* **2014,** *247*, 57-69.

25. Li, H.; Zhou, H., Enhancing the performances of Li-ion batteries by carbon-coating: present and future. *Chem. Commun.* **2012,** *48* (9), 1201-17.

26. Cho, Y.-D.; Fey, G. T.-K.; Kao, H.-M., The effect of carbon coating thickness on the capacity of $LiFePO_4$/C composite cathodes. *J. Power Sources* **2009,** *189* (1), 256-262.

27. Abouimrane, A.; Odom, S. A.; Tavassol, H.; Schulmerich, M. V.; Wu, H.; Bhargava, R.; Gewirth, A. A.; Moore, J. S.; Amine, K., 3-Hexylthiophene as a Stabilizing Additive for High Voltage Cathodes in Lithium-Ion Batteries. *J. Electrochem. Soc.* **2012,** *160* (2), A268-A271.

28. Choi, J. A.; Eo, S. M.; MacFarlane, D. R.; Forsyth, M.; Cha, E.; Kim, D. W., Effect of organic additives on the cycling performances of lithium metal polymer cells. *J. Power Sources* **2008,** *178* (2), 832-836.

29. Xia, L.; Xia, Y. G.; Liu, Z. P., Thiophene derivatives as novel functional additives for high-voltage LiCoO2 operations in lithium ion batteries. *Electrochim. Acta* **2015,** *151*, 429-436.

30. Xing, L. Y.; Hu, M.; Tang, Q.; Wei, J. P.; Qin, X.; Zhou, Z., Improved cyclic performances of $LiCoPO_4$/C cathode materials for high-cell-potential lithium-ion batteries with thiophene as an electrolyte additive. *Electrochim. Acta* **2012,** *59*, 172-178.

31. Choi, J.; Ruiz, C. R.; Nesterov, E. E., Temperature-Induced Control of Conformation and Conjugation Length in Water-Soluble Fluorescent Polythiophenes. *Macromolecules* **2010,** *43* (4), 1964-1974.

32. Wagner, K.; Byrne, R.; Zanoni, M.; Gambhir, S.; Dennany, L.; Breukers, R.; Higgins, M.; Wagner, P.; Diamond, D.; Wallace, G. G.; Officer, D. L., A multiswitchable poly(terthiophene) bearing a spiropyran functionality: understanding photo- and electrochemical control. *J. Amer. Chem. Soc.* **2011,** *133* (14), 5453-62.

33. Umeda, R.; Awaji, H.; Nakahodo, T.; Fujihara, H., Nanotube composites consisting of metal nanoparticles and polythiophene from electropolymerization of terthiophene-functionalized metal (Au, Pd) nanoparticles. *J. Amer. Chem. Soc.* **2008,** *130* (11), 3240-1.

34. Hotchkiss, P. J.; Jones, S. C.; Paniagua, S. A.; Sharma, A.; Kippelen, B.; Armstrong, N. R.; Marder, S. R., The modification of indium tin oxide with phosphonic acids: mechanism of binding, tuning of surface properties, and potential for use in organic electronic applications. *Acc. Chem. Res.* **2012,** *45* (3), 337-46.

35. Cynthia, G. Z., *Handbook of electrochemistry*. First edition; Elsevier: Amsterdam, 2007, pp146.

36. Jadhav, S. A., Self-assembled monolayers (SAMs) of carboxylic acids: an overview. *Cent. Eur. J. Chem.* **2011,** *9* (3), 369-378.

37. Harrison, K. E.; Kang, J. F.; Haasch, R. T.; Kilbey, S. M., Surface structure and composition of thiophene-bearing monolayers. *Langmuir* **2001,** *17* (21), 6560-6568.

38. Kang, J. F.; Perry, J. D.; Tian, P.; Kilbey, S. M., Growth and morphology of polythiophene on thiophene-capped monolayers: 1. Single component monolayers. *Langmuir* **2002,** *18* (26), 10196-10201.

39. Paniagua, S. A.; Giordano, A. J.; Smith, O. L.; Barlow, S.; Li, H.; Armstrong, N. R.; Pemberton, J. E.; Bredas, J. L.; Ginger, D.; Marder, S. R., Phosphonic Acids for Interfacial Engineering of Transparent Conductive Oxides. *Chem. Rev.* **2016,** *116* (12), 7117-58.

40. Queffelec, C.; Petit, M.; Janvier, P.; Knight, D. A.; Bujoli, B., Surface modification using phosphonic acids and esters. *Chem. Rev.* **2012,** *112* (7), 3777-807.

41. Mutin, P. H.; Guerrero, G.; Vioux, A., Hybrid materials from organophosphorus coupling molecules. *J. Mater. Chem.* **2005,** *15* (35-36), 3761-3768.

42. Hanson, E. L.; Schwartz, J.; Nickel, B.; Koch, N.; Danisman, M. F., Bonding self-assembled, compact organophosphonate monolayers to the native oxide surface of silicon. *J. Amer. Chem. Soc.* **2003,** *125* (51), 16074-80.

43. Hanson, E. L.; Guo, J.; Koch, N.; Schwartz, J.; Bernasek, S. L., Advanced surface modification of indium tin oxide for improved charge injection in organic devices. *J. Amer. Chem. Soc.* **2005,** *127* (28), 10058-62.

44. Diaz, A. F.; Crowley, J.; Bargon, J.; Gardini, G. P.; Torrance, J. B., ELECTROOXIDATION OF AROMATIC OLIGOMERS AND CONDUCTING POLYMERS. *J. Electroanal. Chem.* **1981,** *121* (APR), 355-361.

45. Koh, S. E.; McDonald, K. D.; Holt, D. H.; Dulcey, C. S.; Chaney, J. A.; Pehrsson, P. E., Phenylphosphonic acid functionalization of indium tin oxide: surface chemistry and work functions. *Langmuir* **2006,** *22* (14), 6249-55.

46. Dannetun, P.; Boman, M.; Stafström, S.; Salaneck, W. R.; Lazzaroni, R.; Fredriksson, C.; Bredas, J. L.; Zamboni, R.; Taliani, C., The chemical and electronic structure of the interface between aluminum and polythiophene semiconductors. *J. Chem. Phys.* **1993,** *99* (1), 664.

47. English, C. R.; Bishop, L. M.; Chen, J.; Hamers, R. J., Formation of self-assembled monolayers of pi-conjugated molecules on TiO_2 surfaces by thermal grafting of aryl and benzyl halides. *Langmuir* **2012,** *28* (17), 6866-76.

48. Gao, W.; Dickinson, L.; Grozinger, C.; Morin, F. G.; Reven, L., Self-assembled monolayers of alkylphosphonic acids on metal oxides. *Langmuir* **1996,** *12* (26), 6429-6435.

49. Hanwell, M. D.; Curtis, D. E.; Lonie, D. C.; Vandermeersch, T.; Zurek, E.; Hutchison, G. R., Avogadro: an advanced semantic chemical editor, visualization, and analysis platform. *J. Cheminformatics* **2012,** *4* (1), 17.

50. Woodford, W. H.; Carter, W. C.; Chiang, Y.-M., Design criteria for electrochemical shock resistant battery electrodes. *Energy Environ. Sci.* **2012,** *5* (7), 8014.

51. Zhu, M.; Park, J.; Sastry, A. M., Fracture Analysis of the Cathode in Li-Ion Batteries: A Simulation Study. *J. Electrochem. Soc.* **2012,** *159* (4), A492.

52. Lee, S.; Cho, Y.; Song, H.-K.; Lee, K. T.; Cho, J., Carbon-Coated Single-Crystal LiMn2O4 Nanoparticle Clusters as Cathode Material for High-Energy and High-Power Lithium-Ion Batteries. *Angewa. Chem. Int. Ed.* **2012,** *51* (35), 8748-8752.

53. J. Roncali, R. G., A. Yassar, P. Marque, F. Gamier, M. Lemaire, Effects of Steric Factors on the Electrosynthesis and Properties of Conducting Poly(3-alkyithiophenes). *J. Phys. Chem.* **1987,** *91*, 6706-6714.

54. Roncali, J., Conjugated Poly(Thiophenes)-Synthesis, Functionalizations, And Applications. *Chem. Rev.* **1992,** *92* (4), 711-738.

CHAPTER 3

EFFECTS OF ALKYL PHOSPHONATE SURFACE COATINGS ON HIGH-VOLTAGE $LiNi_{0.5}Mn_{0.3}Co_{0.2}O_2$ CATHODE PERFORMANCE

3.1 INTRODUCTION

Lithium–ion batteries (LIBs) are one of the most widely used power sources in portable electronics, due to their high energy densities that arise from the small atomic mass and the low standard reduction potential of lithium metal. In spite of their ubiquity in consumer electronic applications, LIBs have not achieved widespread applications in electric vehicles and large-scale devices for the electrical grid storage of intermittent forms of renewable energy (e.g., wind or solar energy) due to their limited deliverable power and modest storage capacities. Since electrical power is proportional to both the maximum current and the electrochemical potential difference across the battery electrodes, two routes for enhancing the deliverable power of LIBs have emerged: (1) increasing the total battery capacity using high capacity anodes such as lithiated silicon and lithiated germanium,[1-3] and (2) increasing the electrochemical potential difference between the LIB anode and cathode by harnessing the high-voltage cathode materials.[1, 4]

The development and implementation of high-voltage cathode materials has focused primarily on layered inorganic metal oxides into which lithium ions may intercalate under an electrochemical driving force. $LiCoO_2$ is a quintessential layered structured that has been widely used as a LIB cathode operable at voltages ≤ 3.6, V with a specific capacity that is only half of

its theoretical capacity.[4] The limited practical capacity and the restricted operating voltage range stem from the fact that this structure is susceptible to electrochemically-induced structural changes, including irreversible decomposition by oxygen evolution. Exchanging the cobalt sites to varying extents with Earth-abundant transition metals such as nickel and manganese leads to the formation of a variety of $LiNi_xMn_yCo_zO_2$ (NMC) layered cathode materials,[2, 4-9] wherein the useful intercalation voltage range sensitively depends on the metal stoichiometry. However, the long-term cycling performance of these high voltage cathode materials in LIBs is compromised due to a complex combination of decomposition processes that occur in the presence of typical $LiPF_6$/organic carbonate battery electrolytes.[5, 7-8, 10-14] Specifically, manganese ion dissolution and subsequent solution reactions with $LiPF_6$ can lead to the formation of high impedance solid-electrolyte interphase (SEI) layers at both the cathode and anode surfaces. Furthermore, the highly oxidizing electrochemical potentials at which these NMC cathodes operate also trigger the decomposition of electrolyte components such as $LiPF_6$ and the organic carbonate solvent to yield resistive SEI layers at the cathode. These irreversible chemical reactions consume lithium, which leads to permanent capacity losses during every battery charge-discharge cycle.

Numerous research groups have investigated the use of inorganic cathode surface coatings as a means of mitigating transition metal dissolution and oxidative electrolyte degradation reactions.[15-19] Some commonly studied coatings are inorganic, electrical insulators such as Al_2O_3,[16, 18] ZrO_2,[17, 20] $AlPO_4$,[21-22] MgO and AlF_3[19, 23] produced by either sol-gel synthesis or atomic layer deposition (ALD) in order to produce coatings of controlled thicknesses ~2-100 nm. These coatings enhance the cycling performance of the LIBs by a combination of mechanisms, including prevention of transition metal dissolution from the cathode, scavenging HF produced from hydrolysis of $LiPF_6$ by adventitious water, and preventing unwanted

electrolyte oxidation by physically blocking direct contact between the electrolyte and active materials. However, this strategy requires careful control over the coating thickness.[19] Thick, electrically insulating surface coatings reduce the efficiency of electron transfer to and from the active cathode material, which is required to drive lithium ion intercalation and deintercalation. Thick coatings also reduce the rate of lithium (de)intercalation by forming a physical barrier at the electrode/electrolyte interface. On the other hand, very thin coatings typically do not provide enough surface protection to prevent unwanted electrolyte degradation at the cathode particle surface. While precise coating thickness control is difficult to achieve using sol-gel coating methods,[24] atomic layer deposition (ALD) techniques enable production of such materials at significant costs associated with the detailed optimization of materials processing protocols. [25]

An alternative strategy for producing cathode materials with thin coatings of precisely controlled thicknesses is to use solution-grafted self-assembled monolayers of high purity organic molecules. Alkyl phosphonic acids are known to form stable, covalently bound self-assembled monolayers on metal oxide surfaces through strong and hydrolytically stable metal-phosphonate bonds.[26-29] Thus, we reasoned that grafting a series of homologous alkyl phosphonic acids ($C_nH_{2n+1}PO_3H_2$) of variable chain lengths (n = 2, 6, 10, 14, and 18) to the surface of NMC cathode particles would produce electrically insulating, organic coatings with well-defined thicknesses. By comparatively evaluating the electrochemical performance of these materials in Li-ion half–cells against the uncoated materials, we identify the optimal coating thickness required to optimize battery cycling performance while mitigating irreversible capacity losses due to contact between the electrolyte and the NMC particle surface.

3.2 Experimental Section

Materials. All materials and reagent grade solvents were purchased from Sigma–Aldrich Chemical Co. (Milwaukee, WI) and used as received unless otherwise noted. $LiNi_{0.5}Mn_{0.3}Co_{0.2}O_2$ (NMC) electrode powder and electrolyte (1M $LiPF_6$ in 50:50 *v/v* mixture of ethyl carbonate:diethyl carbonate) were supplied by The Dow Chemical Company (Midland, MI) and storage in an argon glovebox. CR2032 coin cell components (case, cap and gasket) were purchased from Pred Materials International, Inc. TIMCAL Super C 65 carbon black and SOLVAY Solef 5130 poly(vinylidene difluoride) (PVDF) were used as received. Celgard 2500 separators were cut into 1.9 cm diameter discs and dried at 40 °C under vacuum for 12 h. Dried separators were then immersed in an electrolyte mixture within an argon-filled glovebox for at least 12 h prior to lithium half-cell assembly.

^{1}H NMR spectra were recorded in DMSO–d_6 using Bruker AC+ 300a, Bruker Avance 400 spectrometers and Bruker Avance 500 spectrometers. Spectra were referenced to the residual protiated solvent peaks in the samples. Analytical purity of all alkyl phosphonic acids was established prior to use by elemental analyses (C,H), which were performed by Atlantic Microlab, Inc. (Norcross, GA) prior to use.

Ethylphosphonic acid (EPA). EPA (200 mg, 1.81 mmol) was recrystallized from CH_3CN (5 mL) to obtain an analytically pure sample. ^{1}H NMR (500 MHz, DMSO–d_6) δ (ppm): 1.48 (*dq*, *J* = 17.5, 7.7 Hz, 2H), 1.01 (*dt*, *J* = 18.9, 7.6 Hz, 3H). *Anal*. Calc $C_2H_7O_3P$; C, 21.83; H, 6.43; Found C, 21.76; H, 6.24.

Hexylphosphonic acid (HPA). HPA (200 mg, 1.2 mmol) was triturated with CH_3CN (7 mL) and isolated by centrifugation. Repetition of this process twice more yielded a pure sample that was free of any residual EPA impurities. ^{1}H NMR (400 MHz, DMSO–d_6) δ (ppm): 1.66–

1.20 (*m*, 10H), 0.94 (*t*, *J* = 6.8 Hz, 3H). *Anal*. Calc $C_6H_{15}O_3P$; C, 43.37; H, 9.10; Found C, 43.66; H, 9.16.

Decylphosphonic acid (DPA). DPA was purified per the protocol used for HPA. ^{1}H NMR (300 MHz, DMSO–d_6) δ (ppm): 1.34 (*m*, *J* = 61.8 Hz, 18H), 0.92 – 0.77 (*t*, *J* = 6.8 Hz, 3H). *Anal*. Calc $C_{10}H_{23}O_3P$; C, 54.04; H, 10.43; Found C, 53.83; H, 10.30.

Tetradecylphosphonic acid (TDPA). TDPA was purified per the protocol used for HPA. ^{1}H NMR (500 MHz, DMSO–d_6) δ (ppm): 1.59 – 1.14 (*m*, 26H), 0.86 (*t*, *J* = 6.8 Hz, 3H). *Anal*. Calc $C_{14}H_{31}O_3P$; C, 60.41; H, 11.23; Found C, 60.45; H, 11.39.

Octadecylphosphonic acid (ODPA). ODPA was purified per the protocol used for HPA. ^{1}H NMR (500 MHz, DMSO–d_6) δ (ppm): 1.52 – 1.18 (*m*, 34H), 0.86 (*t*, *J* = 6.7 Hz, 3H). *Anal*. Calc $C_{18}H_{39}O_3P$; C, 64.64; H, 11.75; Found C, 64.65; H, 11.86.

Representative Procedure for Alkyl Phosphonic Acid Grafting to NMC. Organic surface contamination was removed from the surface of $LiNi_{0.5}Mn0_{.3}Co_{0.2}O_2$ (NMC, 2 g) powder using a UV-ozone cleaner equipped with both 189.4 nm and 253.7 nm sources (Uvotech ProCleanerTM 110). Cleaned NMC powder was then immersed in a solution of alkyl phosphonic acid (~3–5 mg) in anhydrous ethanol (10 mL). The amount of phosphonic acid reflected a three-fold excess of the amount required to fully coat the NMC with a single monolayer, as calculated from the NMC surface area (0.5 m^2/g by BET analysis at The Dow Chemical Company) and the expected area covered by a metal-bound phosphonate (0.24 nm^2/molecule).[26] The ethanolic slurry of NMC particles was stirred for 5 min at ambient temperature, after which the NMC was isolated by centrifugation and decanting the supernatant liquid. The powder isolated from this procedure was heated to 140 °C under vacuum for 48 h to drive the formation of alkyl phosphonate-metal bonds by dehydration. After heat treatment, alkyl phosphonate-coated NMC

was thoroughly washed anhydrous ethanol (3 x 10 mL) at ambient temperature in order to remove any excess, ungrafted acid. The NMC was dried under vacuum prior to materials characterization and half-cell assembly.

X–ray Photoelectron Spectroscopy (XPS). XPS spectra of alkyl phosphonate–coated NMC powders were measured using a Thermo Fisher K–Alpha™ X-ray Photoelectron Spectrometer by exposure to a monochromatic micro-focused Al *K*α X–rays (1486.6 eV) with 400 μm spot size, analyzer resolution of 0.1 eV, a pass energy of 50.0 eV, and a take–off angle of 90°. Peak positions and peak area ratios for P (2p) and Co (2p) were calculated by baseline correction using the Smart function in the Avantage software, fitting the observed peaks to a combined 30% Gaussian and 70% Lorentzian function, and normalization of the signals using the atomic sensitivity factors (P (2*p*) = 1.353; Co (2*p*) = 18.235).

Diffuse Reflectance Infrared Fourier Transform Infrared Spectroscopy (DRIFTS). A Bruker Vertex 70 Fourier transform infrared (FTIR) spectrometer equipped with a Harrick Praying Mantis DRIFTS Accessory and a liquid nitrogen–cooled HgCdTe detector was used to collect DRIFTS spectra of alkyl phosphonate–grafted NMC. The sample holder was purged with dry air to minimize spectral signals associated with water vapor. Spectra were collected on physical mixtures of NMC powders with anhydrous KBr powder by averaging 500 scans over the energy range 4000 to 500 cm^{-1} with resolution of 4 cm^{-1}. All spectra were background corrected using a spectrum of the pure KBr powder from 2400 cm^{-1} to 3600 cm^{-1}, and then each spectrum was baseline corrected using a second–order polynomial fit.

Cathode Disc Fabrication. Super C 65 carbon black (0.00978 g), a 8.2 wt% solution of PVDF in *N*-methyl pyrrolidone (0.9278 g), and NMP (0.4 mL) were mixed using a planetary centrifugal mixer (Thinky Mixer ARE–310) at 2000 rpm for 4 min followed by 2200 rpm for 30

sec. Additional NMP (0.4 mL) was added to the slurry and it was mixed again according to the same protocol. Alkyl phosphonate–grafted NMC powder (2 g) was then added to the slurry, and it was again mixed by the same procedure. The resulting slurry was subsequently cast onto 15 μm thick Al foil (MTI corporation, Richmond, CA) using an Elcometer 4340 Automatic Film Applicator and dried under high vacuum at 40 °C for 16 h. The resulting solvent–cast cathode sheet was cut into 15 mm diameter discs, each of which were calendared under 1.8 tons force for 8 min in a Carver 3851–0 melt press at ambient temperature. Inside an argon-filled glovebox, the pressed discs were heated to 140 °C under vacuum for 12 h to effect their thorough drying.

Half-Cell Assembly and Testing. A CR2032 lithium half–cell was assembled inside an argon–filled glovebox as follows. Each cathode disc was weighed prior to coin cell assembly, in order to accurately calculate the expected specific capacity for the associated cell. Lithium foil (0.2 mm thick, Rockwood Lithium, Kings Mountain, NC) was cut into 16 mm diameter electrode discs. The CR2032 cell cap was loaded with a 16 mm diameter stainless steel spacer, on top of which a lithium foil electrode disc was centered. 40 μl of electrolyte (1M $LiPF_6$ in 50:50 *v/v* mixture of ethyl carbonate:diethyl carbonate) was placed on top of the lithium electrode. An Celgard separator pre-soaked in the electrolyte was placed on top of the lithium electrode, followed by a plastic gasket and another 40 μl of electrolyte. The cathode disc, which curled slightly during vacuum drying, was flattened using plastic tweezers prior to its placement on top of the separator. A stainless steel spacer was stacked on top of the cathode disc, followed by a stainless steel metal spring and the bottom cap. The cell was then crimped sealed using Hohsen automatic coin cell crimper (Osaka, Japan).

Half–cells were cycled between 3.0–4.3 V vs. Li/Li^+, using an Arbin BT2000 battery test station. For discharge capacity retention measurements, cells were initially conditioned by

charging and discharging at 0.1 C for the first two cycles. In subsequent cycles, cells were charged at 0.3 C and discharged at 1 C. For the rate performance tests, all half-cells were conditioned by charging and discharging at 0.1 C for the first two cycles, after which subsequent cycles used a 0.3 C charge rate and increasing discharge C rates (1, 2, 5, 8, 10), followed a final 1 C rate test.

Electrochemical Impedance Spectroscopy (EIS). Electrochemical Impedance Spectroscopy was performed using Biologic SP–200 potentiostat. 51 data points were measured over a frequency range 0.1 Hz –10^5 Hz using an applied potential 10 mV versus the open circuit voltage (OCV) of the half-cell (~3.0 V). Triplicate EIS measurements were made for each coin cell before and after performing the aforementioned rate tests, with a 5 min resting interval between each measurement to enable equilibration of any electrochemical potential gradients.

3.3 Results and Discussion

Numerous reports have described the adsorption of phosphonic acids into metal oxide surfaces (e.g., TiO_2,[30-31] ITO,[32-33] ZrO2,[34-35] stainless steel[36]) and their subsequent heat treatment to yield strongly bound, protective surface monolayers.[37-39] We adapted previously reported protocols for alkyl phosphonate monolayer formation on metal oxides to our NMC materials. We initially cleaned our NMC powder samples using a UV-ozone cleaner to remove any organic contaminants from the surface and to maximize the surface hydroxyl content. Alkyl phosphonic acids $C_nH_{2n+1}PO_3H_2$ (n = 2, 6, 10, 14, and 18) were then adsorbed onto the surfaces of NMC powders from an ethanol solution. The resulting particles were subsequently heat treated to drive condensation of the phosphonic acids with the metal oxide surface hydroxyl groups to form covalently bound surface layers.

We assessed the surface coverage of these molecular coatings using X-ray photoelectron spectroscopy (XPS), by measuring the phosphorous and cobalt atom percent ratio [P]:[Co]. XPS reveals that [P]:[Co] = 1.2–1.5 for the n = 2, 10, 14, and 18 alkylphosphonate-grafted NMC samples, suggesting a relatively constant grafting density. However, the grafting density for the HPA (n = 6) coated NMC was apparently much lower as [P]:[Co] = 0.8. The latter result led us to consider the possibility that the apparently lower surface coverage of the HPA arose from an organic monolayer, whereas the higher coverage for the other alkyl phosphonate ligands may have potentially originated from multilayer formation. We tested this hypothesis by stirring the EPA-grafted NMC in a 5 wt% Et_3N solution in ethanol, followed by particle isolation by centrifugation and vacuum drying. A similar protocol was previously reported to break up of any multilayers that might have formed.[39] XPS analysis of the Et_3N–washed NMC powders yielded no significant difference in the observed [P]:[Co]. Thus, the alkyl phosphonate coatings are apparently monolayers with nearly equal surface ligand densities, with the exception of the HPA that apparently forms a significantly less dense surface layer.

The surface grafting density (n_F) may be estimated as:

$$n_F = \frac{l_P}{l_{Co}} \rho_{Co} \lambda_{Co} cos\,\theta = \frac{[P]}{[Co]} \rho_{Co} \lambda_{Co} cos\,\theta$$

where l_P and l_{Co} are the atom percent values for P (2p) and Co (2p) measured by XPS, ρ_{Co} = 5.9 molecules/nm^3 is the atomic number density of Co in NMC unit cell, λ_{Co} = 1.287 nm is the inelastic mean free path of Co, and $\theta = 90°$ is the XPS instrument take–off angle.[40] Note that the ratio (l_P/l_{Co}) = [P]/[Co], the values of which are listed in Table 3.1. Thus, [P]:[Co] = 1.3 corresponds to an estimated surface coverage of 9.9 molecules/nm^2 Compact, self-assembled monolayers of alkyl phosphonates grafted to planar substrates typically exhibit a surface

coverage of ~4 molecules/nm^2.[26] The factor of two discrepancy between these previous reports and our analyses likely stems from the curvature and the roughness of the NMC particle surfaces, which introduces uncertainties into the above analysis that assumes a relatively flat substrate. Furthermore, our calculation utilizes the inelastic mean free path of pure metallic Co,[46] since the value for cobalt in NMC is not known.

Table 3.1. Phosphorous-to-Cobalt Atomic Ratio for Alkyl Phosphonate–coated NMC Particles.

Coating Type	[P]:[Co]
EPA	1.5
HPA	0.8
DPA	1.2
TDPA	1.3
ODPA	1.5

Previous reports have demonstrated that the grafting of alkyl phosphonate monolayers onto planar substrates is a cooperative process, in which monolayer crystallinity directs further surface ligand adsorption to yield a densely packed surface layer.[41-42] These reports interrogated the crystallinities of the resulting monolayers using Fourier transform infrared (FTIR) spectroscopies, including polarization-modulated infrared reflection–absorption spectroscopy (PM-IRRAS) and diffuse reflectance infrared Fourier transform spectroscopy (DRIFTS). These well-established and reliable FTIR methods enable quantitation of the crystallinity of self-assembled alkane monolayers, since the ratio of the C-H symmetric and asymmetric stretching band intensities for the methylene (–CH_2–) units in the alkyl chains is a sensitive indicator of the restricted molecular motions associated with alkyl chain crystallization.

Stimulated by these reports, we assessed the crystallinities of the alkyl phosphonate monolayers on the NMC surface as a function of the chain length using DRIFTS (Figure 3.1).

We observed four different DRIFTS spectral bands of varying intensities in the frequency range 2800–3000 cm^{-1}, which correspond to the symmetric and asymmetric C-H stretching modes of both the terminal methyl group (2870 and 2960 cm^{-1}) and the methylene units (2850 and 2920 cm^{-1}) in the alkyl chains. The symmetric C-H stretch near 2920 cm^{-1} splits into a lower energy mode at 2918 cm^{-1} corresponding to a methylene unit in a crystalline environment, and a higher energy mode at 2933 cm^{-1} associated with an methylene unit in an amorphous environment.[41,43] We observed that the relative absorbance of the crystalline CH_2 mode qualitatively increases with increasing chain length, implying increasing monolayer crystallinity. The EPA-grafted sample exhibits only a single band associated with a purely amorphous monolayer. Note that the amorphous band in the HPA-grafted samples is more intense than the crystalline one, whereas the crystalline spectral band is more intense than the amorphous one when n ≥ 10. The last observation implies that the degree of crystallinity of the HPA molecular layer is lower than that of the n ≥ 10 samples, which qualitatively exhibit higher crystallinities.

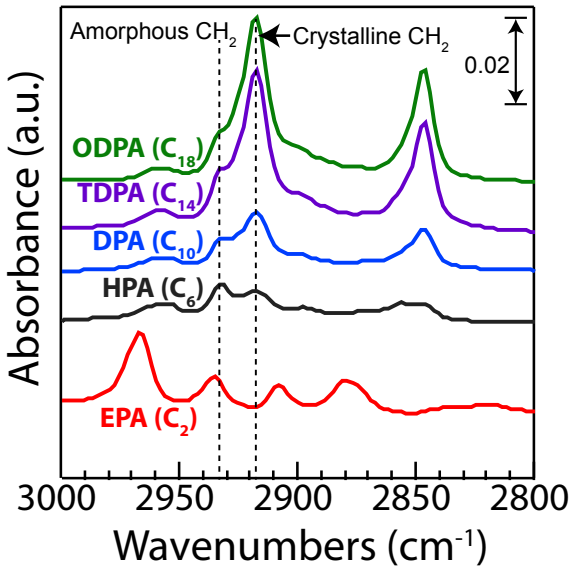

Figure 3.1. DRIFTS spectra for alkylphosphonate molecular layers grafted on NMC cathode particles. The relative intensities of the spectral bands at 2918 cm^{-1} and 2933

cm^{-1}, which correspond to the crystalline and amorphous symmetric C-H stretches of the alkyl chain methylene units, enable quantitation of the surface layer crystallinity.

From the relative absorbances of these crystalline and amorphous methylene DRIFTS bands in a given spectrum (A_{2918} and A_{2933}, respectively), we quantitatively calculated the percent crystallinity (χ) of the alkyl phosphonate monolayer as $\chi = A_{2918}/(A_{2918} + A_{2933})$. The χ values extracted from our analyses are given in Table 3.2 and plotted in Figure 3.2a. χ increases with increasing chain length to an asymptotic value of ~80 %. Figure 3.2b depicts a plot of χ versus [P]:[Co], whereby the latter quantity is related to the surface coverage. From this plot, we deduce a nearly linear relationship between the monolayer crystallinity and the surface grafting density for chains with $n \geq 6$. This observation is consistent with the previous reports that the alkyl phosphonate grafting occurs cooperatively, such that higher crystallinity in the molecular layer leads to better packing that pre-organizes the phosphonate ligands to graft with high densities to the underlying surface.[41] We speculate that the intermediate chain length HPA ligands graft to the surface and occlude the adjacent surface grafting sites due to the lower crystallinity of the monolayer, and thus the surface is incompletely coated. On the other hand, the short ethyl chains of EPA are sufficiently small that they do not sterically interfere with the grafting process. Thus, high surface coverages are obtained for EPA.

Table 3.2. Relative crystallinity and % crystallinity of each phosphonate coating on the NMC.

Coating Type	Relative crystallinity[a]	% crystallinity (χ)[b]
EPA	0.00	0.0
HPA	0.82	45
DPA	1.8	64
TDPA	2.6	72
ODPA	13	76

[a] Relative crystallinity = A_{2918}/A_{2933}, where A2918 and A2933 are the absorbances

measured by DRIFTS at 2918 and 2933 cm^{-1}. [b] $\chi = A_{2918}/(A_{2918} + A_{2933})$.

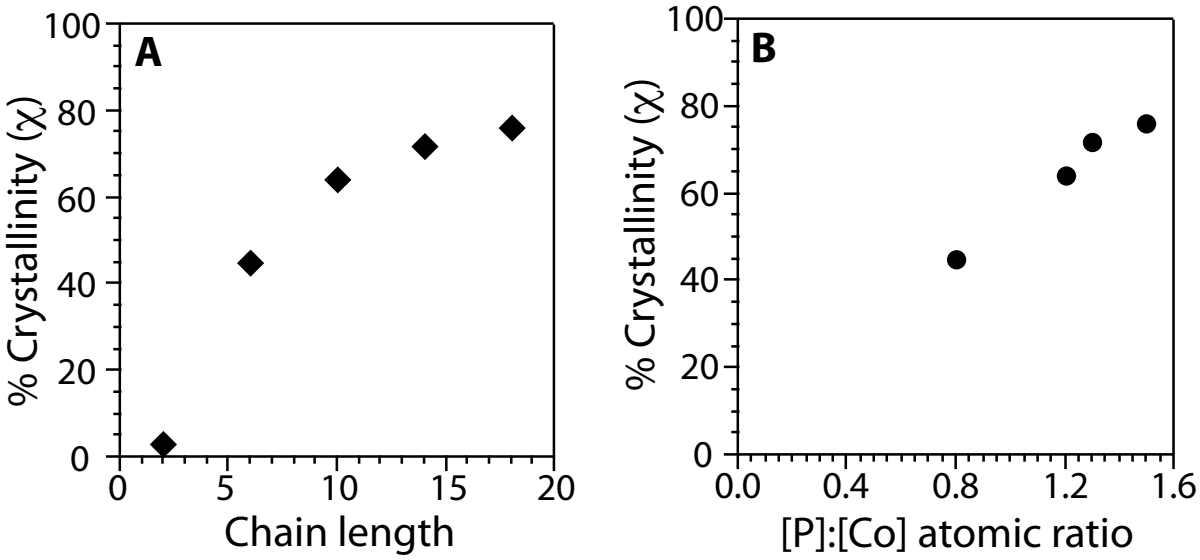

Figure 3.2. (A) Plot of percent crystallinity (χ)versus chain length (n = 2–18) for various NMC-grafted alkyl phosphonate coatings, demonstrating a monotonic increase in χ with chain length. (B) Plot of percent crystallinity (χ) versus [P]:[Co] ratio, showing a relatively linear increase in monolayer crystallinity with surface grafting density.

Composite cathodes constructed from alkylphosphonate grafted NMC cathode powders were fabricated and tested in half-cells against Li metal in a CR2032 coin cell geometry, in order to explore the effect of coating thickness on their cycling performances. The composite cathodes that we tested comprise 92 wt% NMC cathode powder, with Super C65 carbon black (4.5 wt%) as a conductive binder, and PVDF (3.5 wt%) as a high dielectric polymer medium. We focused our studies on NMC particles coated with EPA, DPA, TDPA, and ODPA (n = 2, 10, 14, and 18), since these particles exhibited similar surface coverages (*vide supra*). We also tested half-cells constructed from cathodes made from uncoated NMC. After two initial conditioning cycles (see Experimental Section for details), three half-cells of each type were cycled 50 times using 0.3 C

charge and 1 C discharge rates. From the averaged data for our triplicate runs shown in Figure 3.3, we find that the cathode cycling performance is not statistically different for the uncoated and the variously coated materials (see Supporting Information Figure A1.1 for full error analysis). Thus, we conclude that the presence of an alkylphosphonate coating does not apparently mitigate the observed capacity fade for these half-cells in long-term cycling tests as compared to the uncoated, control materials.

However, charge-discharge rate performance tests (performed in triplicate) on freshly produced half-cells derived from coated cathode powders revealed significant differences in cell behavior as a function of coating thickness (Figure 3.4). After two initial conditioning cycles (see Experimental Section), we found little difference in the 1C discharge performances of the various half-cells in four consecutive cycles. Upon charging the half-cell at 0.3 C and discharging it more quickly four times at each of 2C, 5C, 8C, and 10C, we found that the DPA and TDPA coatings exhibit statistically significant improvements in the specific discharge capacities at both 5C and 10C. At a 5C discharge rate, we observed that the specific discharge capacities for the DPA- and TDPA-coated cathodes were 10-20% better than the uncoated cathode materials (see Supporting Information Figure A1.2 for complete error uncertainties). The performance enhancement in the DPA and TDPA materials increases significantly upon discharging at 10 C, where we observe a 200-300% improvement in the discharge capacity as compared to the uncoated cathode. In order to verify that the NMC cathode materials were not irreversibly affected by the high C-rate cycling tests, we performed one final round of four cycle tests on each half-cell at 1C. These tests showed nearly identical specific discharge capacity to the initial 1C discharge test, indicating that the cathodes were not irreversibly damaged under these aggressive testing conditions. Thus, we conclude that the improved high C-rate

performance of the DPA and TDPA coated NMC materials originates from the organic molecular coating.

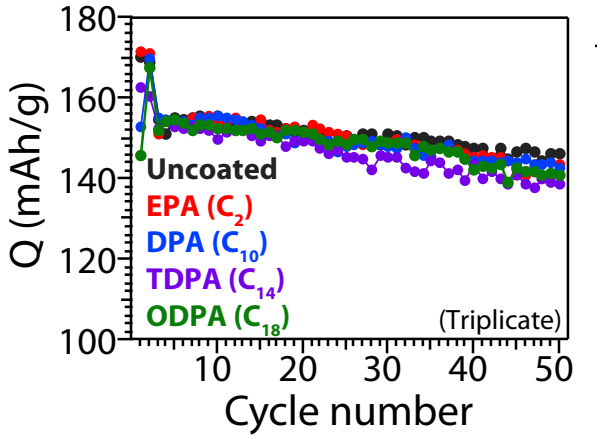

Figure 3.3. Cycle performance of NMC cathode materials grafted with various alkylphosphonate monolayers with alkyl chains ranging in length from C_2–C_{18}, indicating that their discharge capacities decay similarly upon initial conditioning by charging at 0.1 C and discharging at 0.1 C for the first two cycles, followed subsequent charging at 0.3 C and discharging at 1 C.

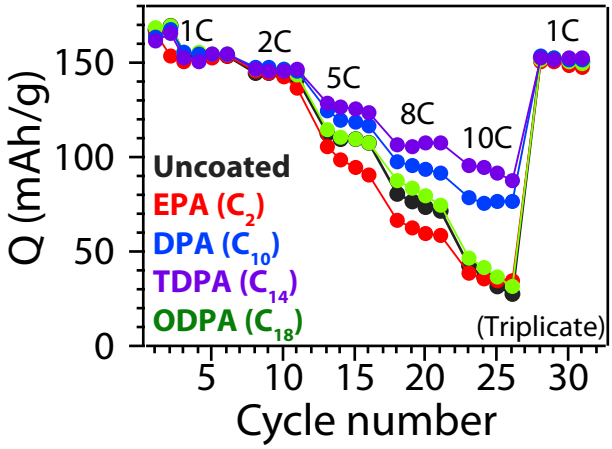

Figure 3.4. Lithium half–cell rate performance test results for NMC cathodes functionalized with various alkylphosphonate monolayers demonstrate that the DPA (C_{10}) and TDPA (C_{14}) monolayers minimize capacity loss at the highest discharge rates, enabling faster charge/discharge cycles. Half-cells were conditioned by charging at 0.1 C

and discharged at 0.1 C for the first two cycles, followed by repeated charging at 0.3 C and discharged at the specified rates C rates.

Electrochemical impedance spectroscopy (EIS) analyses of the half-cells before and after the above C-rate performance tests were conducted to understand better the protective effects of the phosphonate coatings. Nyquist plots for representative half-cells prior to the C-rate cycling tests exhibit a high frequency intercept that reflects the impedance associated with the solution resistance of the fresh 1 M $LiPF_6$ ethylene carbonate/dimethyl carbonate electrolyte (open symbols in Figure 3.5). The nearly invariant solution resistance across all cells, regardless of the surface coating, is consistent with the virgin electrolyte prior to any decomposition reactions due to cell cycling. The filled symbols in Figure 3.5 correspond to EIS spectra for half-cells after the complete series of C-rate cycling performance tests shown in Figure 3.4. These EIS data indicate that the high frequency intercept generally shifts to a higher value, which we attribute to electrolyte degradation under the testing conditions. This resistance change is ascribed to the extent to which the electrolyte decomposes upon cycling due to electrode-electrolyte interfacial contact. The changes in the solution resistance before and after rate testing averaged over three half-cells are given in Table 3.3 as a function of the coating type. These data suggest that the change in solution resistance decreases with increasing alkyl phosphonate chain length, implying that the longer alkyl chains protect the oxidizing cathode surface from contact with the electrolyte and thus mitigate its decomposition.

Table 3.3. Average Change in Solution Resistance After C-Rate Performance Testing.

Coating	ΔR_{soln} (Ω)[a]	$R_{interface}$ (Ω)[b]
EPA	3.8 ± 1.4	10.9 ±2.3
DPA	1.5 ± 0.3	19.0 ± 2.6
TDPA	0.90 ± 0.22	14.9 ± 0.6
ODPA	0.50 ± 0.27	12.5 ± 0.7

[a] ΔR_{soln} is calculated from the difference in the Z'(Ω) intercepts in the EIS Nyquist plots before and after C-rate performance testing. [b] $R_{interface}$ is calculated from the diameter of the semicircle observed after C-rate testing, shown in Figure 3.5.

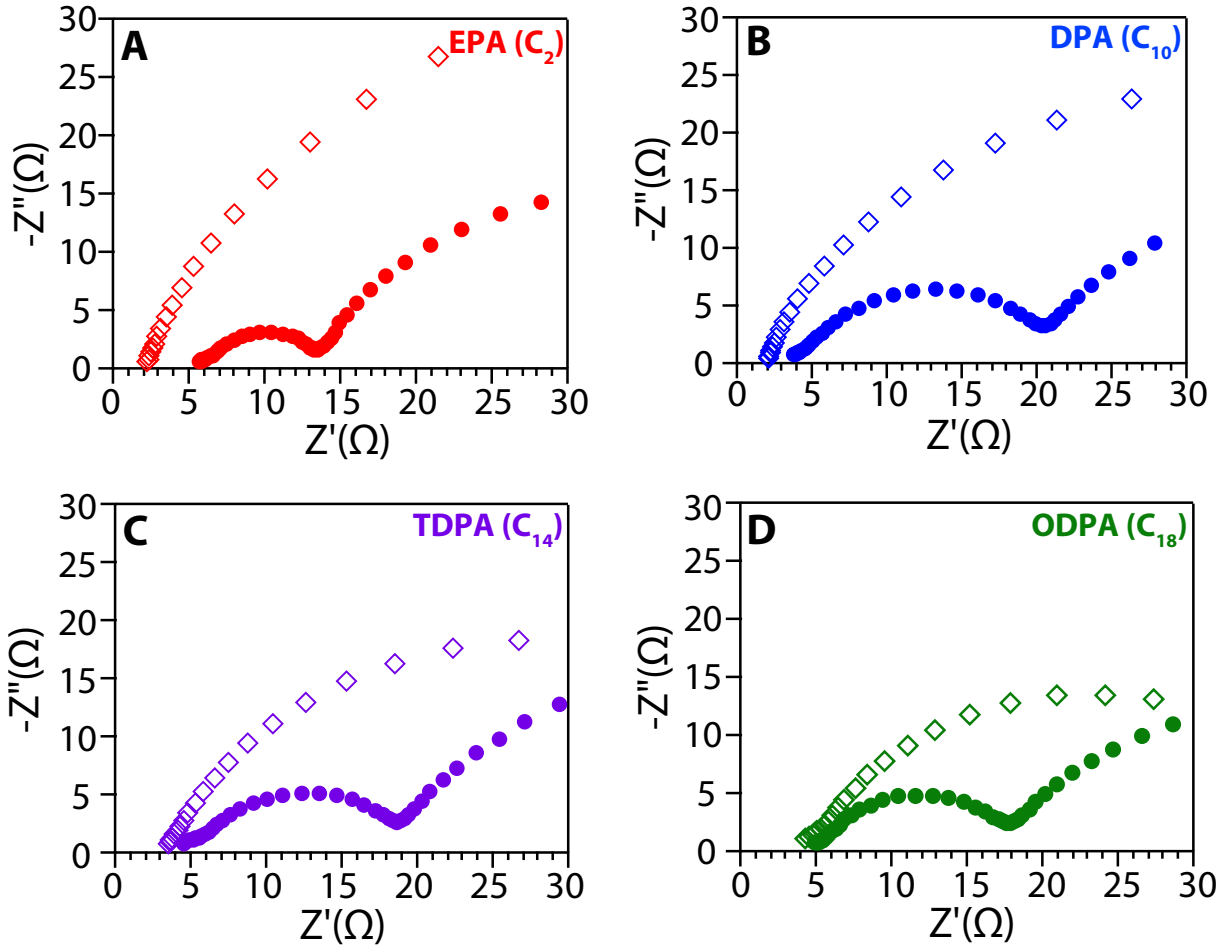

Figure 3.5. Nyquist plots for lithium half-cells comprising coated NMC cathode particles before (◇) and after(●) C-rate testing. The solution resistance change, which is deduced from the difference in the Z'(Ω) intercepts before and after C-rate testing, decreases with increasing alkyl chain length in manner consistent with longer alkyl chains conferring greater protection from electrolyte breakdown. The decreasing diameter of the semicircle observed after C-rate testing with increasing alkyl phosphonate chain length suggests that longer chains lead to less resistive surface layers after cell cycling. (See Figure A1.3 for complete Nyquist plots.)

EIS also provides additional information about the interfacial resistance associated with the alkyl phosphonate surface coating, in addition to any SEI layer that forms from electrolyte

decomposition at the NMC particle surface.[44-45] We fit the Nyquist plot using the equivalent circuit model $R_{soln} + C_{interface}/R_{interface} + C_{CT}/R_{CT}$, where R_{soln} is the solution resistance, $C_{interface}$ and $R_{interface}$ are the respective interfacial capacitance and resistance of interest, and C_{CT} and R_{CT} are the charge transfer capacitance and resistance associated with intercalation of Li^+ into the NMC cathode particles. $R_{interface}$ is the diameter of the first semicircle in the Nyquist plot, the values of which are given in Table 3 as a function of the coating chain length. The fact that the $R_{interface}$ attains a maximum value for DPA (n = 10) reflects a convolution of two opposing trends related to electrolyte decomposition and the intrinsic, thickness-dependent resistance of the organic coating. The thin EPA (n = 2) coating affords little surface protection from the electrolyte and only a small intrinsic interfacial resistance as evidenced by the large ΔR_{soln}, which leads us to conclude that the dominant contribution to $R_{interface}$ is from the electrolyte decomposition products forming an SEI layer at the active material surfaces. In the thickest ODPA (n = 18) coating, the small ΔR_{soln} indicates that SEI formation from electrolyte decomposition is minimal and thus the long alkyl chain is the primary contributor to $R_{interface}$. When $2 < n < 18$, there is a trade off between coating thickness and mitigation of electrolyte decomposition afforded by monolayer crystallinity. For DPA (n = 10) specifically, the intrinsic interfacial resistance of the coating is high and the modest crystallinity of the monolayer does not fully protect the electrolyte from cathode surface decomposition reactions. Thus, the observed $R_{interface}$ is highest in this case, due to large resistances associated with both the coating and the deposited SEI.

The above EIS analyses also provide insights into the somewhat surprising behavior of the alkyl phosphonate–coated NMC cathode materials in rate performance tests. C-rate performance tests reflect the rate of mass transfer of Li ions through the coating to the electrode

surface for intercalation (Figure 3.4). The thickest ODPA (n = 18) coating exhibits the highest crystallinity (densest chain packing) and the lowest ΔR_{soln} value, implying that electrolyte degradation is minimized but also that lithium ions cannot easily reach the surface as required for intercalation. Thus, lithium ion intercalation is slow and the rate performance is poor. In the case of the uncoated and EPA-coated material with an amorphous surface layer, the rate performance is likely poor due to electrolyte decomposition (relatively high ΔR_{soln}) that forms an inorganic SEI layer that prevents lithium ion intercalation into the cathode particles. In the case of the DPA (n = 10) and TDPA (n = 14) coatings, the low values of ΔR_{soln} imply that the semicrystalline surface layer (χ = 65–75%) affords a modest degree of protection from electrolyte decomposition while still allowing lithium ion intercalation. Thus, there is an optimal coating thickness through which lithium ion intercalation is still possible without allowing substantial electrolyte degradation, especially, at a discharge rate of 10C as shown in Figure 3.6.

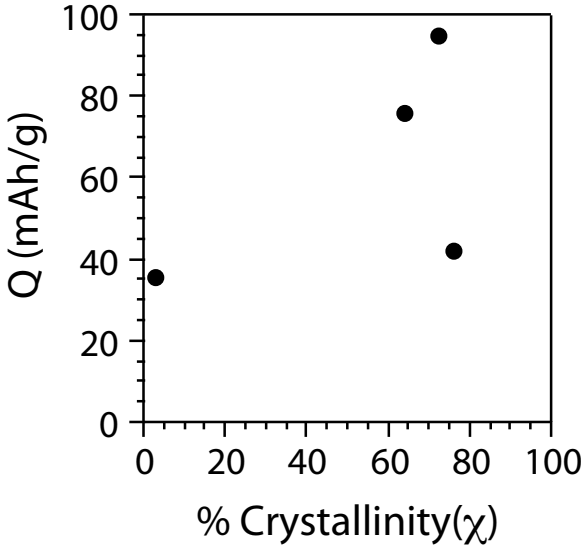

Figure 3.6. Specific discharge capacity measured at 10C discharge rate for various alkyl phosphonate coatings on NMC surface. Alkyl phosphonate coatings with 65–75 % crystallinity exhibit better specific discharge capacity, as compared to other alkyl

phosphonate coatings.

While the aforementioned effects are likely the dominant factors governing the rate performance behaviors of the coated NMC cathode particles, particle wettability by the electrolyte may play a secondary role in the observed performance. Previous studies have indicated that increasing the alkyl chain length of an alkyl phosphonate ligand grafted to a planar substrate significantly increases the advancing and receding contact angles for water, suggesting increased hydrophobicity of the water/coating interface.[41] On this basis, we anticipate that surface ligands with longer alkyl chains that form more tightly packed, crystalline surface layers may exhibit lower wettability by the electrolyte. Due to the small particle size associated with the NMC cathode particles, we were unable to directly and reliably measure the contact angles of the electrolyte solutions on the variously grafted cathode particles.

3.4 Conclusion

We have grafted various straight chain C_2-C_{18} alkyl phosphonic acids into NMC cathode particles to produce electrically insulating coatings of precisely controlled thicknesses, in order to identify the ideal coating characteristics that optimize overall electrochemical cell performance. We found that increasing the alkyl chain length of a phosphonic acid surface ligand results in higher surface coating crystallinities as quantified by DRIFTS measurements. The propensity for electrolyte decomposition decreases with increasing alkyl chain length due to monolayer crystallinity, yet the intrinsic interfacial resistance of the molecular layer also increases. Rate performance tests demonstrate that there is an optimal surface coating thickness of ~ 1.7 nm (tetradecylphosphonate) and crystallinity (~65-75%) that minimizes electrolyte decomposition while still allowing effective Li ion intercalation at rates as high at 10C. This

study suggests that careful control over cathode coating thickness and morphology can lead to improved rate performance of NMC cathode materials by controlling the relative rates of electrolyte degradation and lithium ion transport to insertion into the cathode. We anticipate that these surface coating design criteria may be more general and could be extended to other types of electrically insulating cathode coatings to improve battery cycling and rate performance.

3.5 References

1. Scrosati, B.; Garche, J., Lithium batteries: Status, prospects and future. *J. Power Sources* **2010,** *195* (9), 2419-2430.

2. Amine, K.; Kanno, R.; Tzeng, Y., Rechargeable lithium batteries and beyond: Progress, challenges, and future directions. *MRS Bulletin* **2014,** *39* (05), 395-401.

3. Kim, I. T.; Knight, J. C.; Celio, H.; Manthiram, A., Enhanced electrochemical performances of Li-rich layered oxides by surface modification with reduced graphene oxide/AlPO4 hybrid coating. *J. Mater. Chem. A* **2014,** *2* (23), 8696.

4. Manthiram, A., Materials Challenges and Opportunities of Lithium Ion Batteries. *J. Phys. Chem. Lett.* **2011,** *2* (3), 176-184.

5. Goodenough, J. B., Evolution of Strategies for Modern Rechargeable Batteries. *Acc. Chem. Res.* **2013,** *46*, 1053.

6. Armand, M.; Endres, F.; MacFarlane, D. R.; Ohno, H.; Scrosati, B., Ionic-liquid materials for the electrochemical challenges of the future. *Nat. Mater.* **2009,** *8* (8), 621-9.

7. Goodenough, J. B.; Kim, Y., Challenges for Rechargeable Li Batteries. *Chem. Mater.* **2010,** *22* (3), 587-603.

8. Kraytsberg, A.; Ein-Eli, Y., Higher, Stronger, Better…A Review of 5 Volt Cathode Materials for Advanced Lithium-Ion Batteries. *Adv. Energy Mater.* **2012,** *2* (8), 922-939.

9. Wu, Z.; Ji, S.; Zheng, J.; Hu, Z.; Xiao, S.; Wei, Y.; Zhuo, Z.; Lin, Y.; Yang, W.; Xu, K.; Amine, K.; Pan, F., Prelithiation Activates Li(Ni0.5Mn0.3Co0.2)O2 for High Capacity and Excellent Cycling Stability. *Nano Lett.* **2015,** *15* (8), 5590-6.

10. Yoshida, T.; Takahashi, M.; Morikawa, S.; Ihara, C.; Katsukawa, H.; Shiratsuchi, T.; Yamaki, J.-i., Degradation Mechanism and Life Prediction of Lithium-Ion Batteries. *J. Electrochem. Soc.* **2006,** *153* (3), A576.

11. Xu, K.; von Cresce, A., Interfacing electrolytes with electrodes in Li ion batteries. *J. Mater. Chem.* **2011,** *21* (27), 9849.

12. Vetter, J.; Novak, P.; Wagner, M. R.; Veit, C.; Moller, K. C.; Besenhard, J. O.; Winter, M.; Wohlfahrt-Mehrens, M.; Vogler, C.; Hammouche, A., Ageing mechanisms in lithium-ion batteries. *J. Power Sources* **2005,** *147* (1-2), 269-281.

13. Aravindan, V.; Gnanaraj, J.; Madhavi, S.; Liu, H. K., Lithium-ion conducting electrolyte salts for lithium batteries. *Chem. Eur. J.* **2011,** *17* (51), 14326-46.

14. Xu, K., Nonaqueous liquid electrolytes for lithium-based rechargeable batteries. *Chem. Rev.* **2004,** *104* (10), 4303-417.

15. Bloom, I.; Trahey, L.; Abouimrane, A.; Belharouak, I.; Zhang, X.; Wu, Q.; Lu, W.; Abraham, D. P.; Bettge, M.; Elam, J. W.; Meng, X.; Burrell, A. K.; Ban, C.; Tenent, R.; Nanda, J.; Dudney, N., Effect of interface modifications on voltage fade in $0.5Li_2MnO_3{\cdot}0.5LiNi_{0.375}Mn_{0.375}Co_{0.25}O_2$ cathode materials. *J. Power Sources* **2014,** *249*, 509-514.

16. Su, Y.; Cui, S.; Zhuo, Z.; Yang, W.; Wang, X.; Pan, F., Enhancing the High-Voltage Cycling Performance of LiNi0.5Mn0.3Co0.2O2 by Retarding Its Interfacial Reaction with an Electrolyte by Atomic-Layer-Deposited Al2O3. *ACS Appl. Mater. Interfaces* **2015,** *7* (45), 25105-12.

17. Li, X.; Liu, J.; Meng, X.; Tang, Y.; Banis, M. N.; Yang, J.; Hu, Y.; Li, R.; Cai, M.; Sun, X., Significant impact on cathode performance of lithium-ion batteries by precisely controlled metal oxide nanocoatings via atomic layer deposition. *J. Power Sources* **2014,** *247*, 57-69.

18. Kim, J. W.; Kim, D. H.; Oh, D. Y.; Lee, H.; Kim, J. H.; Lee, J. H.; Jung, Y. S., Surface chemistry of LiNi0.5Mn1.5O4 particles coated by Al2O3 using atomic layer deposition for lithium-ion batteries. *J. Power Sources* **2015,** *274*, 1254-1262.

19. Sun, Y. K.; Lee, M. J.; Yoon, C. S.; Hassoun, J.; Amine, K.; Scrosati, B., The role of AlF3 coatings in improving electrochemical cycling of Li-enriched nickel-manganese oxide electrodes for Li-ion batteries. *Adv. Mater.* **2012,** *24* (9), 1192-6.

20. Huang, Y.; Chen, J.; Ni, J.; Zhou, H.; Zhang, X., A modified ZrO2-coating process to improve electrochemical performance of Li(Ni1/3Co1/3Mn1/3)O2. *J. Power Sources* **2009,** *188* (2), 538-545.

21. Wu, F.; Zhang, X.; Zhao, T.; Li, L.; Xie, M.; Chen, R., Multifunctional AlPO4 coating for improving electrochemical properties of low-cost Li[Li0.2Fe0.1Ni0.15Mn0.55]O2 cathode materials for lithium-ion batteries. *ACS Appl. Mater. Interfaces* **2015,** *7* (6), 3773-81.

22. Quinlan, R. A.; Lu, Y.-C.; Kwabi, D.; Shao-Horn, Y.; Mansour, A. N., XPS Investigation of the Electrolyte Induced Stabilization of LiCoO2and "AlPO4"-Coated LiCoO2Composite Electrodes. *J. Electrochem. Soc.* **2015,** *163* (2), A300-A308.

23. Lee, K.-S.; Myung, S.-T.; Kim, D.-W.; Sun, Y.-K., AlF3-coated LiCoO2 and Li[Ni1/3Co1/3Mn1/3]O2 blend composite cathode for lithium ion batteries. *J. Power Sources* **2011,** *196* (16), 6974-6977.

24. Zhong, Z. Y.; Yin, Y. D.; Gates, B.; Xia, Y. N., Preparation of mesoscale hollow spheres of TiO2 and SnO2 by templating against crystalline arrays of polystyrene beads. *Adv. Mater.* **2000,** *12* (3), 206-209.

25. Leskela, M.; Ritala, M., Atomic layer deposition chemistry: recent developments and future challenges. *Angew. Chem. Int. Ed. Engl.* **2003,** *42* (45), 5548-54.

26. Gao, W.; Dickinson, L.; Grozinger, C.; Morin, F. G.; Reven, L., Self-assembled monolayers of alkylphosphonic acids on metal oxides. *Langmuir* **1996,** *12* (26), 6429-6435.

27. Mutin, P. H.; Guerrero, G.; Vioux, A., Hybrid materials from organophosphorus coupling molecules. *J. Mater. Chem.* **2005,** *15* (35-36), 3761.

28. Yildirim, O.; Yilmaz, M. D.; Reinhoudt, D. N.; Blank, D. H.; Rijnders, G.; Huskens, J., Electrochemical stability of self-assembled alkylphosphate monolayers on conducting metal oxides. *Langmuir* **2011,** *27* (16), 9890-4.

29. Queffelec, C.; Petit, M.; Janvier, P.; Knight, D. A.; Bujoli, B., Surface modification using phosphonic acids and esters. *Chem. Rev.* **2012,** *112* (7), 3777-807.

30. Zeller, A.; Musyanovych, A.; Kappl, M.; Ethirajan, A.; Dass, M.; Markova, D.; Klapper, M.; Landfester, K., Nanostructured coatings by adhesion of phosphonated polystyrene particles onto titanium surface for implant material applications. *ACS Appl. Mater. Interfaces* **2010,** *2* (8), 2421-8.

31. Zhang, L.; Cole, J. M., Anchoring groups for dye-sensitized solar cells. *ACS Appl. Mater. Interfaces* **2015,** *7* (6), 3427-55.

32. Paramonov, P. B.; Paniagua, S. A.; Hotchkiss, P. J.; Jones, S. C.; Armstrong, N. R.; Marder, S. R.; Brédas, J.-L., Theoretical Characterization of the Indium Tin Oxide Surface and of Its Binding Sites for Adsorption of Phosphonic Acid Monolayers. *Chem. Mater.* **2008,** *20* (16), 5131-5133.

33. Paniagua, S. A.; Li, E. L.; Marder, S. R., Adsorption studies of a phosphonic acid on ITO: film coverage, purity, and induced electronic structure changes. *Phys. Chem. Chem. Phys.* **2014,** *16* (7), 2874-81.

34. Marcinko, S.; Fadeev, A. Y., Hydrolytic Stability of Organic Monolayers Supported on TiO2and ZrO2. *Langmuir* **2004,** *20* (6), 2270-2273.

35. Lomoschitz, C. J.; Feichtenschlager, B.; Moszner, N.; Puchberger, M.; Muller, K.; Abele, M.; Kickelbick, G., Directing alkyl chain ordering of functional phosphorus coupling agents on ZrO2. *Langmuir* **2011,** *27* (7), 3534-40.

36. Raman, A.; Dubey, M.; Gouzman, I.; Gawalt, E. S., Formation of self-assembled monolayers of alkylphosphonic acid on the native oxide surface of SS316L. *Langmuir* **2006,** *22* (15), 6469-72.

37. Paniagua, S. A.; Giordano, A. J.; Smith, O. L.; Barlow, S.; Li, H.; Armstrong, N. R.; Pemberton, J. E.; Bredas, J. L.; Ginger, D.; Marder, S. R., Phosphonic Acids for Interfacial Engineering of Transparent Conductive Oxides. *Chem. Rev.* **2016,** *116* (12), 7117-58.

38. Hanson, E. L.; Schwartz, J.; Nickel, B.; Koch, N.; Danisman, M. F., Bonding self-assembled, compact organophosphonate monolayers to the native oxide surface of silicon. *J. Am. Chem. Soc.* **2003,** *125* (51), 16074-80.

39. Hanson, E. L.; Guo, J.; Koch, N.; Schwartz, J.; Bernasek, S. L., Advanced surface modification of indium tin oxide for improved charge injection in organic devices. *J. Am. Chem. Soc.* **2005,** *127* (28), 10058-62.

40. English, C. R.; Bishop, L. M.; Chen, J.; Hamers, R. J., Formation of self-assembled monolayers of pi-conjugated molecules on TiO2 surfaces by thermal grafting of aryl and benzyl halides. *Langmuir* **2012,** *28* (17), 6866-76.

41. Spori, D. M.; Venkataraman, N. V.; Tosatti, S. G.; Durmaz, F.; Spencer, N. D.; Zurcher, S., Influence of alkyl chain length on phosphate self-assembled monolayers. *Langmuir* **2007,** *23* (15), 8053-60.

42. Metoki, N.; Liu, L.; Beilis, E.; Eliaz, N.; Mandler, D., Preparation and characterization of alkylphosphonic acid self-assembled monolayers on titanium alloy by chemisorption and electrochemical deposition. *Langmuir* **2014,** *30* (23), 6791-9.

43. Paniagua, S. A.; Hotchkiss, P. J.; Jones, S. C.; Marder, S. R.; Mudalige, A.; Marrikar, F. S.; Pemberton, J. E.; Armstrong, N. R., Phosphonic Acid Modification of Indium–Tin Oxide Electrodes: Combined XPS/UPS/Contact Angle Studies. *J. Phys. Chem. C* **2008,** *112* (21), 7809-7817.

44. Alcántara, R.; Jaraba, M.; Lavela, P.; Tirado, J. L., X-ray diffraction and electrochemical impedance spectroscopy study of zinc coated LiNi0.5Mn1.5O4 electrodes. *J. Electroanal. Chem.* **2004,** *566* (1), 187-192.

45. Liu, J.; Manthiram, A., Understanding the Improvement in the Electrochemical Properties of Surface Modified 5 V $LiMn_{1.42}Ni_{0.42}Co_{0.16}O_4$ Spinel Cathodes in Lithium-ion Cells. *Chem. Mater.* **2009,** *21* (8), 1695-1707.

46. C. J. Powell; A. Jablonski, *NIST Electron Inelastic-Mean-Free-Path Database*, Version 1.2, SRD 71, National Institute of Standards and Technology, Gaithersburg, MD (2010)

CHAPTER 4

$LiNi_{0.5}Mn_{0.3}Co_{0.2}O_2$ CATHODE SURFACE REACTIVITY : ROLE OF TRANSITION METALS AT THE ELECTRODE SURFACE

4.1 Introduction

Although lithium–ion batteries are ubiquitous in the low power consumer electronics, their widespread implementation in high power applications is limited by the power deliverable from commercially available battery materials. The development of high voltage cathodes based on the layered metal oxide $LiNi_xMn_yCo_{1-x-y}O_2$ (NMC) provides a potential means of addressing the need for new materials, which will enable the high power batteries required for electric vehicles and large scale electric grid energy storage and utilization.[1-6] However, NMC cathodes exhibit significant charge-discharge capacity losses after long-term cycling, as a consequence of structural transformations in the active material during electrochemical cycling, dissolution of transition metals from its surface, and parasitic redox reactions at the electrode/electrolyte interface that consume lithium.[7-12] A variety of strategies for mitigating the latter two issues have emerged, including optimizing battery charge and discharge rates, and the development of sacrificial electrolyte additives that decompose at the cathode surface to generate surface layers that prevent electrolyte contact and breakdown.[13-20] One of the most popular strategies for improving capacity retention in NMC materials is to coat them with electrically insulating metal oxides through which Li^+ ions may still diffuse.[8, 21-25]

While the aforementioned approaches have provided some practical gains in NMC cathode performance, a fundamental understanding of the surface reactivity of NMC with electrolytes is lacking. At present, it is unknown which of the Ni, Mn, or Co sites on the NMC surface decompose the $LiPF_6$/organic carbonate electrolytes that are typically used in Li-ion batteries,[26] and whether these processes are stoichiometric or catalytic reactions.[10, 27] The intrinsic surface reactivity of NMC cathodes is probably spatially heterogeneous and dependent on various factors, which include the specific metals presented at the surface and the nature of the exposed crystal facets of the cathode particles.[28-29] The paucity of knowledge regarding NMC cathode surface chemistry renders the rational development of new and more effective strategies for their performance optimization a difficult task.

Inspired by experimental approaches for studying heterogeneous catalysts,[30-33] this study focuses on understanding the different reactivities of various NMC surface sites through their selective and reversible surface passivation. We demonstrate a new template-directed ligand grafting strategy for the kinetically controlled, selective coating of specific metal sites on NMC surfaces with two different linear alkyl phosphonate surface ligands. This three-step approach enables the formation of spatially heterogeneous, mixed monolayer coatings of the two ligands on the NMC, in which the most reactive sites are coated with either decylphosphonic acid (D) or octadecylphosphonic acid (OD) in the first step. In a second step, the balance of the surface is coated with the other surface ligand. In conjunction with X-ray photoelectron spectroscopy analyses of the coated cathode materials, comparative evaluation of coated NMC cathode charge-discharge performance and discharge rate performance in lithium half-cells provides new

insights into the nature of the surface sites that most adversely impact long-term NMC cathode cycling performance.

4.2 **Experimental Section**

Materials. All materials, reagent grade, and anhydrous solvents were purchased from Sigma–Aldrich Chemical Co. (Milwaukee, WI) and used as received unless otherwise noted. Lithium foil (0.2 mm thick) was obtained from Rockwood Lithium (Kings Mountain, NC) and stored under an argon atmosphere. The Dow Chemical Company (Midland, MI) supplied $LiNi_{0.5}Mn_{0.3}Co_{0.2}O_2$ (NMC) cathode powder, with a surface area of 0.5 m^2/g from BET analysis. Supplied by BASF (Florham Park, NJ), the 1 M $LiPF_6$ in 50:50 *v/v* ethylene carbonate:diethyl carbonate electrolyte was stored under argon in a glovebox. TIMCAL Super C65 carbon black and SOLVAY Solef 5130 PVDF were used as received in the fabrication of composite NMC cathodes. CR2032 coin cell parts (gasket, cap, and case) were purchased from Pred Materials International, Inc. Celgard 2500 separators were cut into 1.9 cm in diameter discs and dried at 40 °C under vacuum for 12 h. The dried Celgard separators were then immersed the aforementioned electrolyte for a minimum of 12 h, prior to their incorporation into lithium half-cells as described below.

X–ray Photoelectron Spectroscopy (XPS). XPS spectra were measured using a ThermoFisher K–Alpha™ X-ray Photoelectron Spectrometer with monochromatic micro-focused Al *K*a X–rays (1486.6 eV) with 400 μm spot size, a pass energy of 50.0 eV, an analyzer resolution of 0.1 eV, and a 90° take–off angle. All spectra were referenced using a peak binding energy of C (1s) at 285 eV. After spectral baseline correction using the using the Smart function

in the ThermoScientific Avantage software, peak positions and relative peak areas for P (2p) and Co (2p) were calculated by fitting them to a weighted combination of Gaussian and Lorentzian functions (30% Gaussian, 70% Lorentzian), followed by signal normalization according to the atomic sensitivity factors 1.353 for P (2p) and 18.235 for Co (2p).

Mixed Monolayer Surface Coating of NMC. This multi-step procedure represents a modification of our previously reported methodology for applying single component linear alkyl phosphonate surface coatings (D or OD) to NMC cathodes particles.[34]

NMC (2.5 g) was placed in a Uvotech ProCleanerTM 110 UV-ozone cleaner (l = 189.4 and 253.7 nm) to remove organic surface contaminants. The cleaned NMC powder was immersed in a solution of benzyl bromide (BB, 5.3 mL, 0.045 mol) in anhydrous toluene (44.7 mL) and stirred at 80 °C for 17 h, after which the BB-treated NMC was collected on a Whatman, Inc. filter paper (15-19 μm pore size). This powder was thoroughly washed with anhydrous toluene (3 x 50 mL) at ambient temperature, in order to remove unreacted BB. The NMC was exhaustively dried under vacuum at ambient temperature prior to proceeding to the next step.

The dried BB-treated NMC (2.5 g) was slurried in an anhydrous ethanol solution (10 mL) containing decylphosphonic acid (D, ~6–8 mg) at ambient temperature for 17 h. This D solution concentration reflects a three-fold excess of that required to coat the entire NMC surface, as calculated from the NMC surface area and by assuming a phosphonic acid surface binding area of 0.24 nm^2/molecule.[35] The resulting BB-D coated NMC was isolated by high-speed centrifugation and decanting the supernatant liquid. To remove any ungrafted acid, the resulting powder was washed by three consecutive cycles of stirring in ethanol (10 mL) for 5 min at ambient temperature, centrifugation, and decanting the supernatant solution. The BB-D NMC

was then dried *in vacuo* and then heated to 150 °C under vacuum for 48 h to effect the removal of the BB-derived coating.

The partially D-coated NMC powder was then stirred in an anhydrous ethanol solution (10 mL) containing octadecylphosphonic acid (OD, ~6–8 mg) at ambient temperature for 17 h. Again, this OD ligand solution concentration reflects a three-fold excess of that required to completely coat the bare NMC surface. The NMC particles bearing a mixed alkyl phosphonate coating were isolated by centrifugation and removal of the supernatant liquid, followed by three ethanol washing steps as described above. The coated D-OD NMC powder was then dried in vacuum prior to analysis and fabrication of composite cathode discs for electrochemical testing.

Note that the order of application of the phosphonic acid surface ligands may be interchanged to furnish a OD-D coating on the NMC powder, whereby the order in which the ligands are listed reflects the order of their application.

Composite Cathode Disc Fabrication. Super C65 carbon black (0.00978 g), a PVDF solution (0.9278 g PVDF, 8.2 wt % in *N*-methyl pyrrolidone) and NMP (0.4 mL) were mixed in a planetary centrifugal Thinky Mixer (ARE–310) at 2000 rpm for 4 min, after which the speed was increased to 2200 rpm for 30 sec. *N*-methylpyrrolidone (0.4 mL) was added to the slurry and the mixing procedure was repeated. The mixed alkyl phosphonate–grafted NMC (2 g) was then added to the slurry, and the mixing procedure was again repeated. An Elcometer 4340 Automatic Film Applicator was used to cast the resulting slurry onto 15 mm thick Al foil (MTI Corp., Richmond, CA), and this cast film was dried under vacuum at 40 °C for 16 h. 15 mm diameter discs were punched out of the resulting solvent-cast cathode sheet, and the discs were individually calendared under a force of 1.8 tons for 8 min in a Carver 3851–0 melt press. The

calendared cathodes were transferred to an argon-filled glovebox, in which they were once thoroughly dried at 140 °C under vacuum for 12 h prior to storage.

Half-Cell Assembly and Testing. Lithium half–cells in CR2032 coin cell format were assembled in a glovebox under argon as follows. Prior to cell assembly, each cathode disc was weighed to enable precise calculation of the expected specific capacity of the cell. 16 mm diameter anode discs were punched out of lithium foil (0.2 mm thick). The half-cell was assembled by sequentially stacking the following items into the top cap of the CR2032 coin cell: a 16 mm stainless steel spacer, a 16 mm lithium foil anode disc, 40 μl of 1 M $LiPF_6$ in 50:50 *v/v* ethylene carbonate:diethyl carbonate electrolyte, a Celgard separator pre-soaked in the electrolyte, a plastic gasket, and another 40 μl of electrolyte. The cathode disc was then placed on top of the separator, followed by a stainless steel metal spring, and finally the bottom cap. A Hohsen automatic coin cell crimper (Osaka, Japan) was used to crimp seal the cell.

Half-cells were cycled in an Arbin BT2000 battery test station instrument between 3.0–4.3 V vs. Li/Li^+ at 40 ºC. Prior to any measurements, each cell was conditioned by two cycles of charging at 0.1 C and discharging at 0.1 C. Discharge capacity retention measurements employed a 0.3 C charge rate and 1 C discharge rate. Discharge rate performance tests utilized a charge rate of 0.3 C and increasing discharge rates of 1, 2, 5, 8 and 10 C. One final 1 C discharge rate performance test was conducted to assess whether or not high C-rate testing irreversibly damaged the cells.

Electrochemical Impedance Spectroscopy (EIS). EIS measurements were performed using a Biologic SP–200 potentiostat over a frequency range w = 0.1 Hz –10^5 Hz with an applied potential 10 mV versus the half-cell open circuit voltage (OCV). Three EIS measurements were

taken prior to half-cell conditioning and after discharge rate performance testing, with a 5 min resting interval between each measurement to enable equilibration of any electrochemical potential gradients.

4.3 Results and Discussion

We previously reported investigations of the surface grafting behaviors of linear alkyl phosphonic acids ($C_nH_{2n+1}PO_3H_2$, n = 2, 6, 10, 14, and 18) onto $LiNi_{0.5}Mn_{0.3}Co_{0.2}O_2$ (NMC) cathode particles, and the effects of these alkyl phosphonate monolayer coatings on their lithium half-cell cycling performances as a function of chain length. Short chain ethyl phosphonic acid coatings (n = 2) allowed significant electrolyte decomposition to occur with no performance gains. On the other hand, long chain octadecylphosphonic acid (OD, n = 18) coatings prevent electrolyte degradation, at the expense of significantly reducing Li^+ permeability therein and decreasing the rate of Li^+ (de)intercalation into the NMC. Intermediate length decyl phosphonic acid (D, n = 10) coatings decreased electrolyte decomposition with significantly improved discharge capacity rate performance. Thus, intermediate thickness coatings mitigate parasitic electrolyte decomposition reactions, while allowing Li-ion permeation through the coating to achieve improved discharge rate performance characteristics.

Based on these findings, we sought to investigate whether the performance of NMC cathodes coated with mixed D/OD alkyl phosphonate monolayers could synergistically combine the protective nature of the long chain OD ligands and the permeability of the intermediate chain length D coating. Given the chemical heterogeneity and differential metal site reactivities on the NMC surface, we hypothesized that an ideal coating would place the more protective OD coating

on the sites most reactive with the electrolyte, while the D ligand would ideally coat the less reactive sites and enable efficient Li^+ permeation and cathode (de)intercalation.

Given our goal of differentially coating NMC surface sites with different reactivities, we naturally sought a robust method for kinetically controlling the deposition of mixed D/OD monolayers (Figure 4.1). One documented electrolyte decomposition reaction at high voltage Li-ion battery cathode surfaces is nucleophilic attack by surface metal–hydroxyls on the carbonate moieties of the organic carbonate electrolyte solvent.[36] Thus, we reasoned that treatment of the NMC powder with an organic electrophile might serve to cap or to "protect" these nucleophilic metal-hydroxyl sites. Subsequent solution coating of the cathode particles with D would direct the incoming surface ligands to the less reactive surface sites. Removal of the reactive site "protecting group" from the surface without disrupting the templated D coating would then unmask the reactive surface moieties for subsequent coating with a protective OD ligand, to yield the desired mixed monolayer. We also envisioned that the order of application of the alkyl phosphonates could be interchanged to study the effect of coating the less reactive sites with OD and the more reactive metal-hydroxyl sites with D ligands.

We initially identified benzyl bromide (BB) as a potentially removable, surface-reactive, hydroxyl protecting group for templating spatially heterogeneous mixed D/OD coatings on NMC. BB is an activated electrophile that rapidly reacts with alkoxy or hydroxy nucleophiles by nucleophilic displacement of a bromide anion to yield the benzylic ethers or alcohols. Thus, we reasoned that BB might react with the NMC surface hydroxyls to generate a benzylated surface. We further hypothesized that the surface-bound benzyl moieties would be susceptible to thermolytic cleavage at elevated temperatures to deprotect the reactive surface sites, by benzyl

radical homolysis and gas phase recombination to form a bibenzyl reaction byproduct. Thermolytic surface deprotection of the benzyl groups is appealing, since alkylphosphonate monolayers are quite thermally stable.

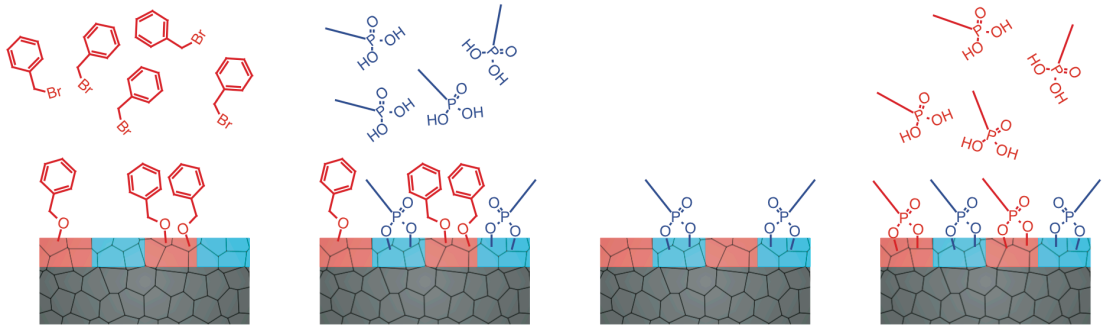

Figure 4.1. Schematic depiction of the three-step generation of the patchy mixed alkyl phosphonate coatings on NMC cathode particles (*grey*): (1) reaction of the NMC surface with benzyl bromide (BB) protects the more reactive red sites and directs the incoming phosphonic acid (*blue*) to the remaining open surface sites, (2) thermolysis of the BB-derived template reveals the reactive surface sites (*red*), thus allowing (3) grafting of the second phosphonic acid (red) to make a mixed coating.

We initially grafted BB onto the surface of a NMC powder sample, which had been freed of organic surface contaminants by UV-ozone cleaning (see Experimental Section). Direct assessment of the grafting density of the surface-bound benzyl functionalities using X-ray photoelectron spectroscopy (XPS) failed, due to significant uncertainties associated with ubiquitous carbon contamination in the sample environment and the lack of any distinguishing heteroatoms in the benzyl ligand that enabled definitive surface coverage quantitation. Consequently, we solution grafted D from an ethanolic solution onto the benzylated NMC to generate a sample with a mixed coating designated BB-D on NMC. Hereon, the order in which the surface ligands are listed reflects the order of their application. Quantitative XPS analyses

revealed that the atom percent ratio [P]:[Co] = 0.5 for the BB-D coating, whereas NMC bearing a pure D monolayer exhibits [P]:[Co] = 1.2 from our previous studies.[34] On this basis, we calculate that the D ligand in the BB-D sample covers ~40% of the available surface, and thus the BB covers the remaining ~60% of the exposed NMC surface area. Therefore, BB apparently templates the partial grafting of the D ligand on NMC.

We proceeded to heat the BB-D on NMC coating to 150 °C under vacuum for 48 h, in an attempt to thermolytically deprotect the benzylated-surface sites while also driving D alkylphosphonate ligand grafting to the NMC surface by high temperature dehydration. To assess the efficacy of the thermolytic surface deprotection reaction, we again solution grafted D from an ethanol solution onto the heated treated, partially D-coated NMC. Quantitative XPS analysis of the resulting D-D sample revealed that the surface atom percent ratio increased to [P]:[Co] = 1.1. Since the D ligand only reacts with free surface hydroxyl groups, this increase in D ligand grafting density indicates that high vacuum thermolysis successfully unmasks the initially protected surface hydroxyl groups. The observed [P]:[Co] = 1.1 is very close to the value [P]:[Co] = 1.2 obtained for a surface-grafted D monolayer on NMC from a single-step solution grafting procedure.[34] We speculate that the slightly higher D surface ligand density arising from the one-step procedure stems from the cooperative nature of the alkylphosphonate surface grafting process.[37] These experiments nonetheless establish the viability of BB as a surface protecting group for kinetically controlled, template-diercted deposition of spatially heterogeneous mixed alkyl phosphonate monolayers on NMC.

Using BB as a removable surface protecting group for template-directed coating, we generated two NMC samples having mixed alkyl phosphonate coatings of decylphosphonic acid

and octadecylphosphonic acid: (1) D-OD and (2) OD-D. In the D-OD samples, the final OD label corresponds to the ligand that coats the surface sites that originally reacted with the BB; analogously, D coats the nucleophilic surface sites that reacted with the BB in the OD-D samples. XPS analyses of the D-OD and OD-D coated NMC obtained from the three-step coating process reveal that the atom percent ratios are [P]:[Co] =1.5 and 1.7, respectively. The consistency of these values with the [P]:[Co] = 1.5 for pure, high crystallinity OD monolayers on the same NMC powder[34] implies that the mixed coatings completely cover the particle surfaces. Note that the higher overall ligand density for the mixed monolayers and the OD monolayer as compared to the D and D-D monolayers probably reflects the cooperative nature of the ligand surface grafting process, whereby longer alkyl phosphonates pack more tightly with higher surface coverages.[37] That the OD-D surface coating density is slightly higher than that of the D-OD probably stems from the fact that the less sterically encumbered D molecules can penetrate to the surface to fill in any gaps in the partially OD-coated surface; however, the OD molecules are likely less able to fill such defects in the partially D-coated surface in the D-OD monolayers.

X-ray photoelectron spectra associated with the NMC transition metal sites at various stages in the three-step production of a D-OD mixed monolayer coating revealed the site selectivity of the reaction with BB (Figure 4.2). XPS reveals that the Ni (2p) binding energy is shifted 1 eV higher in the BB-D coated NMC as compared to the uncoated material, whereas the Co (2p) and Mn (2p) peaks remain at the same positions. Given the electron withdrawing nature of a benzyl group, the observation that only the Ni (2p) peak appreciably shifts to higher binding energy strongly suggests that the BB selectively reacts primarily with surface Ni sites. Assuming that the bulk NMC composition is reflected in the distribution of surface metal sites (*i.e.*, no

surface-induced segregation effects), one would expect ~50% of the surface metal sites to be Ni centers. If these Ni sites selectively react with the BB, then one would predict ~50% surface coverage by the BB–a prediction that matches well with the observed ~60% surface coverage by this removable surface protecting group (*vide supra*). After thermolytic surface deprotection of the BB ligand and subsequent OD coating to produce the desired D-OD coating, we note that the Ni (2p) peak returns to its original position that coincides with the Ni peak position for NMC bearing a pure D monolayer (see Figure S1). This sequence of observations suggests that the second alkyl phosphonic acid (OD) is selectively directed to the Ni sites because the nucleophilic surface sites on the NMC are primarily Ni-based.

We further quantified the transition metal content sampled by XPS analyses before and after the coating process. The native NMC exhibits an atom percent ratio [Ni]:[Mn]:[Co] = 5.1:3.0:2.0. After coating with D-OD, we observed [Ni]:[Mn]:[Co] = 5.0:3.0:1.9 by XPS, which demonstrates that the application and removal of the BB coating minimally alters the apparent NMC surface composition.

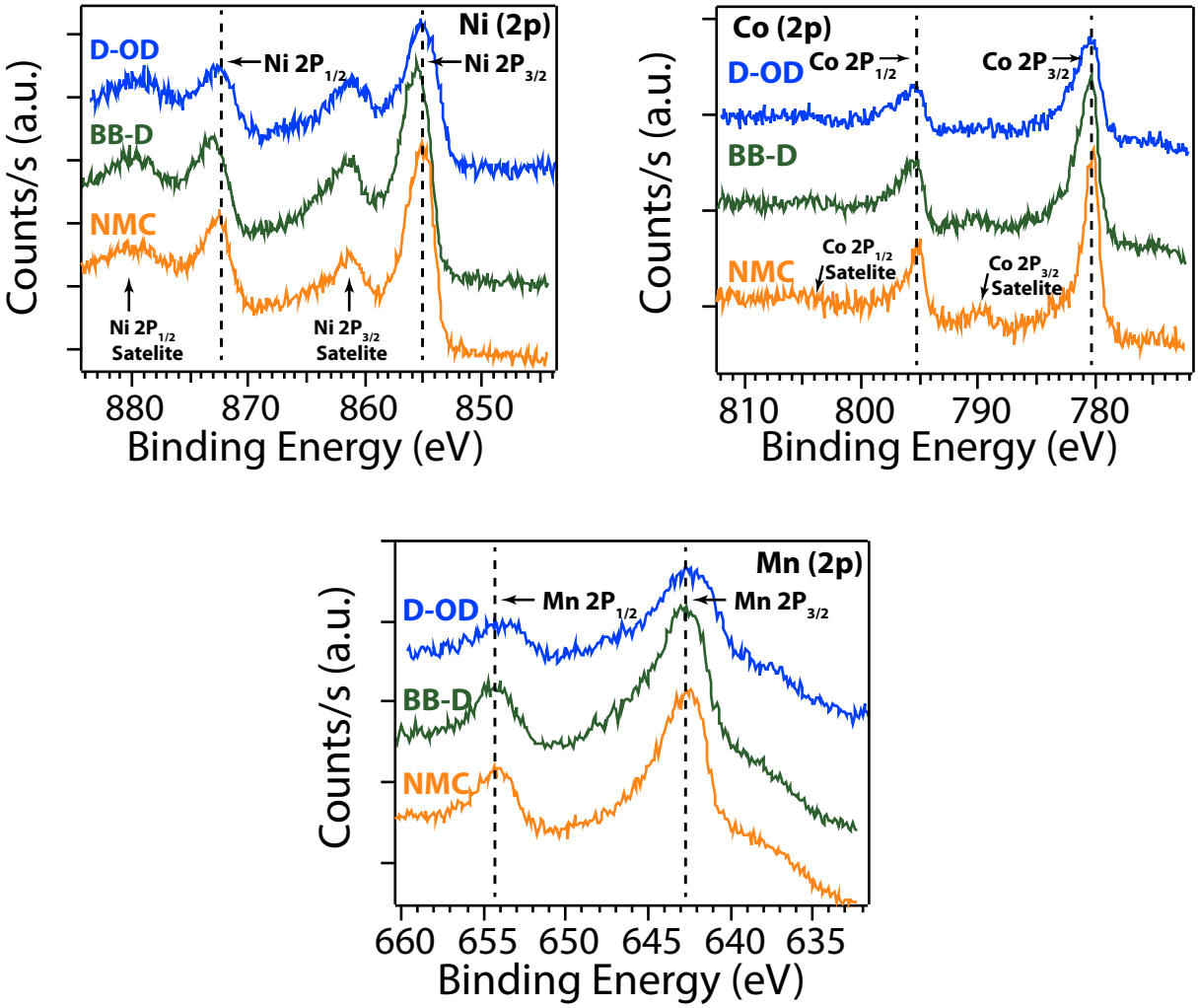

Figure 4.2. X-ray photoelectron spectra for the $2p_{1/2}$ and $2p_{3/2}$ Ni, Mn, and Co peaks in uncoated NMC, NMC after sequential treatment with benzyl bromide (BB) and decyl phosphonic acid (D) to yield a BB-D coating, and the mixed D-OD coating derived from BB thermolysis from the surface and subsequent treatment with octadecylphosphonic acid (OD). The observed binding energy shoft for the Ni (2p) peak in the BB-D coating indicates that the BB reacts primarily with the Ni sites on the NMC surface.

The NMC cathode powders coated with D-OD and OD-D mixed alkylphosphonate monolayers were incorporated into composite cathodes comprising carbon black (4.5 wt%) as a conductive additive and PVDF (3.5 wt%) as a high dielectric binder, for charge-discharge cycle

performance testing in half-cells against Li metal electrodes in CR2032 coin cell format. The results of these tests shown in Figure 4.3 indicate that the D-OD coated NMC exhibits somewhat reduced capacity fade as compared to the OD-D coating. While the difference in discharge capacity is within the statistical error derived from averaging the results of measurements from three separate coin cells of each type, the apparent slope of the capacity fade curve is slightly steeper for the OD-D coating (–0.7 mA•h/g or -0.4% capacity loss per cycle) as compared to the D-OD sample (–0.5 mA•h/g or -0.28% capacity loss per cycle). This finding suggests that the D-OD coating is somewhat more effective at mitigating parasitic processes, such as electrolyte decomposition, which decrease the half-cell discharge capacity upon repeated cycling. Our previous study of single component (pure) alkylphosphonate monolayers on NMC indicated that the pure OD monolayer was more effective than the D monolayer at preventing electrolyte breakdown during cell cycling.[34] Given the modest performance improvement in the D-OD cells in which the reactive Ni sites are coated with the more protective OD ligand, we conclude that the placing the thicker OD coating on the Ni sites impedes their ability induce electrolyte breakdown. Conversely, placing the thin D coating on the Ni sites as in the OD-D coating results in worse cycling performance. Thus, nucleophilic Ni sites appear important in parasitic electrolyte breakdown processes, which suggests that blocking electrolyte contact with them is important for improving cell cycling performance.

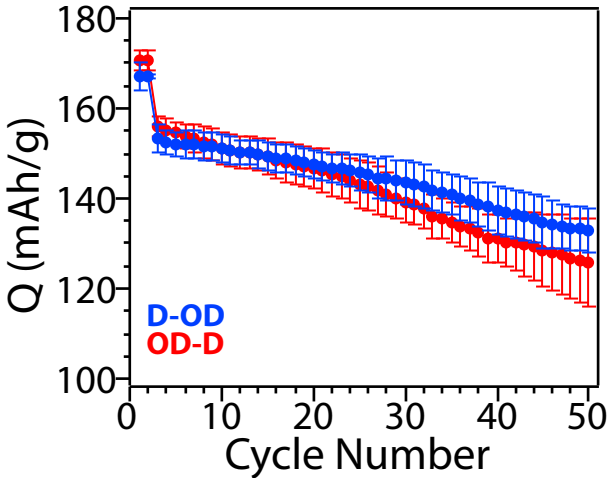

Figure 4.3. Lithium half–cell cycling performance test results (triplicate average) for NMC cathodes coated with D-OD and OD-D mixed alkyl phosphonates demonstrate that the D-OD coating (0.5 mA•h/g decrease per cycle) is more effective in reducing capacity loss compared to the OD-D coating (0.7 mA•h/g decrease per cycle). See text for detailed testing conditions.

Fast discharge rate performance tests on lithium half-cells based on mixed monolayer-coated NMC cathodes revealed striking differences in the activities of the D-OD and OD-D coated cathode powders (Figure 4.4). At discharge rates > 2 C, the D-OD coated cathodes exhibited significantly greater discharge capacity retention by 30% at 5 C, and ≥ 300 % at 8 and 10 C. This surprising behavior could arise from two possible mechanisms. One possibility is that electrolyte breakdown on the OD-D coating generates a high impedance layer with low Li-ion permeability that prevents Li^+ intercalation into the cathode during cell discharge, and these processes are not operative with a D-OD coating. Alternatively, coating surface domains rich in Co and Mn sites with the less Li-ion permeable OD as in the OD-D coating decreases the rate of Li-ion intercalation at the cathode surface, whereas coating the Ni-rich surface domains with the less permeable OD as in the D-OD has little impact on intercalation. We sequentially investigate each of these two potential scenarios in detail.

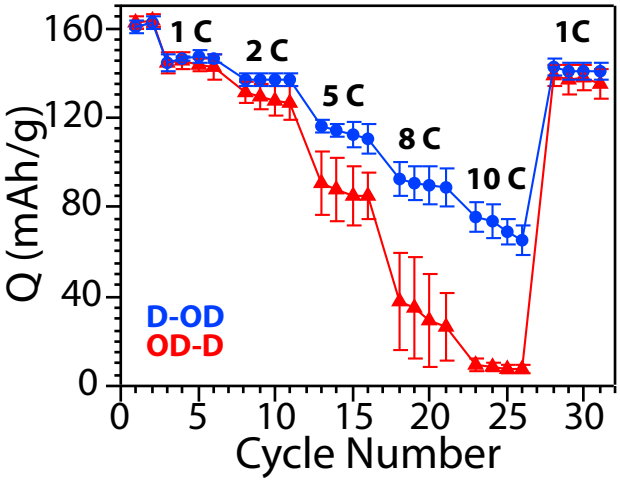

Figure 4.4 Lithium half–cell rate performance test results (triplicate average) for NMC cathodes coated with D-OD and OD-D mixed alkyl phosphonate coatings demonstrate that the D-OD coating significantly minimizes capacity loss compared to the OD-D coating at rates > 2 C. See text for details of test protocols.

Figure 4.5 depicts representative results of electrochemical impedance spectroscopy (EIS) measurements on Li half-cells before and after the rate performance testing. Nyquist plots were fit using an equivalent circuit model $R_{soln} + C_{interface}/R_{interface} + C_{CT}/R_{CT}$, where R_{soln} is the electrolyte solution resistance, $C_{interface}$ and $R_{interface}$ are the respective interfacial capacitance and resistance, and C_{CT} and R_{CT} are the charge transfer capacitance and resistance associated with Li^+ intercalation into the NMC particles. Table 1 enumerates the shift in the high frequency intercept associated with the change in the solution resistance before and after rate testing (ΔR_{soln}), and the diameter of the first semicircle after rate testing that corresponds to any newly developed interfacial resistances ($R_{interface}$). We interpret ΔR_{soln} as an indicator of the extent electrolyte degradation during the rate test, whereas $R_{interface}$ after cycling provides information about the combined resistance of the monolayer coating and any decomposed electrolyte present on the surface.[34] The surprising similarities in the values of ΔR_{soln} and $R_{interface}$ suggest that the mixed

monolayers allow comparable amounts of electrolyte breakdown and that the resulting total interfacial resistance is nearly the same. These results strongly imply that the difference in rate performance does not stem from differences in the protective nature of the coatings per the first mechanism mentioned above.

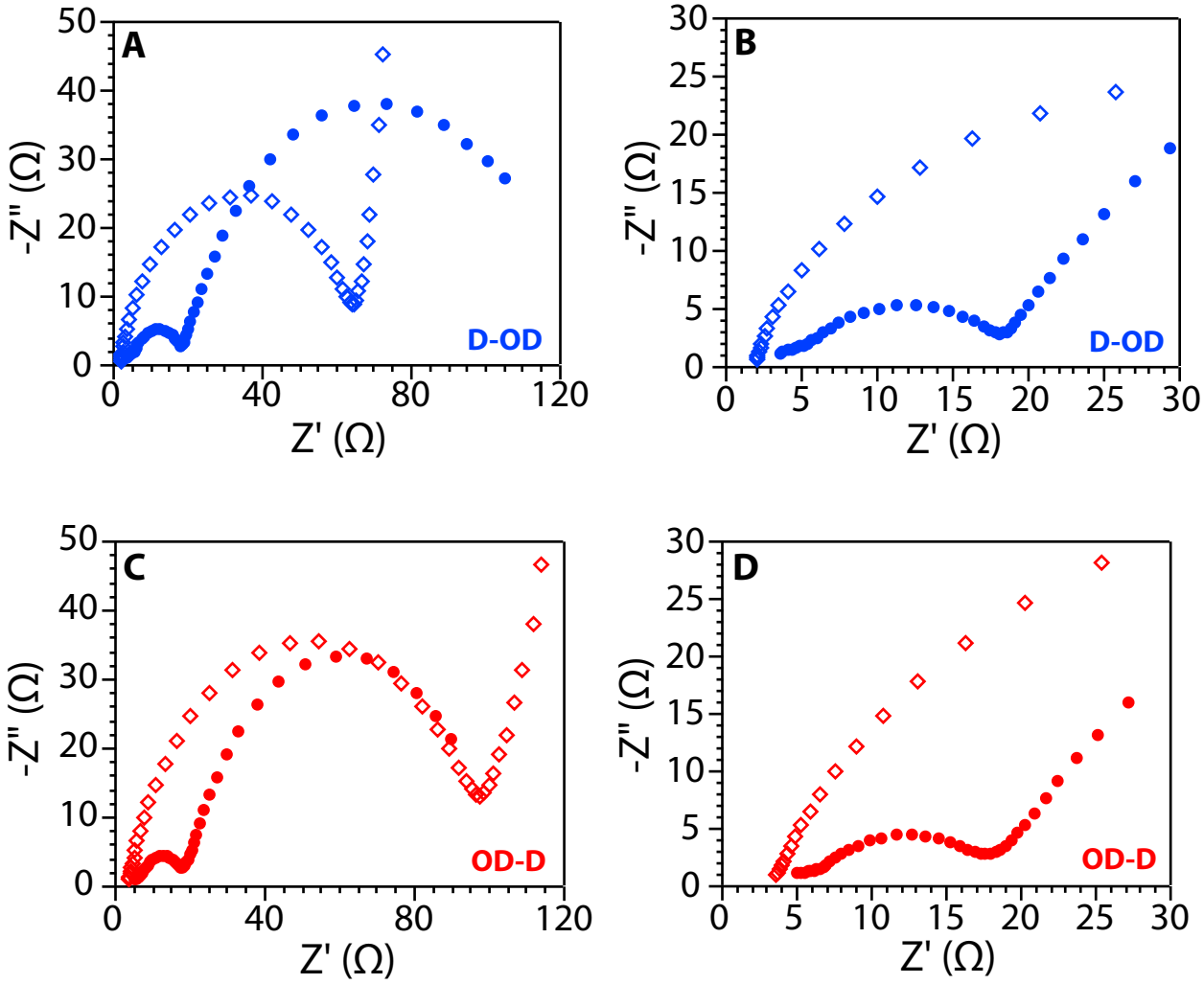

Figure 4.5. (A) Representative full range and (B) magnified Nyquist plots for Li half-cells with D-OD–coated NMC cathodes for "as made" cells (open symbols) and after C-rate testing (filled symbols). (C) Representative full range and (D) magnified Nyquist plots for Li half-cells with OD-D–coated NMC cathodes for "as made" cells (open symbols) and after C-rate testing (filled symbols). The similar values of ΔR_{soln} and $R_{interface}$ for the D-OD and OD-D coated NMC imply that difference in rate performance does not arise from differences in electrolyte decomposition

or different surface layer impedances.

Table 1. Changes in the Solution and Interfacial Resistances After Discharge Rate Performance Testing.

Coating Type	ΔR_{soln} (Ω)	$R_{interface}$ (Ω)
D-OD	1.56 (± 0.47)	15.4 (± 1.5)
OD-D	1.50 (± 0.43)	15.0 (± 0.59)

Absent differences in the protective nature of the OD-D and D-OD NMC coatings, the cathode discharge rate performance must directly depend on the rate of transfer of the Li^+ through the coating and its subsequent intercalation into the underlying active material. Thicker coatings with high surface coverages (high [P]:[Co] atom ratios) typically exhibit high crystallinities that impede Li^+ ion permeation to the active materials surface, whereas less crystalline coatings allow Li^+ ions to approach the underlying interface.[34] In spite of their similar surface ligand coverages, the observation that the D-OD coated NMC generally exhibits better rate performance than the OD-D coated cathodes (Figure 4) provocatively suggests that these coatings direct Li-ion intercalation differently to the active NMC surface. To gain more insight into these phenomena, we compared the rate performances of cathodes comprising NMC coated with pure D, D-OD, and OD-D in Figure 4.6.

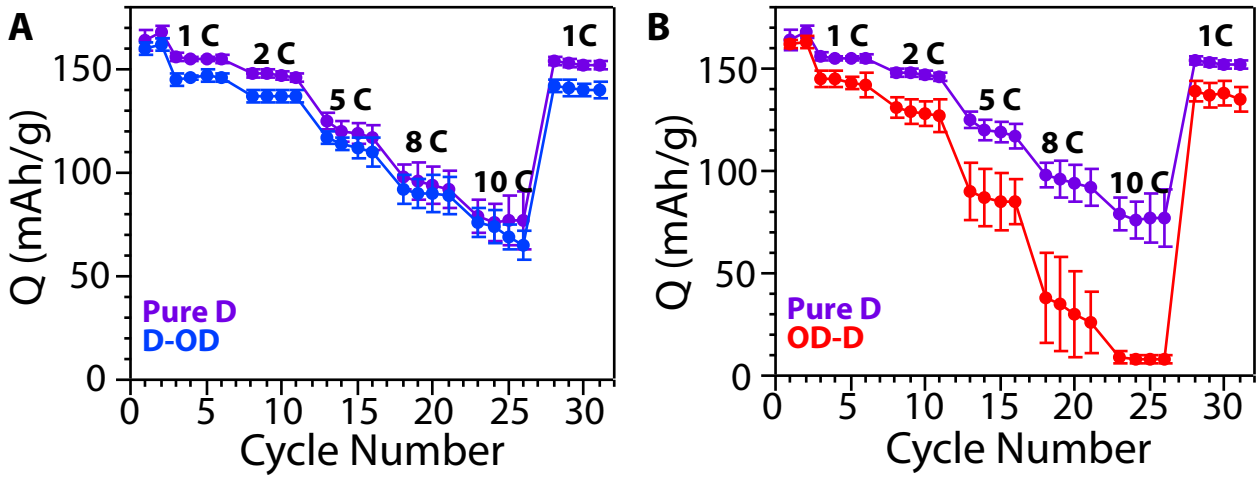

Figure 4.6. Comparative rate performance of NMC coated with a pure decylphosphonate (D) monolayer with (A) D-OD coated NMC and (B) OD-D coated NMC, showing that the D-OD mixed monolayer behaviors similarly to the pure D monolayer in spite of the higher surface ligand coverage by the D-OD monolayer. Similiarities in D and D-OD coated NMC performance suggest that coating the Ni sites with OD minimally impacts the coated NMC performance, whereas OD coating of the Mn and Co sites deleteriously affects the high discharge rate performance of NMC cathodes.

From Figure 4.6a, it is apparent that the rate performance of the D-OD coated NMC is nearly the same as that of the pure D-coated material. This observation is particularly striking given that the surface coverage of the D-OD layer ([P]:[Co] = 1.5) is 25% higher than that of the pure D coating ([P]:[Co] = 1.2), which implies tighter packing of the alkyl chains and thus higher crystallinity in the mixed D-OD monolayer. This increased crystallinity of the D-OD monolayer should severely hinder Li^+ intercalation, an expectation contrary to our experimental observation. Furthermore, the surface ligand coverage in the D-OD and pure OD coatings are the same ([P]:[Co] = 1.2), yet the D-OD coating exhibits better rate performance (see Figure S2a). Thus, coating the Ni-rich surface domains with the less Li-ion permeable OD minimally impacts the coated cathode discharge rate performance. Conversely, the OD-D coated NMC performs poorly

as compared to the pure D-coating (Figure 4.6b) as well as the pure OD-coating (Figure S2b), suggesting that coating the Co- and Mn-rich surface domains with the higher crystallinity and less permeable OD coating significantly impedes Li-ion intercalation to degrade rate performance. From these comparisons, we deduce that the kinetic barrier for Li-ion intercalation at the NMC cathode surface is lower at the Co- and Mn-rich surface domains than at the Ni-rich areas of the surface. In other words, these mixed monolayer coating experiments strongly imply that Co- and Mn-rich surface sites are the primary sites for Li-ion (de)intercalation.

The slightly better rate performance observed for the pure D versus the D-OD coated NMC at discharge rates of 1 C and 2 C (Figure 4.6a) may stem from the imperfect selectivity of the initial BB coating step. We previously deduced that 60% of the surface sites reacted with BB. Assuming that the surface metal site identity distribution is the same as in the bulk NMC (50 mol% Ni, 30 mol% Mn, 20 mol% Co), the BB surface coverage implies that ~10% of the combined Mn and Co sites react. Tracing this surface site population through the three-step coating procedure to produce D-OD coated NMC suggests that ~10 mol% of the surface Mn/Co sites are coated with the OD. The reduced ability of these 10 mol% Mn/Co sites to facilitate Li-ion intercalation could then result in the observed ~10% lower discharge capacity in rate performance tests conducted at 1 C and 2 C, relative to the pure D coating in which all of the Mn, Co, and Ni sites are equally accessible. To support this notion, we normalized the discharge capacity curves in Figure 4.6 using the 1 C as a reference point (Figure 4.7). The near perfect overlap of the normalized rate performance discharge data for the pure D and D-OD coated NMCs lends credence to our deduction. Figure 4.7b further demonstrates that differences in initial capacity at 1 C do not explain the overall C-rate performance difference between the OD-

D, D-OD, and pure D coating. (Similarly normalized discharge curves comparing D-OD, OD-D, and pure OD coatings are given in Figure S3.)

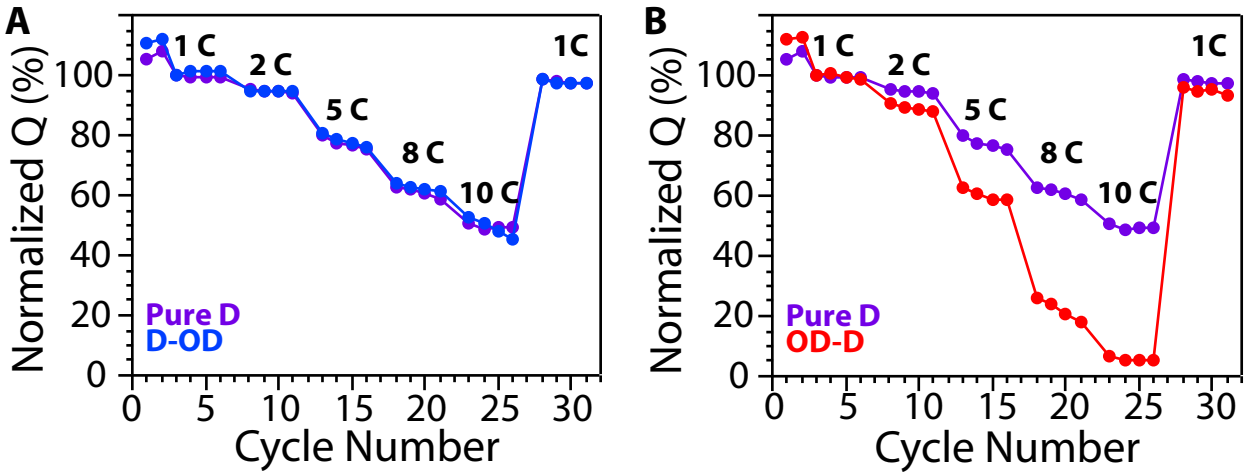

Figure 4.7. Comparison of the normalized discharge rate performance of NMC coated with a pure decylphosphonate (D) coating (A) D-OD and (B) OD-D coating, in which the 1 C discharge capacity was used as the reference. The D and D-OD exhibit nearly identical behavior regardless of discharge rate, while the OD-D coating exhibits poor performance, implying that Li^+ access to the Mn and Co sites is crucial for optimal discharge performance at high C rates.

4.4 Conclusion

We developed a three-step procedure for templating the spatially heterogeneous coating of binary alkylphosphonate monolayers of decylphosphonate (D) and octadecylphosphonate (OD) onto the surfaces of high voltage NMC cathode powders. In the first step, nucleophilic surface sites on the NMC are reacted with electrophilic benzyl bromide (BB) to yield a partially coated surface. XPS analyses reveal that the BB electrophile primarily attaches to surface Ni sites, evidenced by a 1 eV shift in only the binding energy of the Ni (2p) peak. The open Mn/Co

surface domains are then coated with the first alkyphosphonate, prior to high temperature thermoylsis of the benzylated surface to reveal the Ni sites. Finally, the Ni sites are coated with a second alkylphosphonate. This coating strategy allows for selective coating of the Ni-rich surface domains with OD and Co/Mn-rich domains with D to yield a D-OD coating; alternatively, one can coat the Ni-rich sites with D and the Co/Mn-rich sites to yield a OD-D coating. This simple, kinetically controlled, template-directed coating strategy is likely generally applicable to numerous metal oxide materials that exhibit heterogeneities in their surface sites reactivities.

Differences in the charge discharge performance of half cells constructed with cathodes comprising the D-OD and OD-D coated NMC indicate that passivation of the Ni sites with the thicker OD coating slightly improves capacity retention after 50 cycles. The starkly better discharge rate performance of the D-OD coating as compared to the OD-D suggests that the barrier for Li-ion intercalation into $LiNi_{0.5}Mn_{0.3}Co_{0.2}O_2$ (NMC) is lowest through the surface domains rich in Mn/Co sites. Thus, this study provides new insights into the reactivity and (de)intercalation behaviors of the various metal sites on NMC surfaces that may beget new approaches to improving high voltage cathode cycling stability and rate performance for high power applications.

4.5 References

1. Scrosati, B.; Garche, J., Lithium batteries: Status, prospects and future. *J. Power Sources* **2010,** *195* (9), 2419-2430.

2. Manthiram, A., Materials Challenges and Opportunities of Lithium Ion Batteries. *J. Phys. Chem. Lett.* **2011,** *2* (3), 176-184.

3. Amine, K.; Kanno, R.; Tzeng, Y., Rechargeable lithium batteries and beyond: Progress, challenges, and future directions. *MRS Bull.* **2014,** *39* (05), 395-401.

4. Goodenough, J. B.; Kim, Y., Challenges for Rechargeable Li Batteries†. *Chem. Mater.* **2010,** *22* (3), 587-603.

5. John, B. G., Evolution of Strategies for Modern Rechargeable Batteries. *Acc. Chem. Res.* **2013,** *46*, 1053.

6. Kraytsberg, A.; Ein-Eli, Y., Higher, Stronger, Better…□ A Review of 5 Volt Cathode Materials for Advanced Lithium-Ion Batteries. *Adv. Energy Mater.* **2012,** *2* (8), 922-939.

7. Hausbrand, R.; Cherkashinin, G.; Ehrenberg, H.; Gröting, M.; Albe, K.; Hess, C.; Jaegermann, W., Fundamental degradation mechanisms of layered oxide Li-ion battery cathode materials: Methodology, insights and novel approaches. *Mater. Sci. Eng. B* **2015,** *192*, 3-25.

8. Fu, L. J.; Liu, H.; Li, C.; Wu, Y. P.; Rahm, E.; Holze, R.; Wu, H. Q., Surface modifications of electrode materials for lithium ion batteries. *Solid State Sci.* **2006,** *8* (2), 113-128.

9. Yoshida, T.; Takahashi, M.; Morikawa, S.; Ihara, C.; Katsukawa, H.; Shiratsuchi, T.; Yamaki, J.-i., Degradation Mechanism and Life Prediction of Lithium-Ion Batteries. *J. Electrochem. Soc.* **2006,** *153* (3), A576.

10. Xu, K.; von Cresce, A., Interfacing electrolytes with electrodes in Li ion batteries. *J. Mater. Chem.* **2011,** *21* (27), 9849.

11. Aravindan, V.; Gnanaraj, J.; Madhavi, S.; Liu, H. K., Lithium-ion conducting electrolyte salts for lithium batteries. *Chem. Eur. J.* **2011,** *17* (51), 14326-46.

12. Boerner, M.; Horsthemke, F.; Kollmer, F.; Haseloff, S.; Friesen, A.; Winter, M.; Schappacher, F. M., Degradation effects on the surface of commercial $LiNi_{0.5}Co_{0.2}Mn_{0.3}O_2$ electrodes. *J. Power Sources* **2016,** *335*, 45-55.

13. Zhang, S. S., A review on electrolyte additives for lithium-ion batteries. *J. Power Sources* **2006,** *162* (2), 1379-1394.

14. Abe, K.; Ushigoe, Y.; Yoshitake, H.; Yoshio, M., Functional electrolytes: Novel type additives for cathode materials, providing high cycleability performance. *J. Power Sources* **2006,** *153* (2), 328-335.

15. Haregewoin, A. M.; Wotango, A. S.; Hwang, B.-J., Electrolyte additives for lithium ion battery electrodes: progress and perspectives. *Energy Environ. Sci.* **2016,** *9* (6), 1955-1988.

16. Wu, Z.; Ji, S.; Zheng, J.; Hu, Z.; Xiao, S.; Wei, Y.; Zhuo, Z.; Lin, Y.; Yang, W.; Xu, K.; Amine, K.; Pan, F., Prelithiation Activates $Li(Ni_{0.5}Mn_{0.3}Co_{0.2})O_2$ for High Capacity and Excellent Cycling Stability. *Nano Lett.* **2015,** *15* (8), 5590-6.

17. Wu, Z.; Ji, S.; Hu, Z.; Zheng, J.; Xiao, S.; Lin, Y.; Xu, K.; Amine, K.; Pan, F., Pre-Lithiation of $Li(Ni_{1-x-y}Mn_xCo_y)O_2$ Materials Enabling Enhancement of Performance for Li-Ion Battery. *ACS. Appl. Mater. Interfaces* **2016,** *8* (24), 15361-8.

18. Yang, L.; Ravdel, B.; Lucht, B. L., Electrolyte Reactions with the Surface of High Voltage LiNi0.5Mn1.5O4 Cathodes for Lithium-Ion Batteries. *Electrochem. Solid State Lett.* **2010,** *13* (8), A95-A97.

19. Matsuta, S.; Kato, Y.; Ota, T.; Kurokawa, H.; Yoshimura, S.; Fujitani, S., Electron-spin-resonance study of the reaction of electrolytic solutions on the positive electrode for lithium-ion secondary batteries. *J. Electrochem. Soc.* **2001,** *148* (1), A7-A10.

20. Aurbach, D.; Gamolsky, K.; Markovsky, B.; Salitra, G.; Gofer, Y.; Heider, U.; Oesten, R.; Schmidt, M., The Study of Surface Phenomena Related to Electrochemical Lithium Intercalation into Li[sub x]MO[sub y] Host Materials (M = Ni, Mn). *J. Electrochem. Soc.* **2000,** *147* (4), 1322.

21. Su, Y.; Cui, S.; Zhuo, Z.; Yang, W.; Wang, X.; Pan, F., Enhancing the High-Voltage Cycling Performance of $LiNi_{0.5}Mn_{0.3}Co_{0.2}O_2$ by Retarding Its Interfacial Reaction with an Electrolyte by Atomic-Layer-Deposited Al_2O_3. *ACS. Appl. Mater. Interfaces* **2015,** *7* (45), 25105-12.

22. Li, X.; Liu, J.; Meng, X.; Tang, Y.; Banis, M. N.; Yang, J.; Hu, Y.; Li, R.; Cai, M.; Sun, X., Significant impact on cathode performance of lithium-ion batteries by precisely controlled metal oxide nanocoatings via atomic layer deposition. *J. Power Sources* **2014,** *247*, 57-69.

23. Sun, Y. K.; Lee, M. J.; Yoon, C. S.; Hassoun, J.; Amine, K.; Scrosati, B., The role of AlF3 coatings in improving electrochemical cycling of Li-enriched nickel-manganese oxide electrodes for Li-ion batteries. *Adv. Mater.* **2012,** *24* (9), 1192-6.

24. Li, H.; Zhou, H., Enhancing the performances of Li-ion batteries by carbon-coating: present and future. *Chem. Commun.* **2012,** *48* (9), 1201-17.

25. Jackson, D. H. K.; Laskar, M. R.; Fang, S. Y.; Xu, S. Z.; Ellis, R. G.; Li, X. Q.; Dreibelbis, M.; Babcock, S. E.; Mahanthappa, M. K.; Morgan, D.; Hamers, R. J.; Kuech, T. F., Optimizing AlF_3 atomic layer deposition using trimethylaluminum and TaF_5: Application to high voltage Li-ion battery cathodes. *J. Vac. Sci. Technol. A* **2016,** *34* (3).

26. Quinlan, R. A.; Lu, Y.-C.; Kwabi, D.; Shao-Horn, Y.; Mansour, A. N., XPS Investigation of the Electrolyte Induced Stabilization of $LiCoO_2$ and "$AlPO_4$"-Coated $LiCoO_2$Composite Electrodes. *J. Electrochem. Soc.* **2015,** *163* (2), A300-A308.

27. Tebbe, J. L.; Fuerst, T. F.; Musgrave, C. B., Degradation of Ethylene Carbonate Electrolytes of Lithium Ion Batteries via Ring Opening Activated by $LiCoO_2$ Cathode Surfaces and Electrolyte Species. *ACS. Appl. Mater. Interfaces* **2016,** *8* (40), 26664-26674.

28. Liu, R. R.; Deng, X.; Liu, X. R.; Yan, H. J.; Cao, A. M.; Wang, D., Facet dependent SEI formation on the LiNi(0.5)Mn(1.5)O4 cathode identified by in situ single particle atomic force microscopy. *Chem. Commun.* **2014,** *50* (99), 15756-9.

29. Andreu, N.; Flahaut, D.; Dedryvere, R.; Minvielle, M.; Martinez, H.; Gonbeau, D., XPS investigation of surface reactivity of electrode materials: effect of the transition metal. *ACS. Appl. Mater. Interfaces* **2015,** *7* (12), 6629-36.

30. Kang, Y.; Li, M.; Cai, Y.; Cargnello, M.; Diaz, R. E.; Gordon, T. R.; Wieder, N. L.; Adzic, R. R.; Gorte, R. J.; Stach, E. A.; Murray, C. B., Heterogeneous catalysts need not be so "heterogeneous": monodisperse Pt nanocrystals by combining shape-controlled synthesis and purification by colloidal recrystallization. *J. Amer. Chem. Soc.* **2013,** *135* (7), 2741-7.

31. Zaera, F.; Gellman, A. J.; Somorjai, G. A., SURFACE SCIENCE STUDIES OF CATALYSIS - CLASSIFICATION OF REACTIONS. *Acc. Chem. Res.* **1986,** *19* (1), 24-31.

32. Sinfelt, J. H., HETEROGENEOUS CATALYSIS - SOME RECENT DEVELOPMENTS. *Science* **1977,** *195* (4279), 641-646.

33. Sinfelt, J. H., STRUCTURE OF METAL-CATALYSTS. *Reviews of Modern Physics* **1979,** *51* (3), 569-589.

34. Chang, W., Slaymaker, E. L., Hamers, J. R., Mahanthappa, K. M., Effects of Alkyl Phosphonate Surface Coatings on High–Voltage $LiNi_{0.5}Mn_{0.3}Co_{0.2}O_2$ Cathode Performance. *in preparation* **2016**.

35. Gao, W.; Dickinson, L.; Grozinger, C.; Morin, F. G.; Reven, L., Self-assembled monolayers of alkylphosphonic acids on metal oxides. *Langmuir* **1996,** *12* (26), 6429-6435.

36. Gachot, G.; Grugeon, S.; Armand, M.; Pilard, S.; Guenot, P.; Tarascon, J. M.; Laruelle, S., Deciphering the multi-step degradation mechanisms of carbonate-based electrolyte in Li batteries. *J. Power Sources* **2008,** *178* (1), 409-421.

37. Spori, D. M.; Venkataraman, N. V.; Tosatti, S. G.; Durmaz, F.; Spencer, N. D.; Zurcher, S., Influence of alkyl chain length on phosphate self-assembled monolayers. *Langmuir* **2007,** *23* (15), 8053-60.

APENDIX 1

SUPPORTING INFORMATION FOR CHAPTER 3: EFFECTS OF ALKYL PHOSPHONATE SURFACE COATINGS ON HIGH-VOLTAGE LiNi0.5Mn0.3Co0.2O2 CATHODE PERFORMANCE

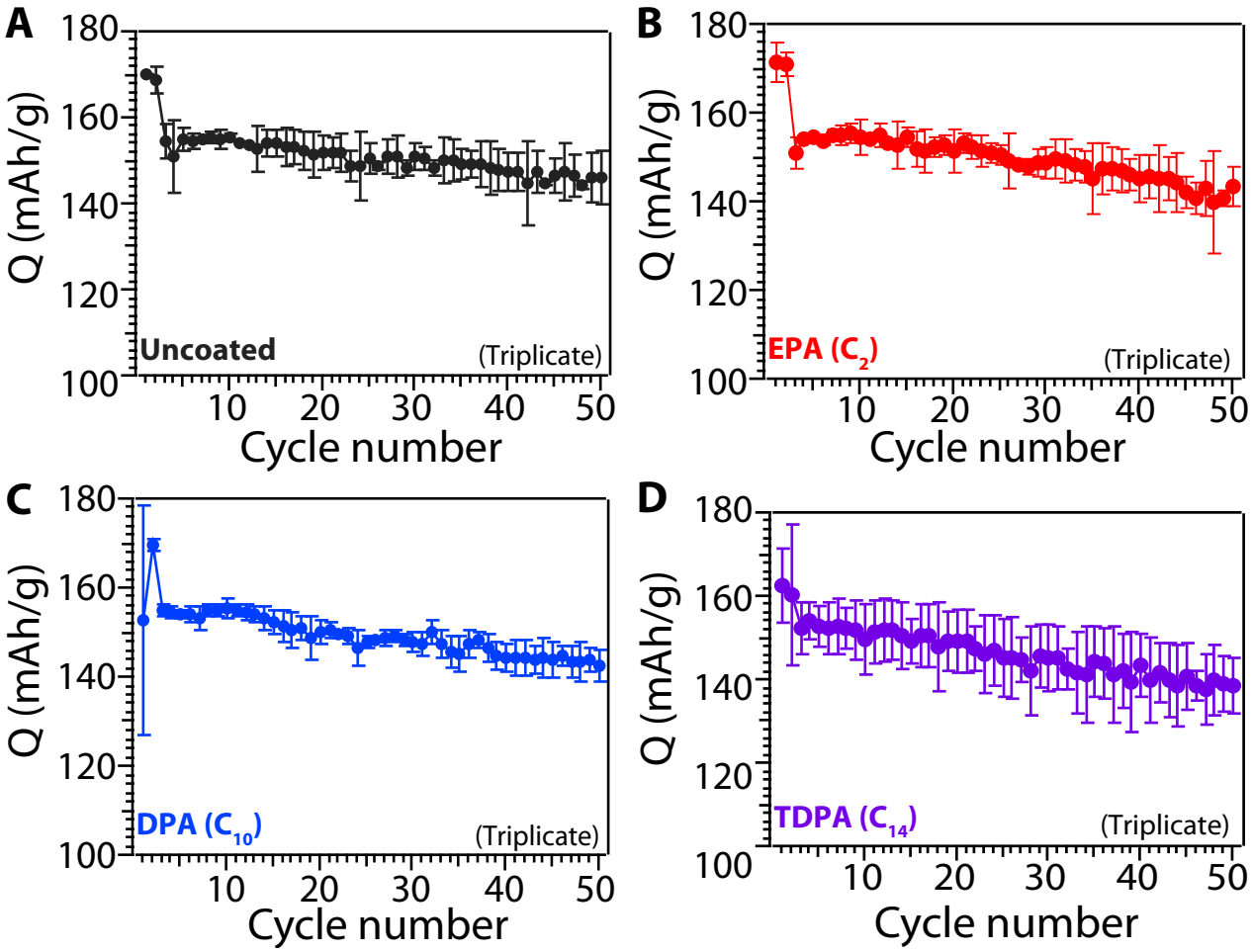

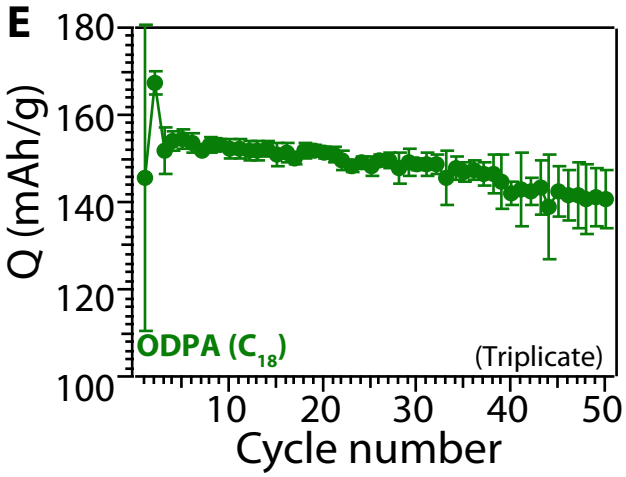

Figure A1.1. (A-E) Cycling performance of NMC cathode materials grafted with various alkylphosphonate monolayers with alkyl chains ranging in length from C_2–C_{18} with error bars, which reflect the average of data obtained from three half-cells that were cycled under similar testing conditions. Half–cells were initial conditioned by charging at 0.1 C and discharging at 0.1 C for the first two cycles, followed subsequent charging at 0.3 C and discharging at 1 C.

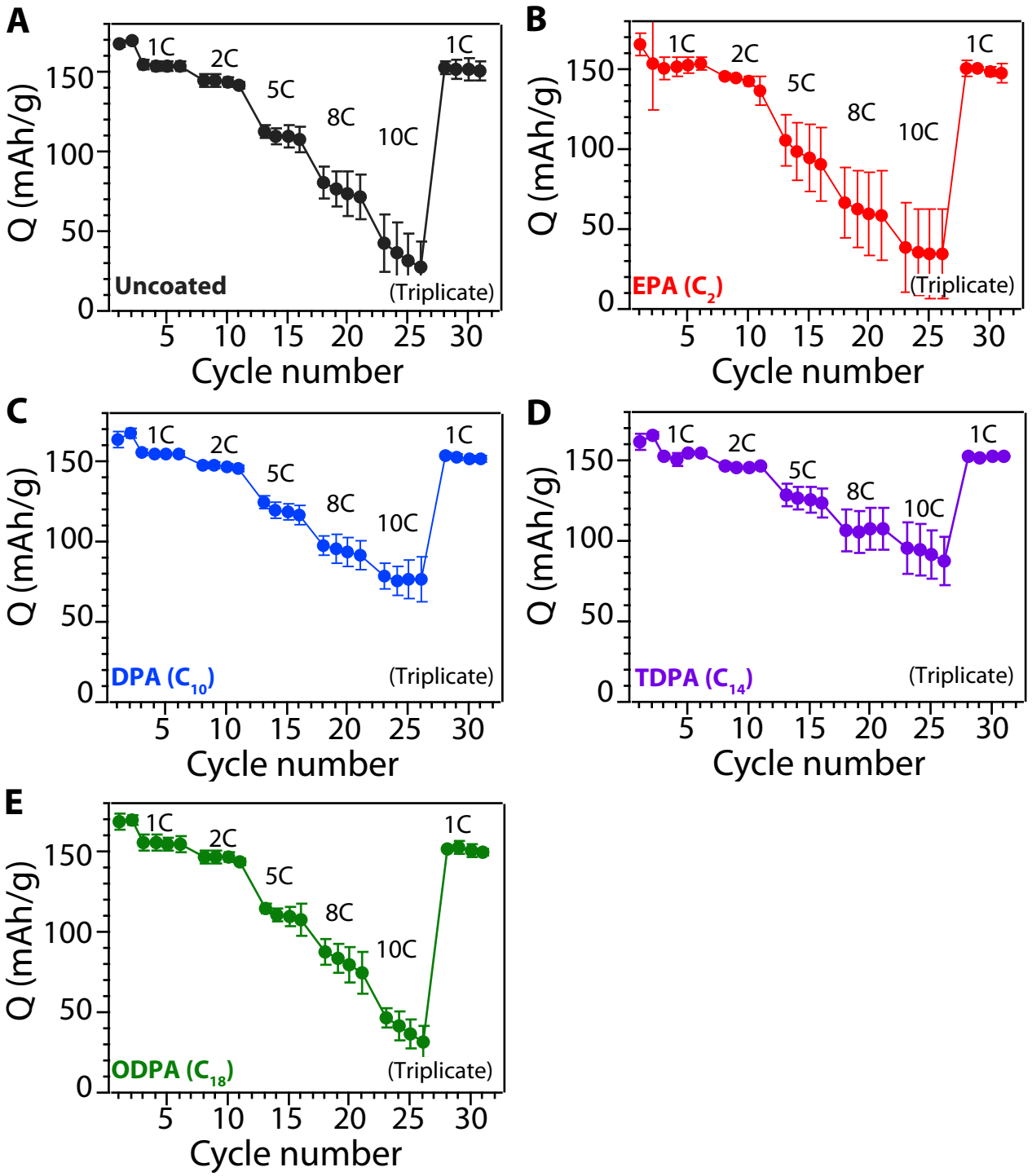

Figure A1.2. (A-E) Rate performance test data for NMC cathode materials coated with various alkylphosphonate monolayers with alkyl chains ranging in length from C_2–C_{18}, with error bars, which reflect the average of data obtained from three half-cells that were cycled under similar testing conditions. Half–cells were initial conditioned by charging at 0.1 C and discharging at 0.1 C for the first two cycles, followed subsequent charging at 0.3 C and discharging at 1, 2, 5, 8, 10,

and 1 C.

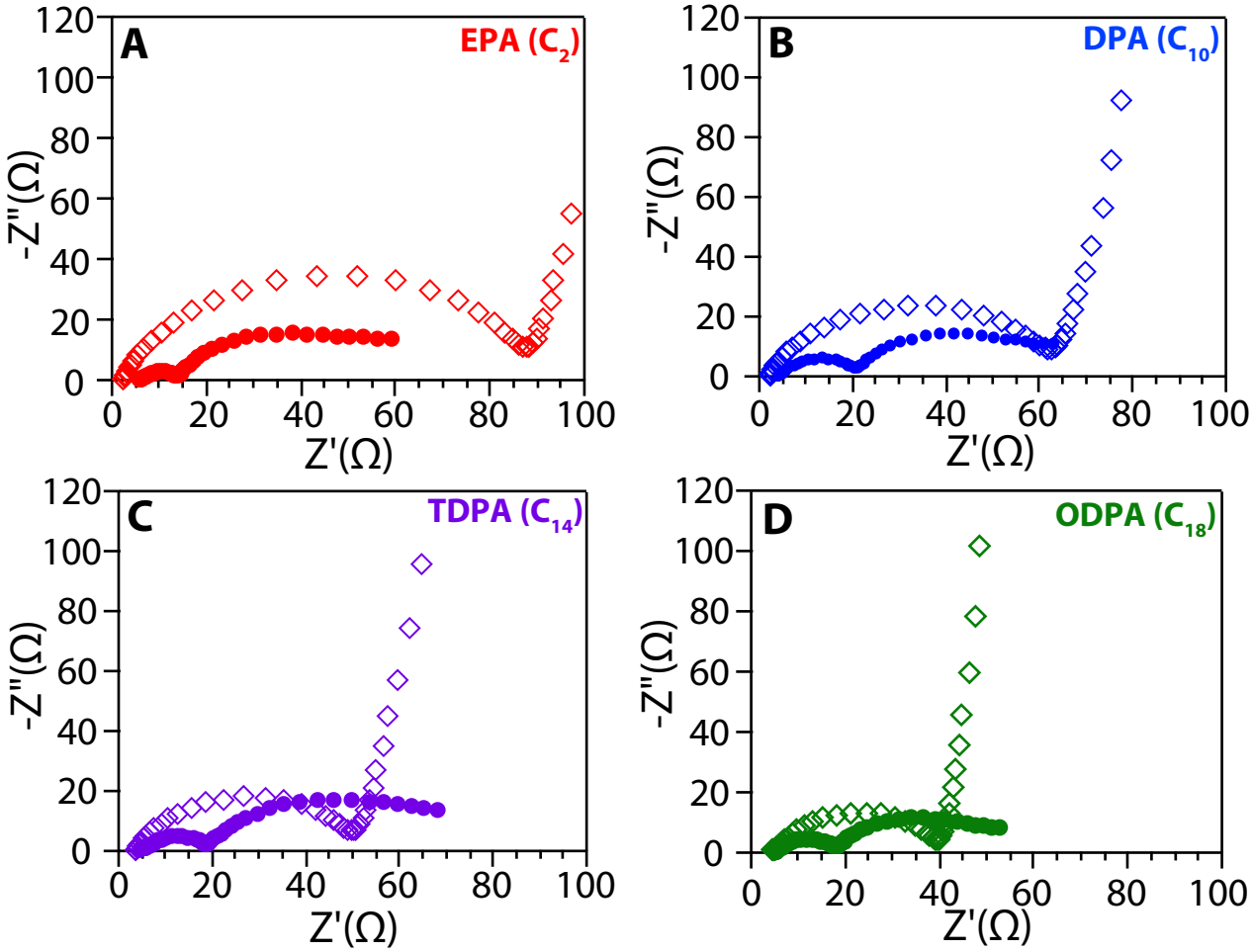

Figure A1.3. (A-D) Full Nyquist plots for half-cells based on alkyl phosphonate-grafted NMC cathode particles against Li metal before (◇) and after (●) the C-rate performance tests.

APENDIX 2

SUPPORTING INFORMATION FOR CHAPTER 4: LiNi0.5Mn0.3Co0.2O2 CATHODE SURFACE REACTIVITY : ROLE OF TRANSITION METALS AT THE ELECTRODE SURFACE

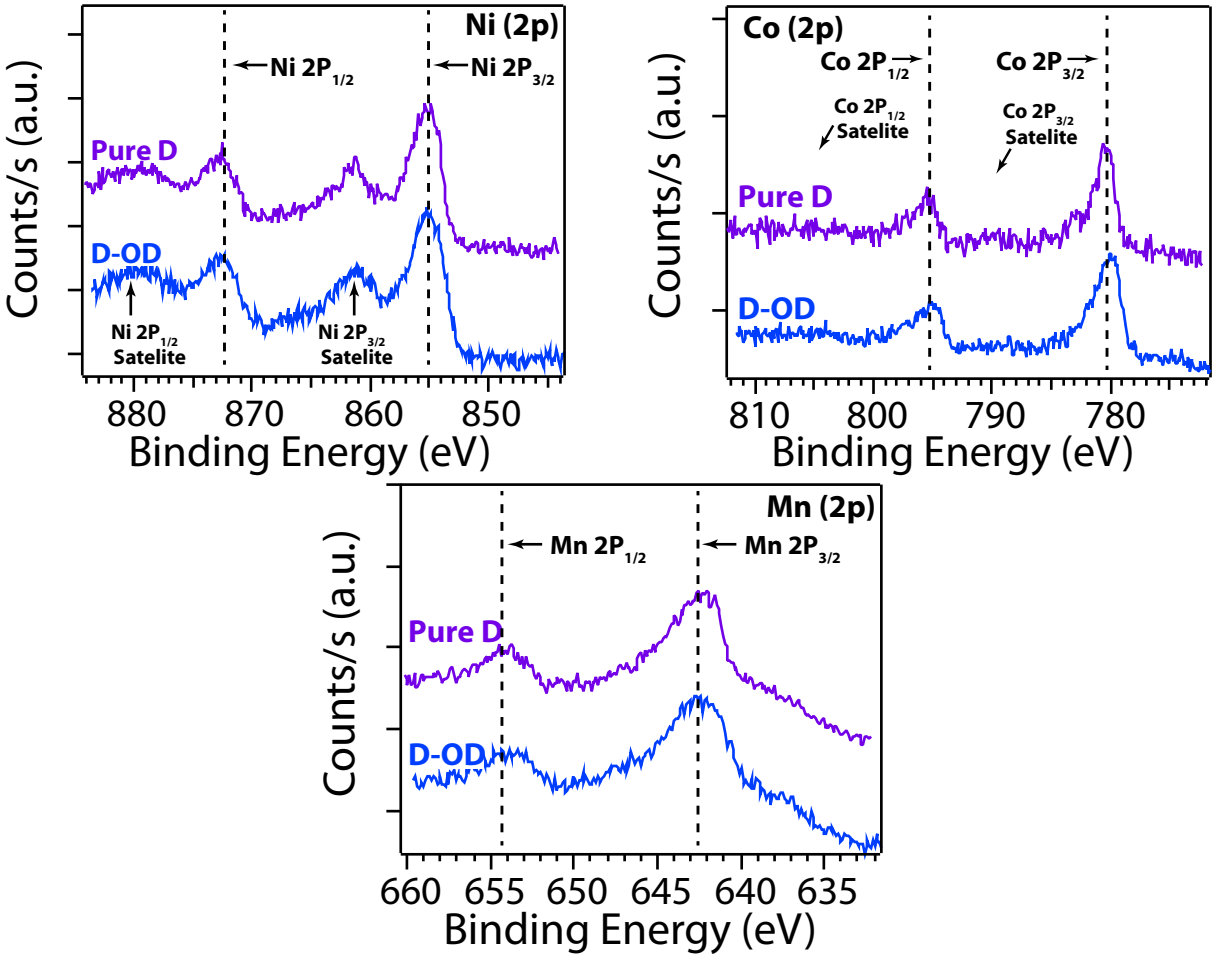

Figure A2.1. XPS of Ni, Mn and Co from decyl phosphonate (D) coated NMC and NMC coated with a decyl phosphonate/octadecyl phosphonate (D-OD) mixed coating. All spectra were referenced using a peak binding energy of C (1S) at 285 eV, and the lines in each spectrum indicate a peak binding energy of $2p_{1/2}$ and $2p_{3/2}$ from each element.

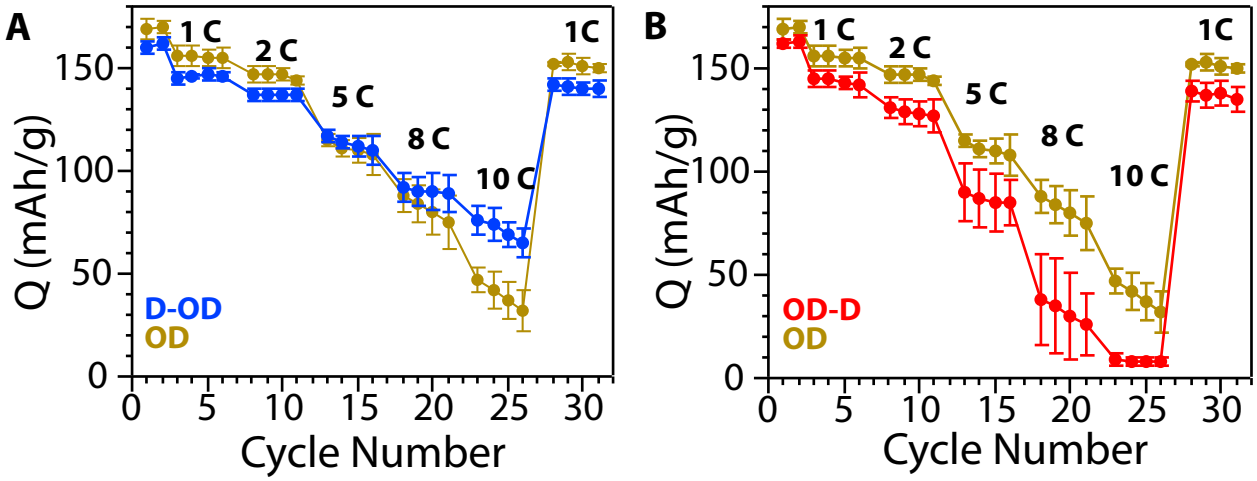

Figure A2.2. (A) Rate performance of NMC coated only with ocdecyl phosphonate and NMC coated with D-OD. (B) Rate performance of NMC coated only with ocdecyl phosphonate and NMC coated with OD-D.

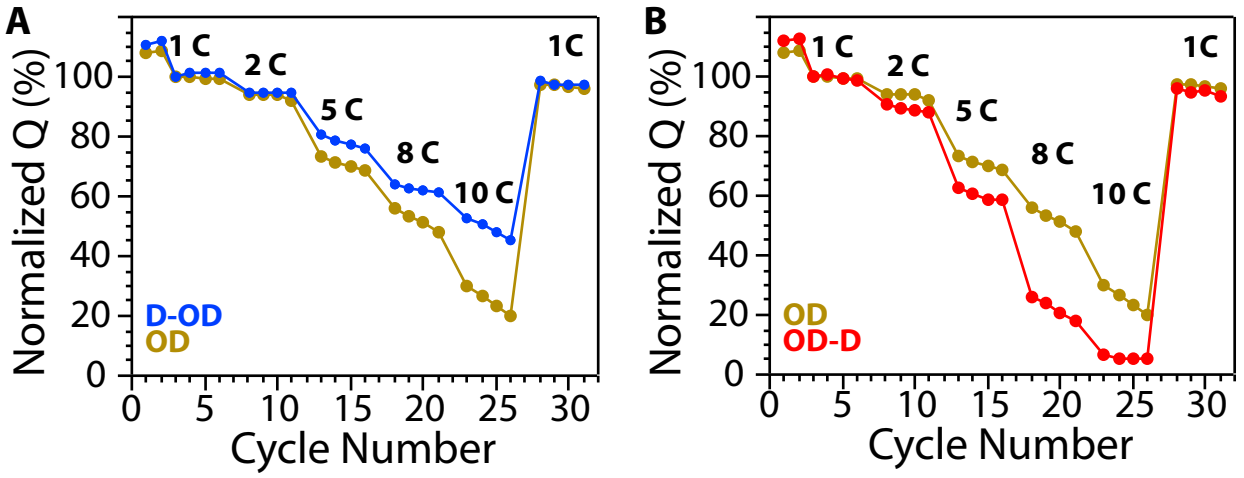

Figure A2.3. (A) Normalized rate performance of NMC coated only with octadecyl phosphonate and NMC coated with D-OD. (B) Normalized rate performance of NMC coated only with octadecyl phosphonate and NMC coated with OD-D.